A comparison of observed and modelled relative sea-level change over the satellite observational period 1993–2013

I. KOMIS,* A.B.A. SLANGEN, R.S.W. VAN DE WAL

Institute of Marine and Atmospheric research Utrecht, Utrecht University,
Princetonplein 5, 3584 CC Utrecht, The Netherlands

Final Submission: December 13th, 2016

Abstract

During the past two decades (1993–present) relative sea-level changes (RSL) have been monitored by satellite altimetry techniques. The European Space Agency Climate Change Initiative (ESA CCI) project on "Sea Level" has produced an improved set of sea-level products by applying a number of corrections—reduction of orbit errors, wet/dry atmospheric correction errors, reduction of instrumental drifts and bias, intercalibration biases, intercalibration between missions, combination of missions, and an improved reference mean sea-surface—into multi-mission (ERS-1&2, Envisat, TOPEX/Poseidon, Jason-1&2, and Geosat Follow-on) altimetry data over the period 1993–2013. We compared those data to RSL changes calculated by separation of mass (land-ice, terrestrial water storage) and volume (steric) changes of water, including the fingerprint due to mass changes. Based on CMIP5 (Coupled Model Intercomparison Project Phase 5) data and independent data sets for groundwater, reservoir storage, and glacial isostatic adjustment (GIA), local RSL changes can be calculated by summation of all the individual contributions at every grid point—taking into account gravitational and rotational aspects as well—over the satellite altimetry period at $1^o \times 1^o$ resolution with a land-ocean mask extending from $\pm 68.5^o$ in latitude. Over the period 1993–2013, and after correcting for GIA, the observed global mean sea-level (GMSL) change is 3.2 ± 0.5 mm/yr and the modelled GMSL change from the CMIP5 multi-model ensemble is 3.1 ± 0.5 mm/yr, a result which suggests that on a global scale observations and model results are in good agreement within the $\pm 1\sigma$ uncertainty. However, differences among individual models and between observations and models are larger on a regional scale (in some locations > 200%), particularly in the eastern equatorial Pacific. For some other regions, like the Indian and South Atlantic Ocean, the agreement between models and observations is better (ranging within $\pm 50\%$). The global RMS error of the ensemble of 8 CMIP5 models which contain all necessary fields to calculate RSL is 2.3 mm/yr, which is 73% of the observed global mean. The RMS error of the individual models ranges from 1.0–5.9 mm/yr. We conclude that while models perform well on a global scale against observations, they do not perform as well on a regional scale over the period 1993–2013.

Keywords: sea-level rise, climate change, satellite era, land-ice melting, GMSL, regional patterns

*(✉) giannos_komis@hotmail.com; ioannis.s.komis@gmail.com

Contents

1 Introduction

1.1 Brief outline

Sea-level has risen globally throughout the 20th century and it will continue to rise during the 21th century even if atmospheric temperatures stabilize and greenhouse gas emissions are hampered (Meehl *et al.*, 2005; 2012). A large number of the world's megacities are situated near the coasts—where rising sea-levels have the most profound impact—containing 10% of the global population (Anthoff *et al.*, 2006; Church *et al.*, 2010a). The primary contributor to sea-level rise is the thermal expansion of the oceans due to the increasing amount of heat being stored in the oceans as a result of the ever-increasing amount of anthropogenic greenhouse gases (GHGs) released in the atmosphere (Church and White, 2011). Secondly, observed sea-level rise is caused by the melting of land-ice originating from the Greenland and Antarctic Ice Sheets (GrIS and AIS), and mountain glaciers and ice caps (MGIC) across the globe. Groundwater depletion also contributes to sea-level rise (Wada *et al.*, 2012; 2016), while water impoundment behind dams contributes to sea-level fall (Chao *et al.*, 2008). Climate change induced sea-level change and increased frequency and intensity of extreme events is already endangering island nations in the Pacific Ocean. Societal impacts include flooding of coastal land, saltwater intrusion into surface waters and underground aquafiers, coastal erosion, and endangerment of vital infrastructure such as roads, bridges, subway tunnels, and oil and gas supplies (Nicholls and Cazenave, 2010).

A common misconception among laypersons is that sea-level rises uniformly around the world. This notion is erroneous, and the reason for that lies in a number of factors. Firstly, wind-driven ocean currents around the world—like the Gulf Stream in the Atlantic and the Kuroshio in the Pacific—alter the shape of the ocean surface as a result of changes in the wind patterns, which in turn are caused by differential heating and increasing global temperatures. Secondly, as the Earth's ice sheets in Antarctica and Greenland melt and lose mass to the ocean, their gravitational potential decreases as well. As the ice sheets attract less water, local sea-level near the ice sheets falls, while it increases more farther away from the ice sheets. Finally, the disappeareance of the northern hemisphere ice sheets that depressed the Earth's surface during the last ice age, has resulted in a rise of the Earth's crust in places like northern Canada and Scandinavia, while in other places, where the land was squeezed upwards during the ice age due to mantle redistribution, like the southern coast of England, has resulted in a sink of the Earth's crust due to the glacial forebulge, leading to greater sea-level rise at those locations (Mitrovica and Peltier, 1991; Gehrels and Long, 2008).

The above three processes describe in a nutshell why sea-level rise will not be uniform around the globe. Correctly estimating and understanding the processes outlined above is of paramount importance for the study of historical and future sea-level change. For the investigation of this question, scientists use, for instance, Atmosphere-Ocean General Circulation models (AOGCMs), in-situ data from tide-gauge observations, hydrographic profiling floats, and satellite altimetry observations. (Leuliette and Willis, 2011).

Due to the potentially catastrophic consequences that sea-level rise will have for coastal communities around the world in the near future—if no immediate is taken—the processes contributing to such rise must be clearly defined, established, and assessed by the scientific community. Complete and thorough knowledge of these processes will help policy makers and goverments to introduce appropriate adaptation and mitigation policies for the future. The research in this thesis seeks to contribute as much as possible with the data at hand to the global problem of sea-level rise.

Before providing a short review of the current research, we will first introduce the concept of *relative sea-level* (RSL).

1.2 Definition of *Relative Sea Level* (RSL)

There are two definitions of sea-level change: i) *absolute sea-level* change is the sea-surface height change with respect to the Earth's centre of mass which is measured by altimetry satellites (more in Section 2.1.1), and ii) *relative sea-level* is the difference between the ocean surface and the ocean floor, which is measured by tide-gauges, devices attached usually to the solid-earth surface along the coast around the world. In order to obtain *relative* sea-level changes from satellite altimetry, measurements have to be corrected for vertical surface displacement (Slangen, 2012). All sea-level change values in this thesis are *relative* sea-level changes (Figure 1).

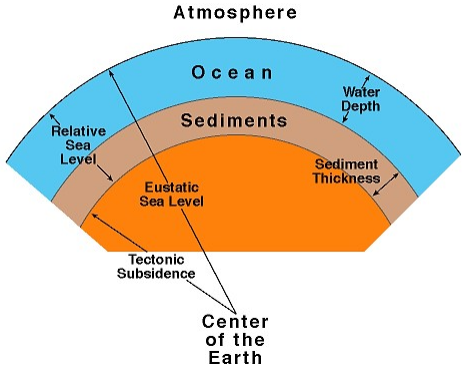

Figure 1. Schematic representation of RSL change (Source: http://strata.uga.edu/sequence/eustasyDefs.gif).

1.3 On RSL change during the satellite altimetry period (1993–present)

Since the introduction of high-precision satellite altimetry in 1993 at a nearly global reach ($\pm 66^o$), many studies have been conducted based on the data collected by TOPEX/Poseidon, Jason-1, Jason-2, and Envisat missions. Despite small deviations between different research groups, there exists very good agreement that the rate of change of global mean sea-level (GMSL) rise—and after correcting for the increasing size of the global ocean basins due to glacial isostatic adjustment (GIA) by -0.3 mm/yr (Peltier, 2009)—is around 3.2 ± 0.4 mm/yr over the period 1993–2012 (Church *et al.*, 2013); the level of precision of such an estimate is assessed based on various sources affecting altimetry measurements (see Section 2.1.3).

Comparing the 1993–2010 period to the late 20th century, it is found that the rate of observed GMSL for the former period is 3.3 mm/yr based on estimates from Leuliette and Scharoo (2010), Cazenave and Llovel (2010), and Beckley *et al.* (2010), while for the latter period (late 20th century) it is 1.8 mm/yr (Church and White, 2006). After the satellite data were calibrated with observations from a worldwide network of tide-gauge observations, it was found that any drifts in TOPEX/Poseidon, Jason-1, and Jason-2 (-0.1 ± 0.4 mm/yr) are consistent with no trend. A GMSL rise of 3.2 ± 0.4 mm/yr (GIA applied), over the period 1993–2009 has also been confirmed by Church and White (2011) based on satellite altimetry data; for the same period, in-situ data from tide gauge observations report a GMSL rise of 2.8 ± 0.8 mm/yr (Leuliette and Willis, 2011).

The European Space Agency (ESA) Climate Change Initiative (CCI) "Sea Level" project (henceforth SL_CCI), of which satellite altimetry data are used in this study, compiled a multi-mission satellite altimetry record from 1993–present applying a number of new improvements for which more details will be given in Section 2.1. They found similar GMSL trend to AVISO over the period 1993–2010 of 3.2 ± 0.5 mm/yr (Ablain *et al.*, 2015). The most notable result they achieved, through separation of ERS-1/ERS-2/Envisat and TOPEX/Jason-1/Jason-2 GMSL time series, is reducing the trend difference between the two time-series to 0.6 mm/yr compared to 1.5 mm/yr formerly (Ablain *et al.*, 2015).

1.4 Project description, aims, and gaps in previous research

RSL changes can be calculated by estimation of mass (land-ice, groundwater, reservoir storage) and volume (steric) changes of water. Based on CMIP5 (Coupled Model Intercomparison Project Phase 5) data, a climate model database (Taylor *et al.*, 2012), and independent data sets, local RSL changes can be calculated by summation of all the individual contributions at every grid point—taking into account gravitational and rotational aspects as well—over the satellite altimetry period at $1^o \times 1^o$ resolution. We will compare these modelled RSL changes with observed altimetry data from SL_CCI. Modelling RSL changes will be based on Slangen *et al.* (2012) and Slangen *et al.* (2014), but in this case compared to satellite data.

RSL changes over the satellite observational period, and more specifically over the period 1993–2013, with use of the newly assembled SL_CCI data set have not been studied in detail and compared to modelled results. As such we decided to follow a similar approach to Slangen *et al.* (2014)—which focused on relative sea-level change between 1961–2003—whereby observations of the individual contributions were compared to the total observations. In this thesis, a similar methodology is applied to the instrumental period 1993–2013, but with the use of more model data—for glaciers, dynamic ice sheets contribution, thermal expansion, groundwater depletion, and reservoir storage—and compared against the SL_CCI composite data set of all satellite missions to date. Chambers *et al.* (2016) paper also evaluate the GMSL budget over the period 1993–2014, and serves as a good basis for comparison between the current study and theirs. What is new about this study compared to previous research is the regional comparison we conduct with the aforementioned combination of observations and models. Some basic research question that we want to investigate are:

- Can the RSL budget over the period 1993–2013, between observations and modelled data, be closed with use of the new SL_CCI data set?,
- How close do these observations come to modelled results from CMIP5 results and independent data sets?
- Are observations and modelled results in good agreement both globally and regionally?
- Do these results agree with previously conducted research from other groups?.

1.5 Structure of thesis

This study is divided as follows: initially, in *Processes contributing to RSL change, and methodology* we present each individual contribution to RSL (mass, thermosteric, and GIA), and the methodology we follow to analyse and process the data, in addition, a description of the models used is also given (Section 2). The *Results* section is divided into observed RSL change, modelled RSL change, and a comparison of the two, on a global and regional scale. Finally, in the *Discussion* section, we place our results on a broader context and compare them against other studies, and in the *Conclusion* section we summarize our main findings.

2 Processes contributing to relative sea-level change, and methodology

This section will provide background information on RSL change research per individual contribution, along with a description of the methodology and data sets used for the calculation of the total modelled RSL change over the period 1993–2013. First, we introduce and describe the SL_CCI monthly RSL anomalies observations (Section 2.1). Secondly, we present the mass contribution (AIS and GrIS, MGIC, groundwater depletion and reservoir storage) and volume contribution (thermosteric) to RSL change in Section 2.2

and Section 2.3 respectively, and finally, we briefly present glacial isostatic adjustment (Section 2.4). In the final section (Section 2.5), the summation of all of the above contributions is discussed along with a treatement of how the associated uncertainties are calculated.

2.1 European Space Agency Climate Change Initiative (ESA CCI) data set

2.1.1 Measuring sea-level changes via satellite altimetry

Satellite altimeter missions measure sea surface height (SSH) relative to the center of mass of the Earth with 10-day repeat cycles along the satellite ground track, providing a continuous time series of absolute RSL height. The results must be corrected for vertical land movement to obtain relative RSL change, along with corrections related to atmospheric pressure variations and tidal cycles (Church and White, 2011).

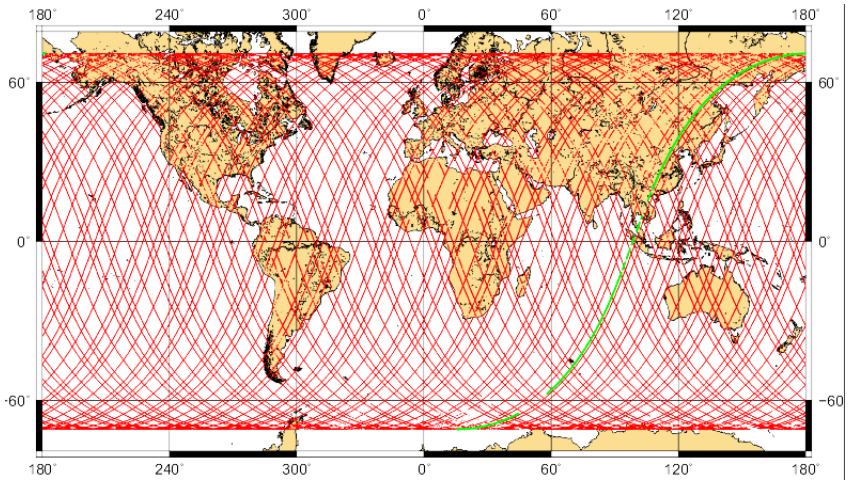

Figure 2. Earth's coverage by satellite altimetry during an orbital cycle of 10 days (Source: http://www.aviso.altimetry.fr/fileadmin/images/news/mod_actus/J1_new_orbit_GMT_pass1_127.png).

Advantages of satellite altimetry for the study of RSL change include their near global spatial coverage (Figure 2) of satellites compared to the sparse and mostly Northern Hemisphere coastal-areas-biased observations from tide gauges. In terms of climate change, satellite data are disadvantageous due to their relatively short time span (since 1993), which is not long enough to isolate decadal variabiliy from the trend (Frankcombe *et al.*, 2015). For instance, Palamisany *et al.* (2015) showed that removal of the Pacific Decadal Oscillation (PDO)/Interdecadal Pacific Oscillation (IPO) signal from the observed altimetry RSL data over the period 1993–2010/2012 resulted in a significant residual trend in the western tropical Pacific, which suggests that internal variability itself cannot explain the observed trends in the area, potentially signifying the presence of an anthropogenic fingerprint. However, in addition to PDO/IPO, the non-linear response of RSL to El Niño-Southern Oscillation (ENSO) also leaves a significant signal in the area (Palamisany *et al.*, 2015). This shows that despite their short time span, altimetry data are still valuable for the study of contemporary relative sea-level change, and have contributed greatly to our knowledge thus far.

2.1.2 SL_CCI data set description

In validating the modelled results for this study, we used the SL_CCI data set (Ablain *et al.*, 2015). The data set includes multi-mission satellite altimetry data over the period January 1993 to December 2013. This new project has implemented a number of improvements to the altimetry data including:

reduction of orbit errors, wet/dry atmospheric correction errors, reduction of instrumental drift and bias, intercalibration biases, intercalibration between missions and combination of the different RSL data sets, and an improvement of the references mean sea surface. The reprocessing of all satellite altimetry data available include ERS-1&2 and Envisat missions, in addition to TOPEX/Poseidon, Jason-1&2, and Geosat Follow-on (GFO) missions. The main product consist of monthly averaged sea-level anomalies (MSLA) at $0.25^o \times 0.25^o$ spatial resolution on a Cartesian grid, extending from $\pm 68.5^o$. The sea surface height (SSH) data have also been combined with other components for greater precision, including orbitography for the precise orbit determination, geodesy (geoid, mean sea surface, GIA), atmosphere (pressure, wind, dry and wet troposphere), and ocean (tides, sea state) (Ablain *et al.*, 2015).

We converted the initial $0.25^o \times 0.25^o$ resolution data set via bilinear interpolation at a $1^o \times 1^o$ resolution grid to match the modelled RSL changes which are also at a $1^o \times 1^o$ grid. Initially, we encountered some problems with the grid conversion, which originated from the bilinear interpolation algorithm used in *MATLAB*. These issues were later resolved with *CDO* (*Climate Data Operators* from Max-Planck-Insitut für Meteorologie, available at: https://code.zmaw.de/projects/cdo) instead of *MATLAB* to perform the bilinear interpolation.

2.1.3 Sources of errors and uncertainty in the SL_CCI data set

There are three main sources of errors affecting the estimation of global and regional sea-level anomalies according to the SL_CCI Error Report: 1) orbit computation, 2) wet troposphere correction, 3) altimeter instrumental parameters and linking altimetry missions together (Ablain and Zawadzki, 2014).

The main reasons errors are introduced in the orbit computation are the International Terrestrial Reference Frame (ITRF) and gravity field models. The current long term errors due to ITRF solution have been estimated to be ~1 mm/yr. After comparison of several orbit solutions that utilise different approaches to model gravity fields, the SL_CCI team has concluded that the upper bound of the error for regional sea-level anomalies is close to 1 mm/yr; differences at annual cycle close to 1 mm of amplitude for global RSL anomalies, and 5 mm for regional have also been observed.

The wet troposphere correction is derived from microwave radiometers on-board altimetric satellites; possible sources of contamination for this correction is by long-term instrumental drifts caused by internal temperature changes induced by yaw maneuvers or errors introduced by turning off the instrument (Ablain and Zawadzki, 2014). In terms of GMSL trend differences between radiometer and models, the uncertainty is close to ± 0.3 mm/yr over the altimetry period.

Altimeter instrumental parameters such as instrumental ageing and errors in the ground processing impact the long-term evolution (> 10 years) of GMSL by <0.1 mm/yr. Finally, errors arising from linking different missions together also have to be taken into account. Differences in the ground processing, for instance, introduced errors between TOPEX-B and Jason-1 (1 mm) missions, Jason-1 and Jason-2 (0.5 mm), and TOPEX-A and TOPEX-B (2 mm) (Ablain and Zawadzki, 2014).

In conclusion, the total error budget of the long-term evolution of GMSL over the altimetry period is ± 0.5 mm/yr (Ablain *et al.*, 2009).

2.2 Mass contribution

2.2.1 Land-ice contribution

2.2.1.1 Mountain Glaciers and Ice Caps (MGIC) and the glacier model Mountain glaciers and ice-caps (MGIC) include all land-ice except the AIS and the GrIS. Most of these glaciers are located in warmer and wetter climates than the two large ice sheets, leading to large mass turnover, a short response time, and large climate sensitivity (Abdalati, 2006). MGIC are located in regions where annual snow

fall exceeds the annual melt and under the influence of its own weight and temperature variations, the snow turns into ice (Slangen, 2012). A substantial net loss of ice has been observed in the majority of northern high latitude glaciers over the 20th and 21th century (Dyurgerov and Meier, 2005; Abdalati, 2006). The net mass gain or loss over the MGIC areas determines their total mass balance, if the mass balance is zero it means they are in equilibrium with climate. The evolution of MGIC and their response to climate change are modelled by using scaling methods by knowing the geometric features of glaciers, such as length or the surface area, and their relation to the volume of the MGIC. Volume-length scaling, volume-area-length scaling, and volume-area scaling use empirical relations derived from a small set of MGIC and then extrapolated to a global scale and supported by simple physical principles of the material properties of ice (Slangen, 2012). The sea-level equivalent (SLE) of the total volume of all glaciers in the world has been estimated to be 0.4 m by Grinsted (2013) using multivariate scaling relationships to estimate glacier volume from glacier inventory data, 0.6 m by Radic´ and Hock (2010) using scaling relationships, and 0.4 m by Huss and Farinotti (2012) using a new physically based flux balance approach.

Meier (1984) recognised MGIC as significant contributors to GMSL. Vaughan *et al.* (2013) confirmed that as well, after an extensive analysis of a global MGIC inventory, and concluded that MGIC will very likely continue to be significant contributors to RSL rise for years to come. The RSL contribution of all glaciers over the period 1993–2009, excluding those at the periphery of the Antarctic and Greenland ice sheets, is estimated to be 0.8±0.4 mm/yr (Church *et al.*, 2013).

As the task of measuring the volume of all glaciers around the world is quite daunting and near impossible, we use a theoretical technique, the product of which is Equation 1, which scales up local observations to general statements by statistically valid relationships to other known quantities, such as surface area (Bahr *et al.*, 1997). The following methodology is taken from Slangen and Van de Wal (2011). In this glacier model,we use a volume-area scaling approach based on Bahr *et al.* (1997), Van de Wal and Wild (2001), and Radic´ *et al.* (2007; 2008), whereby the volume V of the glacier is related to the surface area S by the power law below:

$$V = cA^{\gamma} \tag{1}$$

where c and γ are scaling parameters (for a full derivation of Equation 1, readers can refer to Bahr *et al.* (1997)). For glaciers, we use a value of γ=1.375, while for ice caps we use γ=1.25 (Bahr *et al.*, 1997). For c the value of $0.2055m^{3-2\gamma}$ is used for glaciers, and $1.7026m^{3-2\gamma}$ for ice caps (Radic´ and Hock, 2010). The above power law holds for glaciers in steady-state, but under non steady-state conditions the power law might change as the mass-balance profiles change and thus negatively affect the use of volume-area scaling for modelling the response of glaciers to future climate warming (Radic´ *et al.*, 2007; validated also by Van de Wal and Wild, 2001 but only for steady-state conditions). The volume change ($\frac{dV}{dt}$) of all glaciers is computed based on changes of glacier area (A) in time (t), and temperature (ΔT) and precipitation (ΔP) changes based on an initial glacier inventory by using the following relation:

$$\frac{dV}{dt} = \sum_{j=1}^{n}\sum_{k=1}^{m} A\,(j,k,t) \times \left\{ \Delta T_s\,(j,t)\,\frac{dB_{P(j,t)}}{dT_s} + \Delta T_{ns}\,(j,t)\,\frac{dB_{P(j,t)}}{dT_{ns}} + \Delta P\,(j,t) \right\} \tag{2}$$

where glacier area A is summed over n regions and m size bins. The mass balance sensitivity $dB_{P(j,t)}$ is a function of the local precipitation P, based on the relations from Zuo and Oerlemans (1997) below (Equation 3 and 4):

$$\frac{dB}{dT_s} = -0.259P^{0.427} \tag{3}$$

$$\frac{dB}{dT_{ns}} = -0.387P^{0.683} + 0.259P^{0.427} \tag{4}$$

$dB_{P(j,t)}$ is also dependent on changes in local summer temperature change (ΔT_S)—JJA is NH summer, DJF is SH summer—as well as non-summer temperature change (ΔT_{ns}). T and P are time-dependent and as such the mass balance sensitivity changes over time as well. Equation 2 also requires information on present-day area and volume of the glaciers. The reader is referred to Slangen and Van de Wal (2011) for a description of the glacier inventories used to obtain surface area data, as well as how glaciers are divided per region.

We use monthly global RCP4.5—Representative Concentration Pathway $4.5 W/m^2$ in 2100 relative to pre-industrial values—T/P data from 16 CMIP5 models to run the glacier model and calculate the MGIC contribution to RSL change over the period 1993–2013 per model using the nearest neighbour approach (Slangen and Van de Wal, 2011; Slangen *et al.*, 2012). For the climatology, we use the period 1983–2003, which sets 1993 as the starting year for the future contribution. The future contribution is set to 2013. To obtain the sea-level contribution from MGIC, we convert volume changes in m^3 obtained from Equation 2 to sea-level equivalent (mm) as outlined in Appendix A. We use the results from the glacier model to run the sea-level model (Section 2.2.3) and calculate the resulting RSL pattern. Table 1 summarizes the locations of all MGIC used in this study, based on Slangen and Van de Wal (2011).

Table 1. Mountain glaciers and ice caps (MGIC) locations around the globe based on Slangen and Van de Wal (2011).

	Locations
r1	Canadian Arctic
r2	Alaska
r3	Iceland
r4	Svalbard
r5	Scandinavia
r6	Russian Arctic
r7	East Russia/NE Asia
r8	Central Europe
r9	South Russia/Caucasus
r10	Central Asia
r11	South America/Patagonia
r12	Africa
r13	New Zealand
r14	Greenland Ice Caps

2.2.1.2 Antarctic and Greenland ice sheet (AIS and GrIS) Accounting for ~58 m potential RSL rise if melted, Earth's largest ice sheets cannot be ignored (Vaughan *et al.*, 2013). They experience significant melt, which assists the ice flow towards the sea. Water enters the ocean either through meltwater runoff or iceberg calving. The surface mass balance (SMB) is a measure of net mass gain or loss at the surface. Factors that add mass are mainly snow accumulation but also water vapour deposition and rainfall, and those that remove mass are surface melt, melting beneath floating ice, calving and sublimation (Abdalati, 2006). As the climate warms, mass loss increases through the aforementioned processes.

In recent decades, dynamical discharges of ice at the ice-sheet margins have also been observed but they cannot be attributed to warmer air temperatures. Grounding line migration of the inland slope (Vaughan *et al.*, 2013) and thining of Antarctic and Greenland glaciers and ice-shelves (Pritchard *et al.*, 2009) caused by sub-ice-shelf melting induced by recent modification of the Circumpolar Deep Water (CDW) circulation (Faver *et al.*, 2014) is most likely responsible for these recent dynamical discharges of ice. Liu *et al.*

(2015) found that the total ice mass loss from basal melt is twice as high from that of iceberg calving of ice shelves and the two are connected. They concluded that thinning of outlet ice-shelves is associated with ocean-driven increased basal melt which can trigger increased iceberg calving. Though ice shelves have negligible effect on RSL rise, they support the grounded ice upstream and have been proven to play a stabilizing role in the discharge of grounded ice to the ocean, which does have an effect on RSL rise (Dupont and Alley, 2005; Liu *et al.*, 2015). We can measure these mass discharges, volume changes, and gravitational perturbations of ice sheets by remote satellite platforms (Wingham *et al.*, 1998; Bentley and Wahr, 1998; Rignot and Thomas, 2002). The average rate of combined contribution—SMB and dynamical discharges—to RSL change over the period 1993–2010 from Antarctica and Greenland was 0.6±0.2 mm/yr (Shepherd *et al.*, 2012; Vaughan *et al.*, 2013).

In this study, we use results from the IMBIE 2012 project to calculate the contribution of AIS and GrIS to RSL change over the period 1993–2013. IMBIE is an international collaboration of polar scientists, providing improved estimates of the ice sheet contribution to sea-level change (available at: http://imbie.org/). They combined an ensemble of satellite altimetry (19 years; 1992–2011), interferometry (19 years), and gravimetry (8 years) data sets using common geographical regions, time intervals, models of SMB (32 years of simulations) and GIA to estimate the mass balance of Earth's polar ice sheets. The ice sheets were divided into East Antarctic Ice Sheet (EAIS), West Antarctic Ice Sheet (WAIS), Antarctic Peninsula (APIS), and Greenland Ice Sheet (GrIS) (Shepherd *et al.*, 2012).

Ice sheet surface mass balance (SMB) includes solid and liquid precipitation, surface sublimation, drifting snow transport, erosion and sublimation, and meltwater formation, refreezing, retention, and runoff. IMBIE estimates for the AIS and GrIS SMB were accomplished with the use of RACMO2 regional atmospheric climate models over the period 1979–2010. The spatial uncertainty of the RACMO2 mean SMB was assessed with the help of in-situ observations, and temporal uncertainty was assessed through comparison with global atmospheric reanalyses (Shepherd *et al.*, 2012). For this current study, the IMBIE data set was linearly extrpolated to 2013 with the average rate of 2005–2010 for Antarctica, and the average rate of 2006–2011 for Greenland. We used different time intervals for the average rates because the GrIS record was longer than the AIS.

We use RSL contribution data from the AIS and GrIS based on the IMBIE 2012 project (Shepherd *et al.,* 2012)—which includes SMB, dynamic ice sheet contribution, and GIA from the two major ice sheets—to run the sea-level model (Section 2.2.3). We do not calculate the SMB separately for each of the 16 CMIP5 models, based on temperature and precipitation data, as we do for MGIC because all information we need to calculate the contribution from ice sheets is included in the IMBIE 2012 data set. All dynamic ice sheet contribution from Greenland is located in the South-east coast, while for Antarctica, we divide the dynamic ice sheet contribution per region based on Katsman *et al.* (2011) : Amundsen Sea Embayment (60%), North Atlantic Peninsula (33.3%), and East Antarctic Glaciers (6.6%).

2.2.2 Groundwater depletion and reservoir storage

Terrestrial water storage refers to any non land-ice continental water that contributes to RSL change. This definition includes surface storage (lakes, rivers, wetlands, reservoirs), subsurface storage (groundwater, soil water), and snowpack storage (Meehl *et al.*, 2007; Pokhrel *et al.*, 2012). The great majority of the estimates regarding climate-related changes in land water storage in the last century are based on global hydrological models, as direct observations are difficult due to the diversity in size and location of sources and sinks (Milly *et al.*, 2010). There are also terrestrial water storage changes which are not associated with human-induced climate change, and are related to climate-driven variability in rainfall, evaporation, and runoff. Such changes are not part of this study, however it is worth mentioning that in a recent study by Reager *et al.* (2016), they found that climate variability resulted in an extra 3200±900 Gt of water being

stored on land, which consequently slowed the rate of RSL change over the period 2002–2014 by 0.7±0.2 mm/yr (Reager *et al.*, 2016).

Groundwater depletion can have negative impacts on water supply, but it can also result in land subsidence, reductions in surface water flows and spring discharges, and loss of wetlands (Bartolino and Cunningham, 2003; Konikow, 2011). Konikow (2011) assessed that human-induced groundwater depletion contributed 0.3±0.1 mm/yr to GMSL rise over the period 1993–2008 based on observational methods, while Wada *et al.* (2012) argued that for the same period and using water flux models the net—including renewable (groundwater recharge) and non-renewable groundwater (pumping in excess of recharge)—GMSL change due to human-induced water depletion was 0.5±0.1 mm/yr. There is no significant long-term trend in recent decades in climate-related changes in water and snow storage on land but direct human intervention through reservoir impoundment and groundwater depletion has contributed several tenths of mm/yr of RSL change (Church *et al.*, 2013).

In this study, we use the Wada *et al.* (2012) data set for the contribution of groundwater depletion to RSL change. This data set includes a reconstruction of past groundwater depletion and its contribution to global RSL variation based on three combined socio-economic and climate scenarios (SRES) with transient climate forcing from three General Circulation Models (GCMs). The data set was revised by Wada *et al.* (2016) because initially, they had assumed that 100% of the extracted groundwater ends in the oceans mostly based on pure knowledge of the undertaken pathways and mechanisms that control the fate of the pumped water. However using a coupled climate-hydrological model simulation—a state-of-the-art global climate model, the National Center for Atmospheric Research Community Earth System Model (CESM)—they demonstrated that only 80% of the groundwater ends up in the ocean, and the rest 20% remains on land, returning in the course of time back to soil and grounwater storage as infiltration and recharge from precipitation, and irrigation (Wada *et al.*, 2016). As such, the contribution from groundwater depletion to RSL change in this study over the period 1993–2013 was reduced from 0.5±0.1 mm/yr to 0.4±0.1 mm/yr.

Dams and artificial reservoirs contribute to RSL fall. The rate of RSL change from water impoundment behind dams was around -0.5 mm/yr in the 1980s but decreased to -0.3 mm/yr due to less dams being constructed (Chao *et al.*, 2008). Based on Milly *et al.* (2010) and Wada *et al.* (2012), water impoundment is decelerating, while groundwater depletion is accelerating, signaling an increase in the future net terrestrial water storage (Slangen, 2012). An estimation based on the construction of 30,000 reservoirs during the 20th century had as a result the reduction of GMSL at an average rate of -0.6 mm/yr during the past half-century after inclusion of groundwater seepage (Chao *et al.*, 2008).

After compiling an all-inclusive record of all dams constructed from 1901 to 2007 based on data from the International Commision of Large Dams (ICOLD) World ReGrISter of Dams, Chao *et al.* (2008) proceeded to calculate the total volume of water impoundment in the world's reservoirs with the following equation:

$$V(t) = \sum_i V_i H(t - t_i)$$

where t is any given calendar year, V_i is the capacity of a given individual reservoir modelled as an addition to V in year t_i of its completion, and H is the Heaviside function. The corresponding global RSL drop is given by:

$$d(t) = \frac{-V(t)}{A}$$

where $A = 3.6 \times 10^8\, km^2$ is the total ocean area (Chao *et al.*, 2008). In this study, we extrapolate Chao *et al.* (2008) data set from 2008 to 2013 by taking the average rate of 2002–2007, and using it to calculate the change over the period 2008–2013.

2.2.3 The sea-level model

As the ice sheets retreated following the Last Glacial Maximum (LGM), their meltwater increased the volume of the ocean; however, not all submerged indicators of shorelines of the same age lie at the same present-day elevation, indicating that the sea-level did not rise uniformly relative to the land (Clark *et al.*, 1978). This nonuniform sea-level rise would be larger farther away from the ice sheets, as the reduced ice load caused gravitational disequilibrium (Walcott, 1972). As surface ice melts, mantle flows to compensate for the changing surface-mass load distribution, this combined mass transfers affect the geoid. As mass has the property of attracting other masses around it, ice sheet on a continent attract ocean waters. Hence, the water in the vicinity of the ice sheet is elevated compared to a scenario whereby gravitational attraction was absent. If the ice sheets melts, then this gravitational attraction also disappears (Vermeersen and Sabadini, 1999). Mitrovica *et al.* (2001) conducted an experiment in which an imaginary melting event in Greenland contributed 1 mm/yr of eustatic sea-level rise. In that case, sea-level will fall in the vicinity of Greenland and it will rise by less than 0.2 mm/yr in Newfoundland, Britain, and Fennoscandia, while maximum sea-level rise of 1.3 mm/yr was obtained in north Pacific and southern Atlantic. They ascribed this nonuniform redistribution of sea-level to self-gravitation in the surface mass load, with water pilling up in the near field of an ice mass due to gravitational attraction. As the ice melts the ocean will relax and water will tend to flow from the near field to the far field (Mitrovica *et al.*, 2001). The aforementioned process will be shortly presented through the following derivation based on Farrell and Clark (1976), Clark *et al.* (1978), and Vermeersen and Schotman (2009).

If an ice sheet, modelled as a point source (Figure 3), was to melt, the meltwater will be distributed uniformly over the ocean in absence of gravitational effects. Sea-level would then rise by an amount, ε_e:

$$\varepsilon_e = \frac{M_I}{A_w \rho_w} \tag{5}$$

where ε_e is the global average sea-level change, ρ_w is the density of the water, A_w is the total surface area, and M_I is the mass of ice. In an ideal state, where the ocean is absolutely calm and no motion is observed, one can imagine eustatic sea-level as the average sea-level state. However, even in that case, the "true" sea-level change is different from the eustatic sea-level change. The reason lies in the properties of bodies that have a mass. Based on Newton's Law, mass attracts other mass and consequently land-ice attracts ocean water as described above. Hence, sea-level is elevated closer to the ice sheet and drops farther away from it. So, if the land-ice melts, the resulting sea-level pattern will not only be a result of the redistribution of meltwater over the oceans, but also because the gravitational properties of the melted land-ice have seized to exist.

We consider a spherically symmetric, nonrotating Earth with radius R and mass $M_E = \frac{4}{3}\pi R^3 \rho_E$, where the effect of self-gravitation of ice and water is not negligible. As such, the gravitational potential ϕ_g at radial distance r for points on the Earth's surface or outside is:

$$\phi_g(r) = \frac{GM_E}{r} \quad (r \geq R) \tag{6}$$

where $G = 6.7 \times 10^{-11}\, m^3 kg^{-1} s^{-2}$ is the gravitational constant. Imagine now that an ice sheet of mass M_I is formed in a point mass at the Earth's surface, ϕ_g will change according to the radius r and angular distance θ from the ice sheet, this change will be given by:

$$\phi_g^*(r,\theta) = \frac{G(M_E - M_I)}{r} + \frac{GM_I}{\sqrt{r^2 + R^2 - 2Rr\cos\theta}} \tag{7}$$

and if $r = R$, Equation 7 can be rewritten as:

$$\phi_g^*(R,\theta) = \frac{G(M_E - M_I)}{R} + \frac{GM_I}{2R\sin(\theta/2)} \tag{8}$$

The undisturbed sea-level is at $r = R$, and the sea-level after building up of the ice sheet is at $r = R + \varepsilon(\theta) + S_e$. The constant S_e ensures conservation of mass. Since Equation 8 is θ-dependent, a solution whereby sea-level distributes uniformly is no longer a possible as ϕ_g^* is not radially symmetric anymore. A new equipotential surface can be found through:

$$\phi^*(R+\varepsilon,\theta) = \phi(R) \tag{9}$$

We use a Taylor-expansion to describe the variation of the gravitational potential with r. Since $M_E \gg M_I$, and hence $R \gg \varepsilon$, to first order in ε we can write:

$$\phi^*(R+\varepsilon) = \phi^*(R,\theta) + \varepsilon \frac{\partial \phi^*(R,\theta)}{\partial r} + \ldots \approx \phi^*(R,\theta) - \varepsilon g \tag{10}$$

Note that the gravitational acceleration at the Earth's surface $g = 9.8\, m/s^2$ is by definition the derivative of the gravitational potential. To first order, the gradient of the gravitational potential does not change for values of θ that are not small:

$$\frac{\partial \phi^*}{\partial r} = \frac{\partial \phi}{\partial r} = -g \tag{11}$$

Thus to first order we get

$$\varepsilon(\theta) = \frac{\phi^*(R,\theta) - \phi(R)}{g} \tag{12}$$

and with g being

$$g = \frac{GM_E}{R^2} \tag{13}$$

ε can be expressed, in combination with Equation 8, as:

$$\varepsilon(\theta) = \frac{M_I R}{M_E}\left(\frac{1}{2\sin(\theta/2)} - 1\right) \tag{14}$$

After the ice sheet has been formed, the surface at θ-dependent radial distance $r = R + \varepsilon$ is an equipotential surface. But if $r = R + \varepsilon$ forms an equipotential, then for any constant $S_e \ll R$ also $R + \varepsilon + S_e = R + \varepsilon_1$ forms an equipotential, then $r = R + \varepsilon$ is not a unique equipotential surface. Mass conservations must restrict the new sea-level that coincides with the equipotential i.e. any mass extracted from the ocean must be equal to the mass that turns into the ice sheet given by:

$$\int_0^{2\pi}\int_0^{\pi} (\varepsilon + S_e)\, dV = -\frac{M_I}{\rho_w} \tag{15}$$

where $dV = r^2 \sin\theta dr d\theta d\phi$, and it follows that:

$$4\pi R^2 S_e + 2\pi R^2 \int_0^{\pi} \varepsilon \sin\theta d\theta = -\frac{M_I}{\rho_w} \tag{16}$$

From Equation 16, the expression for the eustatic sea level change can be found:

$$S_e = -\frac{M_I R \rho_E}{M_E 3 \rho_w} \tag{17}$$

where $\rho_E = 5500\,kg/m^3$ is the mean density of Earth. Combination of Equation 14 and Equation 17 results in the actual sea-level change as difference in radial distance between the initial and the final sea-surface:

$$\varepsilon^*(\theta) = \varepsilon(\theta) + S_e = \frac{M_I R}{M_E}\left(\frac{1}{2\sin(\theta/2)} - 1 - \frac{\rho_E}{3\rho_w}\right) \tag{18}$$

Equation 18 describes the sea-level change with self-gravitation taken into account and the sea-level change as a consequence of the loss of ocean mass and addition of ice mass. The ratio between actual sea-level change with gravitational effect (ε^*) to eustatic sea-level change (S_e) is given by H in Equation 19:

$$H = \frac{\varepsilon^*}{S_e} = \left(\frac{1}{2\sin(\theta/2)} - 1 - \frac{\rho_E}{3\rho_w}\right) / \frac{\rho_E}{3\rho_w} \tag{19}$$

From Equation 19, it can be computed that the sea-level will fall as a result of ice melt within a distance up to 20^o (~2200 km) from the former ice sheet (Figure 4). Within 60^o (~6700 km), sea-level will rise less than if the amount of water from the ice sheet had been distributed eustatically over the oceans (Farrell and Clark, 1976; Vermeersen and Sabadini, 1999; Slangen, 2012). Note that H is not dependent on the mass of the ice sheet, but only on the ratio between the density of the Earth and the density of ocean water.

Farrell and Clark (1976) postulated that given a spherically symmetric viscoelastic Earth model, the time-depending change in separation between Earth's surface and the geoid caused by a point load placed on the Earth's surface can be computed (Peltier, 1974; Clark *et al.*, 1978), and as such describing a method by which sea-level patterns can be calculated. For a realistic spatial distribution of these sea-level patterns, the load is considered to be a collection of point loads, and the effects are added. If the load is time-dependent, the effects of past loads are added to the effects of the present loads, and the history of sea-level change relative to the deforming surface of the solid Earth is given by S at time t and position vector $r(\lambda,\phi)$, where λ denotes longitude and ϕ denotes latitude, and can be described as follows:

$$\begin{aligned} S(t,r) \;=\; & \iint_{Ocean} G^E(r-r')\,\rho_w s(t,r')\,d\Omega' + \iint_{Ice} G^E(r-r')\,\rho_i I(t,r')\,d\Omega' \\ & + \int_{18{,}000BP}^{t} d\tau \iint_{Ocean\&Ice} G^V(t-\tau, r-r') \times \left[\rho_w s(t,r') + \rho_i I(t,r')\right] d\Omega - k_E(t) - k_c(t) \end{aligned} \tag{20}$$

where G^E is the immediate-response elastic Green function, G^V is the time-dependent viscous Green function, ρ_w is the density of water, ρ_i is the density of ice, I is the ice thickness, $d\Omega'$ is an element of area, k_E corrects for the oceanwide average rise in RSL (eustatic rise), k_c assures that mass is conserved, and the notation $r-r'$ indicates the angular distance between position vectors r (where the load change takes place) and r' (the point under consideration) (Clark *et al.*, 1978). The first term in Equation 20, is the immediate sea-level change caused by changes in water load. The second term takes into consideration the immediate elastic sea-level response due to the change in ice load, and the third term represents the slow deformation of the Earth from changes in both ice and water loads.

The effects of gravitation, solid-earth deformation, and rotation are included in the sea-level model (Schotman, 2008) we use in this thesis. The sea-level equation above is solved by the model utilizing a pseudo-spectral approach as outlined by Mitrovica and Peltier (1991). The Earth model is elastic, compressible, and radially stratified based on the Preliminary Reference Earth Model (PREM) (Dziewonski and Anderson, 1981). Since our investigation includes processes with timescales less than a century, the above solid-Earth elastic approach is permitted. In addition, during the 21-year period we study the ocean surface does not increase or decrease drastically, hence the model we use does not account for moving coastlines, and the ice and ocean density remain fixed (Slangen, 2012).

Furthermore, mass variations on the Earth's surface cause variations on the Earth's rotation rate and the position of the rotation axis (Vermeersen and Sabadini, 1999). As all terms in Equation 20 are

interconnected and dependent upon each other, sea-level changes from mass changes—as discussed in Section 2.2.1.1 and Section 2.2.1.2 above—are not calculated at once in the sea-level model. As mass is added to the ocean the Earth's crust gets depressed; the Earth's gravitational field and rotation changes accordingly leading to redistribution of the water causing changes in the Earth's crust and rotational pattern (Slangen, 2012). This process results in sea-level fall close to the melt sources, and sea-level rise farthest away from them.

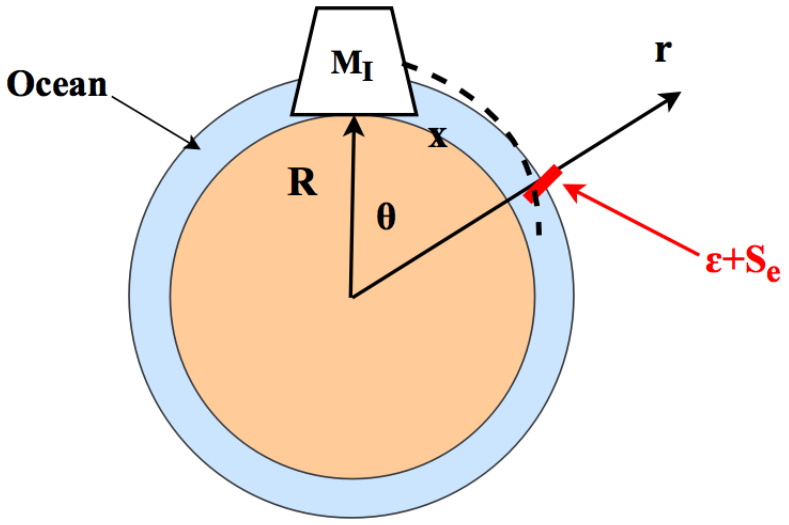

Figure 3. Conceptual configuration used to study the gravitational effect of an ice sheet, of mass M_I, on sea-level on a spherically symmetric, simplified Earth of radius R with uniform ocean. The dashed curve shows sea-level relative to the situation without an ice sheet, where $\varepsilon(\theta)+S_e=\varepsilon^*(\theta)$. The sea-level always coincides with an equipotential surface. Here $x=\sqrt{r^2+R^2-2Rr\cos\theta}$, θ is the angular distance from the ice sheet, and r is radial distance for points on the Earth surface or outside.

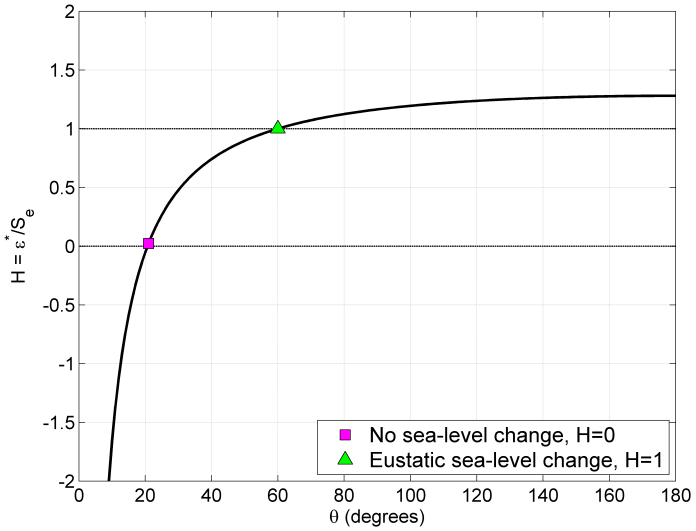

Figure 4. Ratio between actual sea-level change with gravitational effects (ε^*) and without gravitational effect (S_e) or eustatic sea-level. Square dot (20^o) shows where no sea-level change is observed (H=0). Triangle dot (60^o) shows where eustatic sea-level change is observed (H=1).

2.3 Thermosteric contribution

During the last 50 years, 90% of the heat absorbed by the Earth as a result of global warming has been stored in the oceans (Rhein *et al.*, 2013). As the ocean warms, sea-level rises. Given the same amount of heat input, warmer water will expand more than colder water; water of higher salinity will expand more than lower salinity water, and water at larger depth and consequently higher pressure will expand more as well (Church *et al.,* 2010). The collective density variations caused by temperature (thermosteric) and salinity (halosteric) changes are known as steric contribution to RSL change. The steric contribution signal results in highly varying RSL pattern. This variability occurs due to the coupling of density and ocean dynamics changes, as the ocean circulation transports heat and salt.

Measurements of the ocean heat content and thermal expansion have been conducted since the 1960s with the use of expandable bathythermographs (XBT). In the 1990s, the World Ocean Circulation Experiment (WOCE) offered the first and highest quality, global, top-to-bottom survey of ocean temperatures and salinity (Siedler *et al.*, 2001; Church *et al.*, 2010). In the 2000s, the ARGO program was launced and it deployed thousands of autonomous profiling floats, which collect high quality temperature/salinity profiles of the world oceans up to 2000m depth, at a fraction of the cost of the WOCE (Davis *et al.*, 2001; Gould *et al.*, 2004).

During the instrumental period 1993–2010, the observed contributions to GMSL change due to thermal expansion for the 0–700m depth range is 0.8±0.3 mm/yr, and 1.1±0.3 mm/yr when accounting for the deep ocean contribution (Church *et al.*, 2013).

We obtained globally averaged historical (1900–2100) and RCP4.5 thermosteric RSL change (*zostoga*) timeseries from 16 CMIP5 AOGCMs (see Appendix B Table 11). Monthly historical (~1850–2012) SSH above the geoid of local dynamic topography (due to water mass advection, thermohaline circulation, and wind-driven circulation), *zos* data could only be obtained for CanESM2, CNRM-CM5, CSIRO-Mk3.6.0, HadGEM2-ES, MIROC-ESM-CHEM, MIROC-ESM, MRI-CGCM3, and NorESM1-M. The *zos* data set is added to the *zostoga* in order to calculate the total modelled RSL change due to thermal expansion and ocean dynamics. The 16 CMIP5 AOGCMs are partitioned into 'complete' (Table 3) and 'incomplete' (Table 4) models. We chose this dichotomy because the 'complete' models contain all necessary field to calculate RSL patterns, while the 'incomplete' model lack the local dynamic topography (*zos*) field, and as such are only suitable for GMSL calculations, in contrary to the 'complete' which are suitable for both GMSL and spatial comparison. For the rest 8 models for which the *zos* field is missing, the ensemble mean *zos* field is calculated as the average from the 'complete' models (Table 3) and added to the 'incomplete' models (Table 4). The thermosteric data sets account for changes from the surface and up to 2000 m depth (Domingues *et al.*, 2008; Levitus *et al.*, 2012; Chambers *et al.*, 2016). Due to poor knowledge of the halosteric contribution during the 1990s, this component is neglected in this study.

2.4 Glacial Isostatic Adjustment (GIA) contribution

The Last Glacial Maximum (LGM) was ~24,500 years ago when large ice sheets (GrIS, FennoscandianIS, and LaurentideIS) covered much of Earth's northern hemisphere. Their mass load led to deformation of the viscoelastically-behaving (Maxwell body) solid earth. The elastic part of vertical deformation after a mass change works similar to a spring: it deforms instantaneously and completely when pressure is applied, and returns back to its initial shape when the pressure is no longer applied (Slangen, 2012). The enormous weight of the ice sheets caused the underlying mantle to flow away to the sides of the ice sheets, which consequently caused upward movement next to the ice sheets (peripheral bulges). Following the collapse of the FIS and LIS, RSL increased approximately by 120 m on average as meltwater returned to the ocean. Slowly the solid earth crust started to recover, returning to its initial position. In Scandinavia and Hudson

Bay, Canada maximum uplift rates of up to 1 cm/yr have been observed, leading RSL to fall (Peltier, 1999; Slangen, 2012).

The GIA signal must be taken into account when estimating ice sheet mass balance with either satellite gravimetry or satellite altimetry. In this study, we use the 1^o resolution, 0kyrBP GIA field from Peltier's ICE-5G (viscosity profile 2 with 90 km lithosphere, VM2 LM90) model version 1.2 (Peltier, 2004). ICE-5G, and its predecessor ICE-4G, is a refined model of the global process of glacial isostatic adjustment, for which an extensive review can be found in Peltier (2004).

2.5 Summation of contributions and treatment of uncertainty

In Sections 2.2–2.4, we described each of the modelled RSL change contributions. In order, to obtain the total field of modelled RSL change over the period 1993–2013, we add all of the above fields at every location at $1^o \times 1^o$ resolution using a land-ocean mask extending from $\pm 68.5^o$ in latitude (see Section 2.6 for a description of the land-ocean mask). The uncertainty in the total modelled RSL pattern is calculated as the sum of uncertainties per contributing data set. For MGIC and thermosteric contribution, the $\pm 1\sigma$ multi-model spread i.e. the variation in global mean among the 16 models, is used to calculate the mean MGIC and thermosteric contribution respectively, while for non model-specific datasets such as groundwater and reservoir storage, the uncertainty is calculated as 20% of the global mean. For ice sheets, the uncertainty is already given in Shepherd *et al.* (2012) data set. The total modelled RSL change uncertainty is given by Equation 21:

$$\sigma_{total} = \sqrt{(\sigma_{MGIC})^2 + (\sigma_{AIS})^2 + (\sigma_{GIS})^2 + (\sigma_{GW})^2 + (\sigma_{RS})^2 + (\sigma_{TS})^2 + (\sigma_{GIA})^2} \tag{21}$$

where GW stands for groundwater, RS for reservoir storage, and TS for thermosteric. The total GMSL budget is given by Equation 22:

$$GMSL(t) \pm \sigma_{total} = (GMSL_{mass}(t) \pm \sigma_{mass}) + (GMSL_{steric}(t) \pm \sigma_{steric}) \tag{22}$$

where $GIA \pm \sigma_{GIA}$ is zero and hence is omitted from the final GMSL calculation. In Figure 5, the methodology to calculate RSL patterns in this study is schematically summarized.

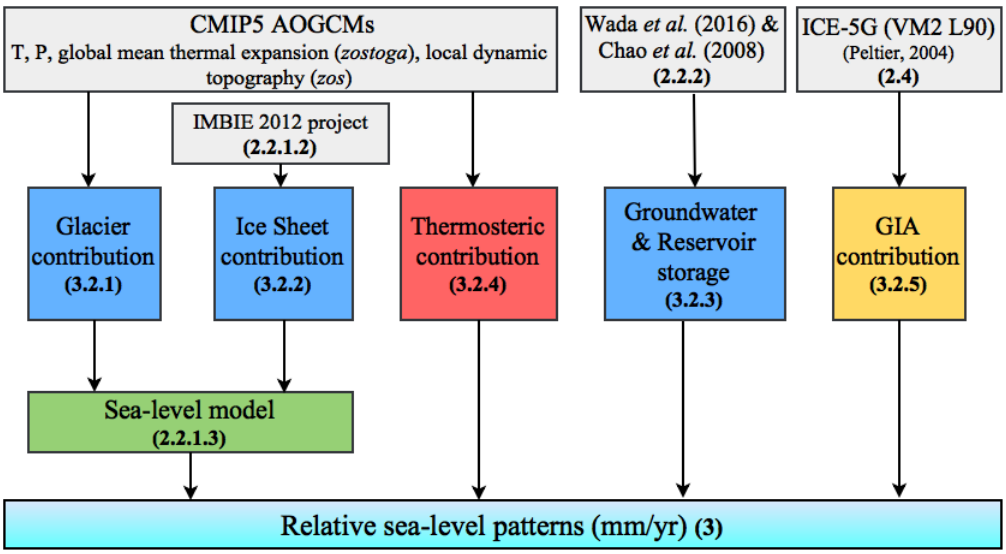

Figure 5. Schematic diagram with methodology followed in this study. Number in brackets indicated sections in this thesis in which contribution is presented.

2.6 Masking

For the purpose of homogeneity and comparison, we created a land-ocean mask based on the "worst" land-ocean mask found among the individual contribution data sets, namely that of *zos*. We also mask any data outside $>\pm 68.5^o$ to match the SL_CCI data set. The final figures are presented on a Miller Cylindrical projection overlaid with 0.25^o resolution coastlines extending from $\pm 68.5^o$ in latitude and 0.5^o–359.5^o longitude. The Miller Cylindrical projection has similar properties to that of a Mercator. It is a conformal map, that is it preserves local angles, and it is based on a tangent cylinder wrapped around the equator. Straight lines on this projection are rhumb lines i.e. the track followed by a course of constant bearing.

3 Results

3.1 Observed relative sea-level change (1993–2013)

Even though the global trend (3.2±0.5 mm/yr) over the period 1993–2013 suggests a rise in the mean sea-level, regionally we observe differences that range between ±10 mm/yr. The first point of interest in Figure 6 is the dark red region in SE Asia, east of Philipinnes, where RSL increased at a rate of >9.0 mm/yr over the period 1993–2013. The wider region surrounding Philipinnes, Papua New Guinea, and some parts of Indonesia experienced a rate of RSL change of the order of >6.0 mm/yr, that is a factor of ~2 larger than the GMSL rate of 3.2±0.5 mm/yr. These patterns in the western tropical Pacific are transient and mostly attributed to interdecadal climate variability (see *Discussion* section). Regions which experienced similar above average increases in RSL change over the period 1993–2013 are: the South Pacific off the coast of Antarctica (negative to zero trend; cyan-gray region), a small region NE of Japan (positive trend; dark red region), and a small section along the track of the Gulf Stream in North Atlantic (negative trend; blue-gray region), where sea-level increased around Greenland and decreased along the Gulf-Stream, a result of the North Atlantic dipole. In whole, there are only two locations were the RSL trend exhibited no significant trend, that is mainly in the eastern equatorial Pacific along the western coast of South America and USA, extending towards the center of the Pacific Ocean along the Equator. In addition, the observed RSL exhibited slight variations off the western coast of Canada, up to the coastline of Alaska and the Aleutian Islands (grey areas). Regional variations in observed and modelled sea-level change will be discussed in depth in Section 3.5.

In Figure 7a, a time-series of monthly observed RSL change over the period 1993–2013 is shown. The grey line represents the unfiltered time-series with the seasonal-cycle included. A least-square linear fit has been included (blue line) along with a 13-term moving average line (red line). The slope of the fit is 3.2±0.5 mm/yr. The amplitude of the interannual observed RSL (Figure 7b) fluctuates between ~±11.0 mm, with a few exceptions where it reaches ~+13.0 mm (marked by the green dot). A sudden "jump" possibly associated with the strong 1997/8 El Niño is also visible. A number of other points—marked by dots—indicate weak to moderate El Niño events (cyan and magenta dots) and one moderate La Niña event (yellow dot). All of the aforementioned points lie outside the 5–95% confidence intervals and coincidentally also correspond to periods where El Niño/La Niña events occured.

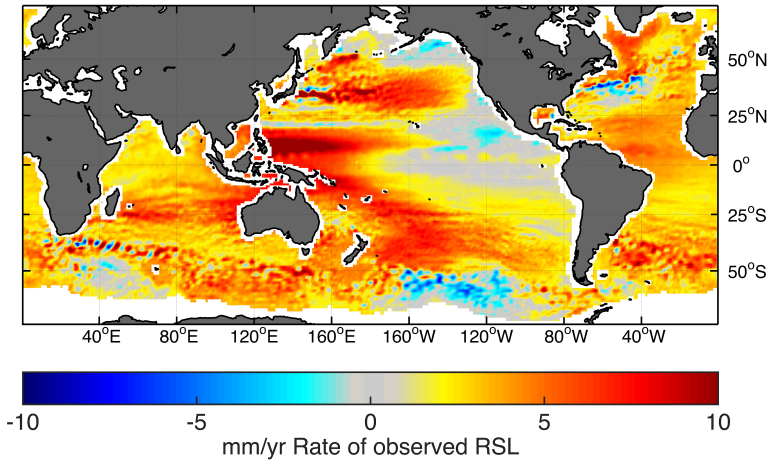

Figure 6. Total observed relative sea-level change (mm/yr) over the period 1993–2013 using SL_CCI data. Missing values in white.

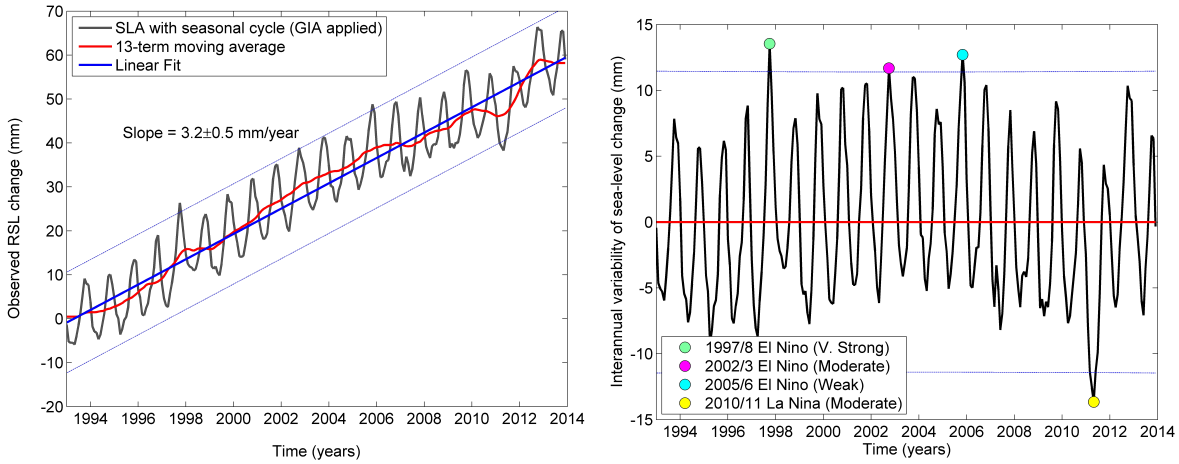

Figure 7. (a–left) Timeseries of total observed relative sea-level change (mm) over the period January 1993–December 2013. Grey line shows unfiltered signal of relative sea-level change with seasonal cycle included and 5-95% confidence bounds (blue dashed lines). Red line shows the 13-term moving average, and the solid blue line is the linear least-square fit. The slope is 3.2 ± 0.5 mm/yr. (b–right) Interannual variability of observed relative sea-level change (mm) with 5-95% confidence bounds (blue dashed lines) over the period January 1993–December 2013. Dots mark weak to very strong El Niño/La Niña events over this period.

3.2 Individual modelled contributions to relative sea-level change

3.2.1 Mountain glaciers and ice caps (MGIC) contribution

Mountain glaciers and ice-caps around the world contributed on average 0.9 ± 0.2 mm/yr of RSL rise over the period 1993–2013. In Figure 8, the multi-model mean MGIC contribution to RSL change over the period 1993–2013 is shown. RSL change due to MGIC is highest in the Indian, Pacific, and Atlantic Ocean as indicated from the 0.9–1.0 mm/yr contour, that is farthest away from the location sources mostly found in high latitudes as a result of gravitational disequilibrium (see Table 1 for specific locations of MGIC used

in this study). Lowest values are modelled close to Greenland and Arctic Canada (0.5–0.7 mm/yr), off the coast of Alaska, and at the straits between South America and Antarctica (also 0.5–0.7 mm/yr). Out of the total modelled RSL change of 3.1±0.5 mm/yr over the period 1993–2013, MGIC explain ~29% of the total change (see Table 5 in Section 3.3.3).

3.2.2 Antarctic and Greenland ice sheet (AIS and GrIS) contribution

In this section, we present time-series of AIS and GrIS contribution to RSL change over the period 1993–2013 based on Shepherd *et al.* (2012) (Figure 10a). We also present a global map of the RSL change (mm/yr) due to AIS and GrIS contribution over the same period after running the sea-level model with the IMBIE 2012 results (Figure 10b)

We convert ice mass loss (in Gt) from three different regions of Antarctica to sea-level equivalent (SLE in mm) following the methodology outlined in Appendix A. Each Antarctic region is not contributing to GMSL change equally, and as such each region is assigned a percentage contribution as outlined in Section 2.2.1.2. In total, Antarctica contributed 5.0±1.0 mm of RSL rise or 0.2±0.1 mm/yr over the period 1993–2013. Out of the total RSL rise contributed from Antarctica (black line), 3.0±0.6 mm (or 0.1±0.0 mm/yr) were contributed from the Amundsen Sea Embayment (ASE; blue line), 1.7±0.3 mm (or 0.1±0.0 mm/yr) from the North Antarctic Peninsula (NAP; red line), and finally, 0.3±0.1 mm from the East Antarctic Glaciers (EAG; cyan line), which is considered a negligible contribution over the period of study. A summary of the above can be found in Table 2.

The GrIS contributed 10.4±1.3 mm or 0.5±0.1 mm/yr of RSL rise over the period 1993–2013. The contribution from GrIS has accelerated in recent years as seen in Figure 10a from the increasing separation of the two signals (blue for Greenland and red for Antarctica) from ~2005 onwards. This increase in GrIS sea-level contribution has been attributed to acceleration of outler glaciers and decreasing SMB (increasing meltwater runoff), while mass losses from the WAIS are mainly due to dynamic discharges of ice at the ice sheet margin. Losses from the APIS have been attributed to ice-shelf collapse and calving-front retreat (Shepherd *et al.*, 2012). By the end of 2013, the contribution from Greenland (0.5±0.1 mm/yr) almost equalled the contribution from groundwater depletion (0.4±0.1 mm/yr) (Figure 12a)—consistent with other studies as well (Velicogna *et al.*, 2014; Yi *et al.*, 2015).

In total, AIS and GrIS contributed 15.4±2.0 mm or 0.7±0.2 mm/yr of RSL rise over the period 1993–2013. The largest RSL rise impact of the combined AIS and GrIS ice mass loss over this period, is farthest away from the two ice sheets (Figure 10b) resulting from the distribution of meltwater around the oceans and the loss of gravitational attraction of ice sheets. While in the vicinity of the ice sheets, RSL fall is observed as indicated from the dark blue regions in Figure 10b, the largest rate of RSL rise is observed within the range of the 0.8–0.9 mm/yr contours found in the Pacific, Indian, and Atlantic Ocean basins.

Though from Figure 10a, the total contribution from land-ice sources is 0.7±0.2 mm/yr, a higher value of 0.8 mm/yr is found in Figure 10b. This discrepancy has to do with the addition of the land-ocean mask to the data, which covered certain high latitudes areas that otherwise contribute negatively to the GMSL. As such the GMSL from land-ice sources increased; however, 0.7±0.2 mm/yr is the value we use in this study.

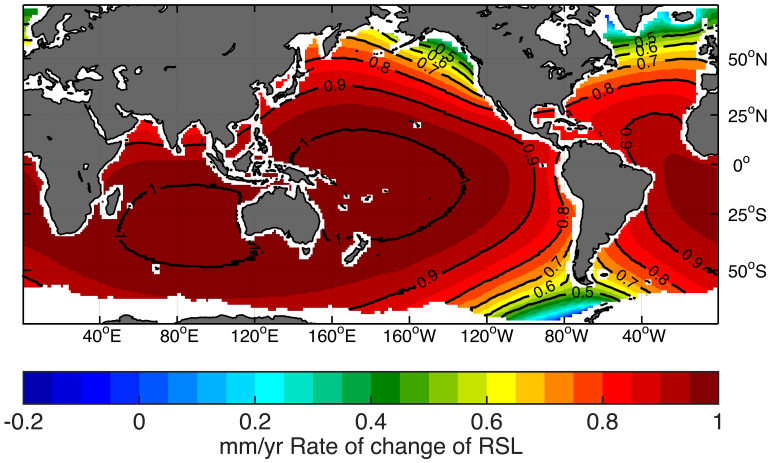

Figure 8. Multi-model (16 AOGCMs) ensemble mean of relative sea-level change (mm/yr) due to melting of mountain glaciers and ice-caps (MGIC) over the period 1993–2013. Missing values in white.

Table 2. Summary of AIS and GrIS total (dynamic and SMB) contribution to GMSL change over the period 1993–2013 based on data from Shepherd *et al.* (2012).

Region	**Sub-region**	**SLE (mm)**	**GMSL change (mm/yr)**	**Percentage (%)**
Antarctica	*Total*	5.0 ± 1.0	0.2 ± 0.0	–
	-Amundsen Sea Embayment	3.0 ± 0.6	0.1 ± 0.0	60%
	-North Antarctic Peninsula	1.7 ± 0.3	0.1 ± 0.0	33.3%
	-East Antarctic Glaciers	0.3 ± 0.1	0.0 ± 0.0	6.6%
Greenland	*Total*	10.4 ± 1.3	0.5 ± 0.1	–
Total	–	15.4 ± 1.6	0.7 ± 0.1	–

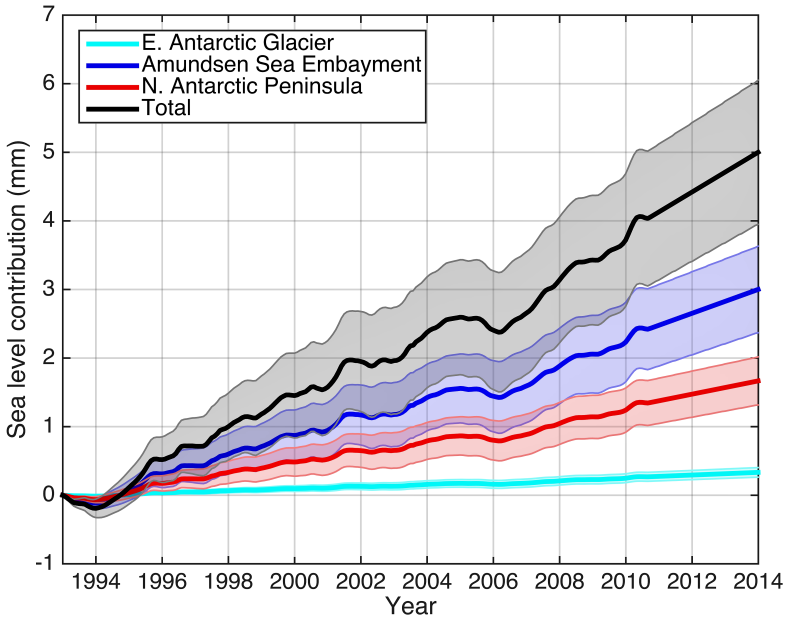

Figure 9. Sea-level equivalent (SLE in mm) contribution due to ice mass change from the East Antarctic Glaciers (cyan line), Amundsen Sea Embayment (blue line), North Antarctic Peninsula (red line), and the sum of the three (black line). Shaded areas indicate $\pm 1\sigma$ uncertainty. Data are taken from Shepherd *et al.* (2012); due to lack of measurements after 2011, the data sets have been linearly extrapolated to December 2013 with the average rate of the period 2006–2011.

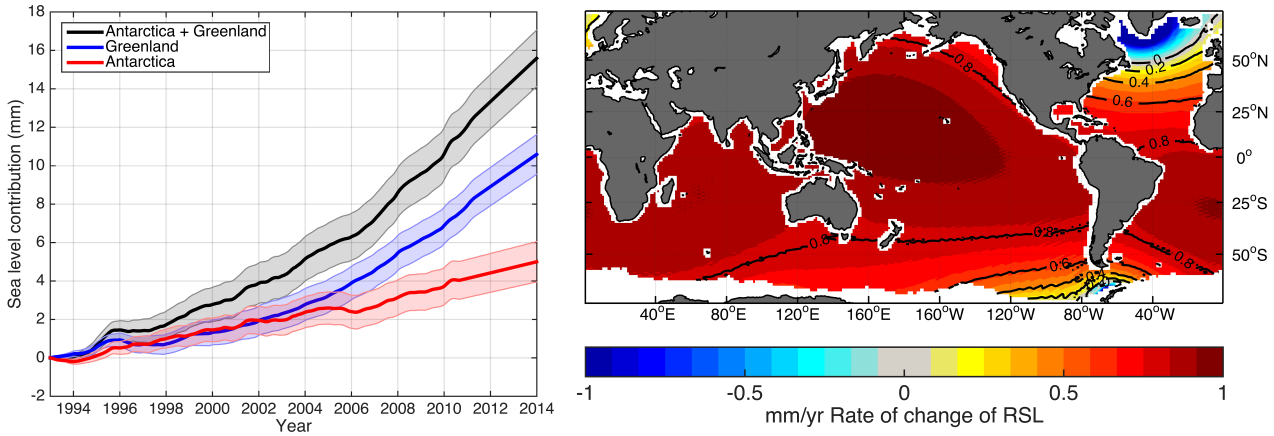

Figure 10. (a–left) Relative sea-level contribution (mm) from ice mass change in Antarctica (red line), Greenland (blue line), and Antarctica and Greenland (black line) over the period 1993–2013. Shaded areas indicate $\pm 1\sigma$ uncertainty. Data are taken from Shepherd *et al.* (2012); due to lack of measurements after 2010 (Antarctica) and 2011 (Greenland), the data set has been linearly extrapolated till December 2013 with the average rate of 2005–2010 for Antarctica, and the average rate of 2006–2011 for Greenland. (b–right) Relative sea-level change (mm/yr) due to contribution from AIS and GrIS over the period 1993–2013. Missing values in white.

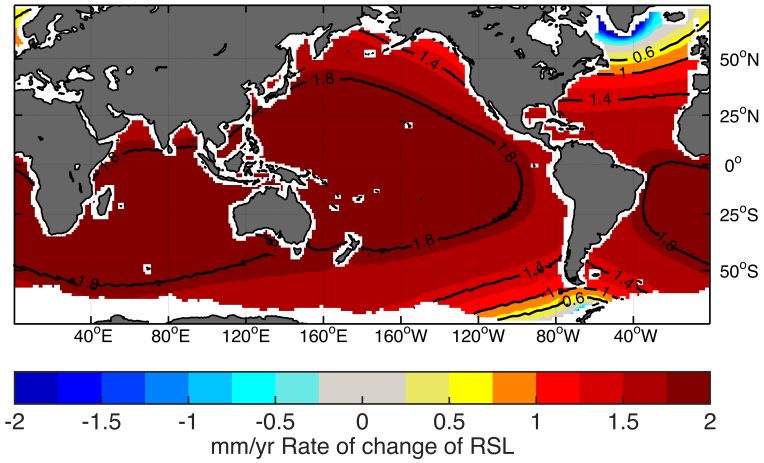

Figure 11. Relative sea-level change (mm/yr) due to melting of land-ice sources (MGIC, AIS, GrIS) over the period 1993–2013. Missing value in white.

3.2.3 Groundwater depletion and reservoir storage contribution

A global increase in reservoir construction (dams) and storage of water on land—for use in hydroelectric power production—since the beginning of the 20th century, led to 6.3 mm or 0.3 mm/yr of potential sea-level rise to be stored on land over the period 1993–2013 (Figure 12a; black line). This process slowed the rate of GMSL change as seen from the black line in Figure 12a. Over the same period, depleted groundwater, which eventually ended up in the oceans, contributed 10.5 mm or 0.5 mm/yr of RSL change (blue solid line), according to Wada *et al.* (2012) estimate; an estimate which was later corrected from Wada *et al.* (2016) to 80% of that value, that is 8.6 mm or 0.4 mm/yr of RSL change (blue dashed line) over the period 1993–2013. The total landwater contribution from groundwater depletion and reservoir storage is 0.1±0.1 mm/yr.

The main source locations of groundwater depletion are located along the coast of India, Bangladesh, Pakistan, Iran, and the SE Arabic Peninsula, and to a lesser extent along the Californian coast, in Figure 12b (dark blue regions) with values increasing to 0.1–0.2 mm/yr farthest away from the coast.

The RSL fingerprint (modelled by solving the sea-level equation) resulting solely from the addition of all modelled mass contributions to sea-level change over the period 1993–2013 is shown in Figure 13 and it identifies the location and magnitude of the sources, i.e. mainly from MGIC, and AIS and GrIS.

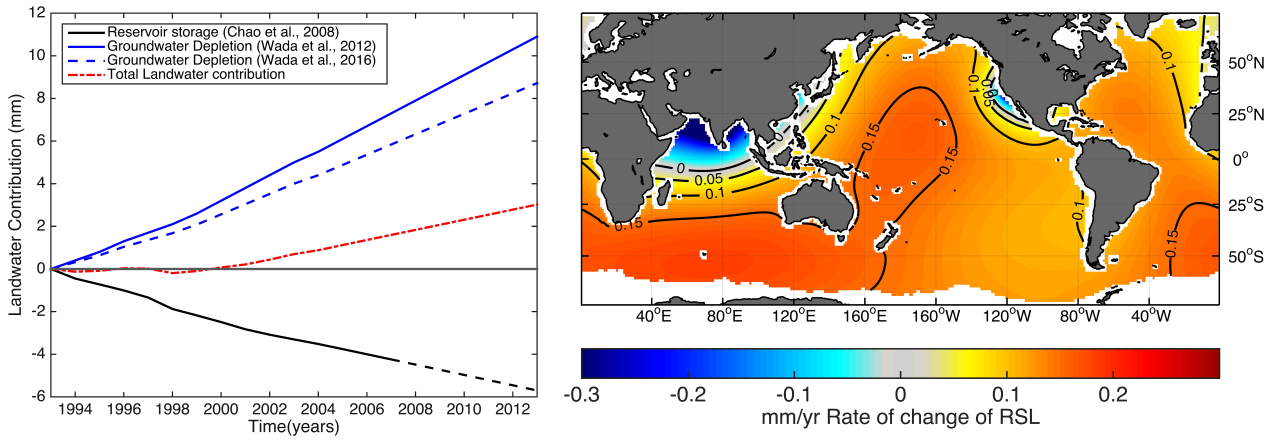

Figure 12. (a–left) Landwater contribution (mm) to relative sea-level change over the period 1993–2013. Black line represents water stored in reservoirs till 2007 and extrapolated to 2013 with the average rate of the period 2002–2007 (black dashed line) based on the data set by Chao *et al.* (2008). Solid blue line represents the groundwater depletion contribution to relative sea-level change over the same period based on the Wada *et al.* (2012) data set, while the blue dashed line is the improved estimate by Wada *et al.* (2016). Red dashed line represents the total landwater contribution over the period in question. (b–right) Landwater contribution (groundwater depletion and reservoir storage in mm/yr) to relative sea-level change over the period 1993–2013. Global weighted mean is 0.1±0.1 mm/yr, and contours represent values from 0.0–0.15 mm/yr. Missing values in white.

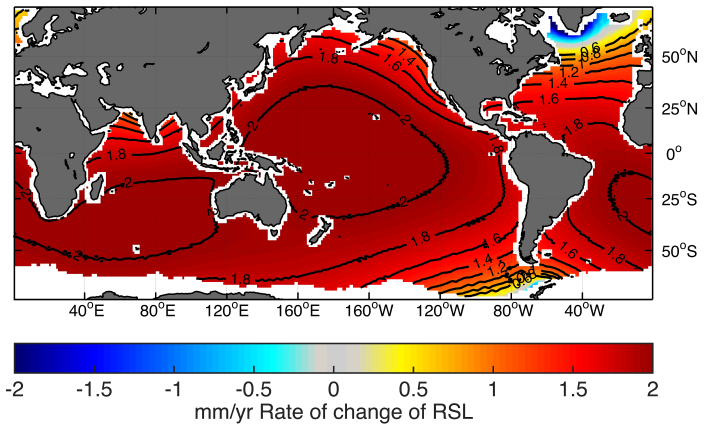

Figure 13. Relative sea-level fingerprint of the total modelled mass contribution (AIS & GrIS, MGIC, groundwater and reservoir storage) in mm/yr over the period 1993–2013. Missing values in white.

3.2.4 Thermosteric contribution

In Figure 14a, the change of thermosteric RSL rise w.r.t. 1993 is shown. Each gray line represents an individual CMIP5 AOGCM. The black line represents the thermosteric RSL change ensemble mean (all 16 models included), and the red shaded area is the multi-model $\pm 1\sigma$ spread. Local dynamic topography is not included in the time-series, as it is zero on a global mean. Over the period 1993–2013, the rate of RSL due to thermal expansion increased on average 1.4±0.4 mm/yr for the 0–700 m depth range including the deep ocean contribution (Figure 14b). The models representing the outliers of the thermosteric RSL rise

are MRI-CGCM3, at the lower-end with 0.7 mm/yr, and MPI-ESM-LR, at the higher-end with 1.8 mm/yr (Table 3, and Table 4 respectively).

GMSL rise due to thermal expansion is nearly equivalent to the increase in ocean heat content. CMIP5 historical simulations tend to underestimate the observed ocean heat uptake due to omission of volcanic forcing in their control experiments according to Gregory (2010) and Gregory *et al.* (2013). Following major volcanic eruptions, the rate of thermal expansion tends to temporarily increase, while the ocean rebounds from the cooling induced from volcanic forcing. Church *et al.* (2013) found that over the period 1993–2010, modelled thermosteric contributions exceedeed the observed contributions. However, given the uncertainties involved in the estimations, this difference is not statistically significant.

The resulting patterns thermosteric sea-level rise patterns (Figure 14b) can be explained by a combination of internal climate variability—eg. ENSO in the tropics, Atlantic Meridional Circulation (AMOC) in the Atlantic—and anthropogenic forcing—increase in GHGs concentration. However, anthropogenic forcing dominates the observed thermosteric sea-level, while the modelled thermosteric sea-level is mostly attributed to natural forcing (Slangen *et al.*, 2014a). Thermosteric RSL rise over the period 1993–2013 seems to be larger in the Indian Ocean (1.0–3.0 mm/yr), tropical Pacific (2.5–3.0 mm/yr), off the coast of Japan (2.0–3.0 mm/yr), Baffin Bay between Newfoundland, Canada and Greenland (2.5–3.0 mm/yr), and along the course of the Gulf Stream (>2.0 mm/yr). Similar patterns in some of these areas are also confirmed by Palanisamy *et al.* (2015b) in the tropical Pacific over the period 1993–2012, and Ishii and Kimoto (2009) in the tropical Pacific and North Atlantic (Baffin Bay/Greenland) over the period 1993–2009. On the other hand, Levitus *et al.* (2009) model thermal contraction off the coast Japan, a result which contradicts the modelled thermosteric trend in Figure 14b for the same region.

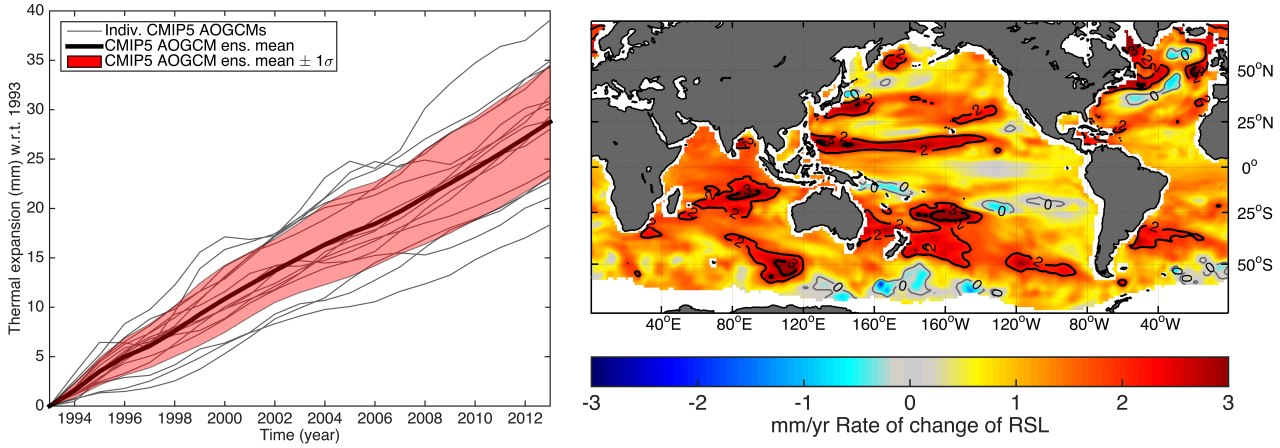

Figure 14. (a–left) Thermosteric-only contribution to relative sea-level change (mm) over the period 1993–2013. Grey lines indicate individual CMIP5 AOGCMs (16 in total), while the thick black line represents the ensemble mean of all 16 models, while the shaded red region represents the $\pm 1\sigma$ multi-model spread. Local dynamic topography is not included, as it is zero on a global mean. (b–right) Complete models ensemble mean of relative sea-level change (mm/yr) as a result of thermal expansion and local dynamic topography. Global weighted mean is 1.4 ± 0.4 mm/yr. Black lines indicate the 2 mm/yr (thin line) and 3 mm/yr (thick line) contour. Grey line indicates the 0 mm/yr contour. Missing values in white.

3.2.5 GIA contribution

The GIA contribution to RSL change during present times is zero. However, on a regional scale contribution from GIA is higher, mostly in areas formerly occupied by the Fennoscandian ice sheet and around the

periphery of Greenland (Figure 15), due to the slow rebound of the Earth's crust which in turn induces local relative sea-level rise. The underlying assumption here is that the GIA contribution remains constant over the period 1993–2013. On longer time scales (~1000 years), GIA would contribute to the RSL change, but not during the short period we study here.

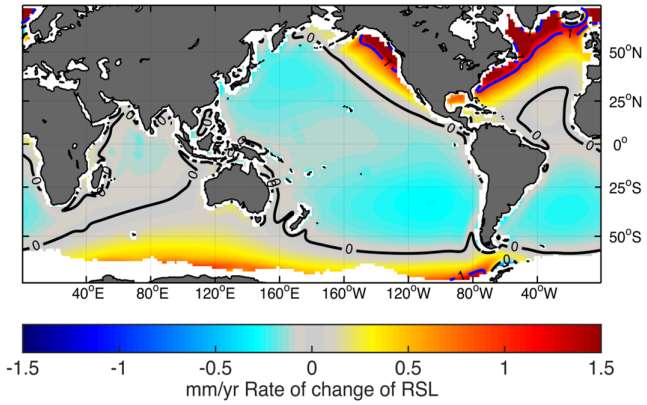

Figure 15. Map of GIA contribution to relative sea-level change in mm/yr at 0 kBP with data from Peltier's ICE-5G (VM2 L90) model version 1.2 (Peltier, 2004). Black line indicates zero contour, and blue line indicates where GIA contribution is equal to unity. Global weighted mean is 0.0 mm/yr over the period 1993–2013. Missing values in white.

3.3 Summation of modelled contributions (1993–2013)

3.3.1 "Complete" models

Table 3 summarizes our results of the GMSL budget for all models that contain all necessary fields to calculate RSL change (complete models) over the period 1993–2013. The ensemble mean sum of all individual contributions amounts to 3.0±0.4 mm/yr. The uncertainty quoted represents the multi-model $\pm 1\sigma$ spread. The model with the highest estimation is HadGEM2-ES with 3.4 mm/yr. Though relative conservative in its estimation of the thermosteric component, having the second lowest thermosteric estimate after MRI-CGCM3, HadGEM2-ES has the highest estimate regarding the MGIC contribution to RSL with 1.6 mm/yr, a model estimate 60% higher than the ensemble MGIC mean. The cryosphere (MGIC, AIS and GrIS) component of the HadGEM2-ES accounts for 68% of the total sum (3.4 mm/yr).

Among the complete models, the modelled RSL change was largest in the Pacific and Indian Ocean, and more specifically along the arch extending from Japan to the southeastern tip of Australia (Figure 16 and Figure 17). This pattern is more evident in some models than others such as CanESM2, HadGEM2-Es, MIROS-ESM-CHEM, MIROS-ESM, and NorESM1-M, while not as evident in CNRM-CM5, CSIRO-Mk3.6.0, and MRI-CGCM3, or at least to a lesser extent and magnitude. CSIRO-Mk3.6.0 even exhibits zero to negative RSL change off Philipinnes, a region where most of the other models agree that the rate of RSL change is high (>5.0 mm/yr) over the period 1993–2013.

In conclusion, the ensemble mean$\pm 1\sigma$ of the complete models [2.6–3.4 mm/yr] overlaps with the $\pm 1\sigma$ uncertainty of the observed GMSL [2.7–3.7 mm/yr] rise over the period 1993–2013, hence the complete models and observations are in good agreement.

Table 3. GMSL budget (mm/yr) for all complete models. The sum of contributions is made out of mountain glaciers and ice caps (MGIC), ice sheets (IS), thermal expansion and ocean dynamic changes contribution (TS), groundwater depletion (GW), reservoir storage (RS), and glacial isostatic adjustment (GIA).

Model	MGIC	IS	TS	GW	RS	GIA	Sum$\pm 1\sigma$
			mm/yr				
CanESM2	0.8		1.6				3.2
CNRM-CM5	0.8		1.0				2.6
CSIRO-Mk3.6.0	0.8		1.1				2.7
HadGEM2-ES	1.6	0.7	1.0	0.4	-0.3	~0.0	3.4
MIROS-ESM-CHEM	1.0		1.5				3.3
MIROC-ESM	1.0		1.5				3.3
MRI-CGCM3	0.9		0.7				2.4
NorESM1-M	0.9		1.5				3.2
Mean$\pm 1\sigma$	1.0$\pm$0.3	0.7$\pm$0.2	1.2$\pm$0.3	0.4$\pm$0.1	$-$0.3$\pm$0.1	~0.0	3.0$\pm$0.4

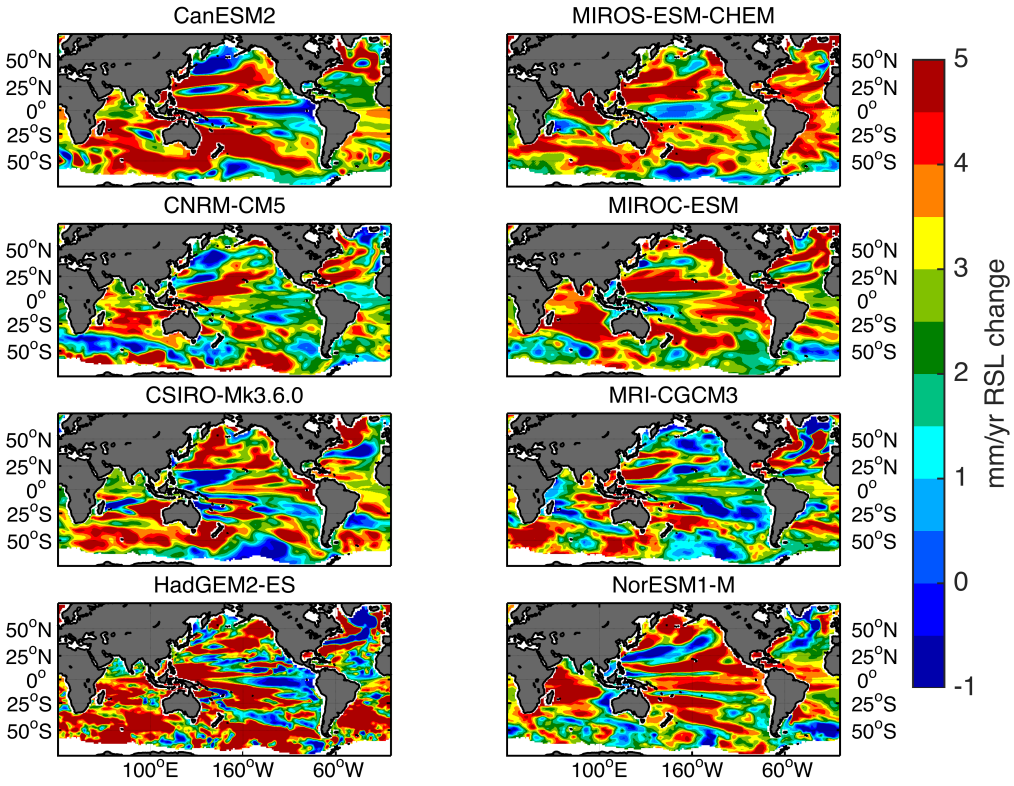

Figure 16. Relative sea-level change (mm/yr) for each of the complete models over the period 1993–2013. Missing values in white.

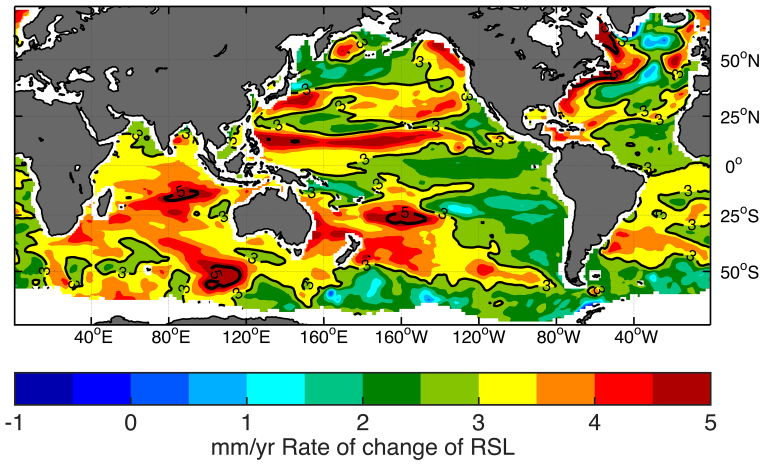

Figure 17. Complete models ensemble mean relative sea-level change (mm/yr) over the period 1993–2013. Thin black and solid black lines indicate the 3 mm/yr and 5 mm/yr contours respectively. Global weighted mean is 3.0±0.4 mm/yr. Missing values in white.

3.3.2 "Incomplete" models

Table 4 summarizes our results of the GMSL budget for all models that lack the local dynamic topography field (incomplete models) over the period 1993–2013 The ensemble mean sum of all individual contributions among the incomplete models amounts to 3.2±0.2 mm/yr. The incomplete models ensemble sum is 8% higher compared to the complete models ensemble sum. However, the incomplete models exhibit a 8.4% lower MGIC value than the complete models, and a 20% higher thermosteric contribution value compared to the complete models. However, any differences between the two sets of models (complete and incomplete) are purely based on chance and not the model quality per se. We chose the models based on availability of fields necessary to compute RSL patterns, hence these differences do not imply than one set is better than the other.

ACCESS1.0 and IPSL-CM5A-MR have the highest MGIC contribution among the incomplete models (1.0 mm/yr), and GFDL-ESM2G and MIROC5 model the lowest (0.7 mm/yr). In terms of thermosteric contribution, MPI-ESM-LR has the highest with 1.8 mm/yr, and INM-CM4 has the lowest with 1.2 mm/yr. MPI-ESM-LR and IPSL-CM5A-MR are the models with the highest sum (3.5 mm/yr), and along with HadGEM2-ES (3.4 mm/yr) from the complete models, are the models with the highest deviations from their respective ensemble mean, 9% (MPI-ESM-LR) and 13% (HadGEM2-ES) respectively.

We conclude that the ensemble mean$\pm 1\sigma$ of the incomplete models [3.0–3.4 mm/yr] overlaps with the $\pm 1\sigma$ uncertainty of the observations [2.7–3.7 mm/yr], and as such they are in good agreement with the observed GMSL rise over the period 1993–2013.

Table 4. GMSL budget (mm/yr) for all incomplete models. The sum of contributions is made out of mountain glaciers and ice caps (MGIC), ice sheets (IS), thermal expansion and ocean dynamic changes contribution (TS) whereby the ensemble mean *zos* field of the complete models has been used here, groundwater depletion (GW), reservoir storage (RS), and glacial isostatic adjustment (GIA).

Model	MGIC	IS	TS	GW	RS	GIA	Sum$\pm 1\sigma$
				mm/yr			
ACCESS1.0	1.0		1.3				3.1
GFDL-ESM2M	0.9		1.6				3.3
GFDL-ESM2G	0.7		1.5				3.0
INM-CM4	0.9	0.7	1.2	0.4	-0.3	~0.0	2.9
IPSL-CM5A-MR	1.0		1.7				3.5
MPI-ESM-LR	0.9		1.8				3.5
NorESM1-ME	0.9		1.5				3.2
MIROC5	0.7		1.7				3.2
Mean$\pm 1\sigma$	0.8$\pm$0.1	0.7$\pm$0.2	1.5$\pm$0.2	0.4$\pm$0.1	$-$0.3$\pm$0.1	~0.0	3.2$\pm$0.2

3.3.3 Ensemble mean of modelled RSL rise

Each individual source contributing to the modelled GMSL rise over the period 1993–2013 is summarised in Table 5. The largest modelled source is the land-ice contribution, composed of AIS and GrIS, and MGIC combined, which contributed 1.6$\pm$0.3 mm/yr of RSL change. Following the land-ice contribution, thermal expansion of the oceans (thermosteric) contributed 1.4$\pm$0.4 mm/yr over the same period, followed by the groundwater depletion which contributed 0.4$\pm$0.1 mm/yr. Finally, water impoundment behind reservoirs reduced the rate of GMSL rise by $-$0.3$\pm$0.1 mm/yr. GIA had zero contribution over the same period. In total, the modelled GMSL rise from all 16 models over the period 1993–2013 is 3.1$\pm$0.5 *mm/yr.*

Table 5. GMSL budget (mm/yr) for each individual contribution over the period 1993–2013. The modelled AIS and GrIS contributions are the values from Shepherd *et al.* (2012), linearly extrapolated to 2013. The modelled MGIC and themorsteric contributions are the ensemble mean of all 16 models used in this study computed with CMIP5 results, and the glacier model based on Slangen and Van de Wal (2011). The groundwater contribution only takes into account anthropogenic intervention, and does not include climate-related fluctuations of the water cycle; recharging of groundwater aquifiers is also taken into account. The *Reference* column lists the author(s) from which data sets were taken in order to calculate the GMSL trend of the middle column.

Source	mm/yr$\pm 1\sigma$	Reference
AIS	0.2$\pm$0.1	Shepherd *et al.* (2012)
GrIS	0.5$\pm$0.1	
MGIC	0.9$\pm$0.3	Slangen and Van de Wal (2011)
Thermosteric	1.4$\pm$0.4	CMIP5 output
Groundwater	0.4$\pm$0.1	Wada *et al.* (2016)
Reservoir Storage	$-$0.3$\pm$0.1	Chao *et al.* (2008)
GIA	~0.0	Peltier (2004)
Sum	3.1$\pm$0.5	This study
Observations (GIA applied)	3.2$\pm$0.5	Ablain *et al.* (2015)

3.3.4 Relative individual contributions to the complete models ensemble mean

In this section, we present the ratio (%) of each individual modelled contributions to RSL change over the period 1993–2013, against the complete models ensemble mean. The purpose is to examine the influence of each contribution on the total (complete models only) modelled RSL change and the spatial pattern they exhibit over the period 1993–2013. Maps of the individual contribution as a fraction of the complete models ensemble mean RSL change are shown in Figure 18. Table 6, summarizes the relative contributions of each modelled source.

Table 6. Relative contribution (%), based on relative sea-level change in mm/yr, of each contributing source over the period 1993–2013, to the complete models ensemble mean.

Source	Relative contribution (%)
MGIC	29%
AIS and GrIS	23%
Groundwater and reservoir storage	3%
Thermosteric	45%
GIA	0%

In total, land-ice explains 52% of the total modelled RSL change. The combined effect of MGIC, AIS, and GrIS influences positively the region NE of Japan (50–60%), the equatorial and eastern Pacific by the same amount, and the region SE of New Zealand and the Antarctic coast by 50–60%; on the other hand, the largest negative influence (-10%) is found around GrIS and the NAP as a result of gravitational disequilibrium, whereby RSL rises farthest away from the melt sources, and falls close to the source (Figure 4), i.e. ice sheets, as described by Equation 19 (Figure 18a).

Mountain glaciers and ice caps (MGIC) explain 29% of the total modelled RSL change. The 30% contour in Figure 18b shows which regions are more influenced on average from the melting of MGIC. Within the areas enclosed by the mean relative contribution contour, there exists places where the relative contribution is higher (30–50%) especially in central and eastern Pacific, off the coast of Antarctica, and east of Japan. These are the regions where MGIC have the highest influence. There is a region west of the North Antarctic Peninsula where MGIC have 0–10% influence. Another such region is found off the coast of Alaska with similarly low MGIC influence. All these locations have in common, is the presence of glaciers. Similarly, to the paragraph above, this is explained by gravitational disequilibrium. Other than the regions specified above, MGIC have a relative influence ranging from 10–30% on global RSL change over the period 1993–2013.

The AIS and GrIS combined, explain 23% of the total modelled RSL change. Around GrIS there is a dark blue region where the influence of ice sheets is negative (-10%); around the NAP a similar pattern is modelled, however the land-mask used covers part of it. In eastern Pacific, SE of New Zealand, and NE of Japan, we find that ice sheets influence the total modelled sea-level change by 30–40% over the period 1993–2013 (Figure 18c). The exhibited mass-related RSL patterns

The influence of groundwater depletion and reservoir storage on the total modelled RSL change is on average positive (3%). Around the coast of Antarctica, equatorial and easternPacific Ocean, NE of Japan, and along the course of the Gulf Stream and south of Greenland however the influence of groundwater seems to be higher (4–5%), while along the coast of India, Pakistan, and the SE tip of the Arabic Peninsula, areas where groundwater depletion is higher—due to higher rates of extraction—the influence of groundwater ranges from zero to -10 % (Figure 18d).

The effect of thermal expansion explains almost 45% of the total modelled RSL rise. The regions

bounded by the 40% contour in the Indian Ocean, the Pacific, and the Atlantic Ocean experience a 40–60% influence from thermal expansion. The regions where the thermosteric component of RSL rise is more influential are the high latitudes and especially the regions around GrIS and the NAP (50–60%) (Figure 18e). This can be attributed to increased freshwater input from precipitation and river runoff in the northern high latitudes, which leads to changes in the density structure of the region.

GIA has around zero or negative influence to modelled RSL rise. As indicated from the blue to dark blue regions which occupy the largest part of the global ocean basins, the influence of GIA is almost zero. However, regionally, in areas formerly occupied by ice sheets such as Arctic Canada (Fennoscandian ice sheet), around GrIS, NAP, and Scandinavia, the influence of GIA is >35%, and reaches 60%, for instance, around Greenland and Arctic Canada (Figure 18f).

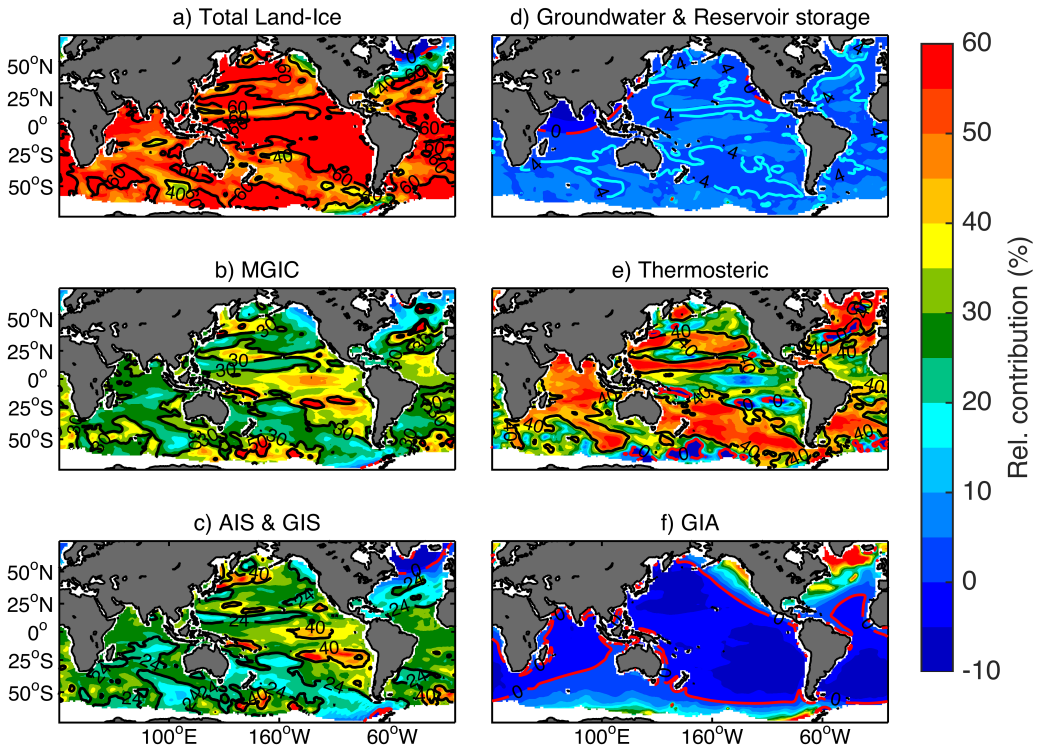

Figure 18. Panel with relative contribution (%) of each individual contribution against the complete models ensemble mean. a) Total land-ice contribution (AIS, GrIS, and MGIC), b) MGIC, c) AIS & GrIS, d) groundwater and reservoir storage, e) thermosteric, and f) GIA. Red contour represents 0% contribution. Missing values in white.

3.4 Global mean sea-level differences between observations and individual models

In this section, the relative difference (%) in GMSL change over the period 1993–2013 between observations and complete and incomplete models is shown. Both complete and incomplete models GMSL change agree well within the $\pm 1\sigma$ uncertainty with the observed GMSL change (Table 7 and Table 8), with respective relative differences of 6% and 0%. Finally, we take the average of the complete and incomplete models ensemble mean to compute the 16 CMIP5 multi-model ensemble, and find that the ensemble modelled GMSL is 3.1±0.5 mm/yr, which is in good agreement with the 3.2±0.5 mm/yr observed GMSL change from the SL_CCI data set. We conclude that: a) the RSL budget closes within the uncertainty, and b) that we understand well the processes that make up the observed GMSL change of 3.2±0.5 mm/yr.

Table 7. Comparison of observations against complete models in terms of GMSL over the period 1993–2013. Relative difference of GMSL change in %.

Model	Sum	Observations	Rel. diff.
	mm/yr		(%)
CanESM2	3.2	3.2±0.5	0%
CNRM-CM5	2.6		19%
CSIRO-Mk3.6.0	2.7		16%
HadGEM2-ES	3.4		-6%
MIROS-ESM-CHEM	3.3		-3%
MIROC-ESM	3.3		-3%
MRI-CGCM3	2.4		25%
NorESM1-M	3.2		0%
Mean±1σ	3.0±0.4	3.2±0.5	6%

Table 8. Comparison of observations against incomplete models in terms of GMSL over the period 1993–2013. Relative difference of GMSL change in %.

Model	Sum	Observations	Rel. diff.
	units: mm/yr		(%)
ACCESS1.0	3.1	3.2±0.5	3%
GFDL-ESM2M	3.3		-3%
GFDL-ESM2G	3.0		6%
INM-CM4	2.9		9%
IPSL-CM5A-MR	3.5		-9%
MPI-ESM-LR	3.5		-9%
NorESM1-ME	3.2		0%
MIROC5	3.2		0%
Mean±1σ	3.2±0.2	3.2±0.5	0%

3.5 Regional sea-level differences between observations and complete models

To perform the regional comparison, we used only complete models, as they contain all necessary fields to calculate RSL patterns. We looked at spatial patterns of relative differences (%) based on RSL trends (mm/yr) in 8 regions (Table 9) of high interest over the period 1993–2013—regional boundaries were chosen arbitrarily though carefully selected to cover most of the globe (Figure 20–Figure 27). The relative differences are given by Equation 23:

$$Relative\ difference\,(\%) = \frac{O_i - M_i}{O_i} \times 100 \tag{23}$$

where O_i and M_i represent observed and modelled RSL change (mm/yr) respectively, in n number of grid points. Additionally, differences between the observations and complete models are assessed through the root-mean-square error (RMS error; mm/yr) (Figure 28) given by Equation 24:

$$RMS\ error\,(mm/yr) = \sqrt{\frac{1}{n}\sum_{i=1}^{n}(O_i - M_i)^2} \tag{24}$$

The relative RMS error (rRMS error) is given in Equation 25, whereby the RMS error has been scaled with the observed regional mean, $\bar{O}_{reg.}$:

$$rRMS\ error\,(\%) = \frac{\sqrt{\frac{1}{n}\sum_{i=1}^{n}(O_i - M_i)^2}}{\bar{O}_{reg.}} \times 100 \tag{25}$$

The rRMS error indicates if the errors are larger or smaller than the observed regional average per region; the smaller the rRMS error is, the better the match between observations and modelled RSL change is.

The ensemble mean of the complete models is tested against observations in Figure 19. The ensemble mean performs relatively well in SE Asia (r1), with relative differences ranging from 25–50%. Despite underestimating the observations by ~60% on average, intramodel agreement exists that SE Asia exhibited high regional sea-level rise over the period 1993–2013. Models also capture relatively well the strong dipole-like pattern with the two relative maxima near 10^oN and 10^oS of the equator, but underestimate the magnitude of the rise. The RMS error between observations and ensemble mean is 3.5 mm/yr or 59% of the observed regional mean (Figure 28, Figure 29). CanESM2 and HadGEM2-ES agree fairly well with observations with RMS error of 3.2 mm/yr or 54% of rRMS error (Figure 28, Figure 29). CanESM2 seems to model the northern branch of the dipole-pattern near 10^oN better than the one near 10^oS, in which case its magnitude is underestimated by almost 75–100% (Figure 20). We previously saw (Figure 16) that CSIRO-Mk3.6.0 highly underestimates the observed rise (Figure 6) in SE Asia. This is also evident from Figure 20, where the magnitude of the regional sea-level change is underestimated by 100–120%. The CSIRO-Mk3.6.0 RMS error in the region is 5.9 mm/yr, as high as the observed regional mean (5.9 mm/yr), and 83% higher than the global observed mean (3.2 ± 0.5 mm/yr).

Eastern equatorial Pacific is the region where models perform the least well (Figure 19), overstimating the observations by ~285% (ensemble mean) on average. This is not apparent from Figure 28 (RMS error of 2.0–4.2 mm/yr), however when scaled with the regional observed RSL mean (0.8 mm/yr), models differ as much as ~530%, for instance, NorESM1-M. All models exhibit rRMS error values >250%. Though the observed trend in the region is ranging from ~$\pm$1.0 mm/yr (Figure 6), the modelled RSL trend reach as high as 4.0–5.0 mm/yr (NorESM1-M) in this region (Figure 16). The models fail to capture the observed RSL patterns and estimate the observed magnitude. CanESM2 is the only model that captures this V-shaped pattern, most likely associated with ENSO variability, that extends from western coast of South America to central Pacific.

Southern Ocean exhibits high variability in terms of observed RSL patterns (Figure 6), most likely associated with Antarctic Circumpolar Current (ACC) jets or frontal filaments. Over the period 1993–2013, the Southern Ocean exhibits positive RSL trends (regional observed mean of 2.8 mm/yr), similar to the global observed mean. The observed spatial patterns in the Southern Ocean are captured relatively well by models (Figure 22). In the western part, all models overestimate by 150–200% the observations, while in the easternpart close to Drake Passage, all models underestimate by 75–200%, the observed RSL patterns. Overall, all models exhibit RMS errors ranging from 2.3–4.0 mm/yr, which is 82–142% of the observed regional mean with the ensemble mean being 2.4 mm/yr or 85% of the observed mean. CSIRO-Mk3.6.0 represents the observations with the lowerst rRMS error 82% in this region, and HadGEM2-ES doing the least well with rRMS error of 142%.

The observed RSL patterns in North Pacific exhibit high variability most likely associated with jets and eddies related to the Kuroshio Current. Over the period 1993–2013, North Pacific experienced RSL trends (3.3 mm/yr) as high or slightly higher than the global observed mean. RMS error ranges from 3.2–4.0 mm/yr (98–122%) with the ensemble mean being 3.1 mm/yr (93%). The regional ensemble mean spatial patterns (Figure 19), show models underestimating the observations in terms of relative differences by 25–50%. CSIRO-Mk3.6.0 does a better job in this case with rRMS error of 98%, while

CanESM2, CNRM-CM5, and NorESM1-M doing the least well with rRMS error of 122%, 121%, and 123% respectively (Figure 29).

The ensemble mean performs better than any of the individual models in Greenland with RMS error of 1.9 mm/yr and rRMS error of 55%. Among the individual models CNRM-CM5 is performing the best with RMS error 2.6 mm/yr and rRMS error 77%. Though from the spatial distribution of relative differences it might seem as CNRM-CM5 is underestimating a large portion around and south of Iceland (100–200%), in reality it seems it performs marginally better than CSIRO-Mk3.6.0, which is overestimating for the most extent the spatial patterns by 50–120%.

In terms of relative differences, the models ensemble mean overestimate (50–200%) for the most part the region east of the Florida Peninsula, and off the coast of Atlantic Canada in the Equatorial Atlantic Ocean (r6). Farther east, in central Atlantic models seem to underestimate the observations by >150%. In the eastern Atlantic Ocean basin closer to Europe, the models are in good agreement ($\pm$10%), for the most part, while farther south off the coast of Africa, they slightly (~50%) underestimate the observations. Models exhibit RMS error ranging from 2.3–3.5 mm/yr, and rRMS error of 89–132%. The ensemble mean performs better than any individual model with rRMS error of 87%, very close to NorESM1-M which has rRMS error of 89%. HadGEM2-ES and MRI-CGCM3 have the highest rRMS error with 132% and 126% respectively.

Both Indian and South Atlantic Ocean are the two regions were models perform the best against observations among all 8 regions selected. CSIRO-Mk3.6.0, MIROS-ESM-CHEM, and MRI-CGCM3 underestimate the region off the coast of Madagascar by 50–100%, while NorESM1-M overstimates the same region by the same magnitude or more (150–200%). RMS error range from 1.4 mm/yr (CNRM-CM5) to 2.9 mm/yr (NorESM1-M), while the ensemble mean has the lowest with 1.3 mm/yr. rRMS error are ranging respectively from 40–88%, with an ensemble mean rRMS error of 38%. In the South Atlantic Ocean, agreement is even better with relative differences ranging from $\pm$50%, and reaching around 100% in off the coast of South America in CSIRO-Mk3.6.0. Overall, RMS error is ranging from 1.0 mm/yr (NorESM1-M) to 2.3 mm/yr (HadGEM2-ES), with the ensemble mean RMS error being 1.1 mm/yr. In terms of rRMS error, NorESM1-M exhibits the best regional match among all regions and across all models with 32%, which is considered a very good match.

On a global scale, all models exhibit rRMS error ranging from 82–104%, with the ensemble mean being 73%. The model ensemble mean performed the least well in eastern equatorial Pacific with rRMS error of 291%, and performed the best in the South Atlantic with rRMS error of 34%, which is considered a good match. In a number of cases (North Pacific, Greenland, Indian Ocean, Global), we find that the ensemble mean performs better than any individual models; for instance, in Greenland the ensemble mean (55%) is 38% lower than the lowest rRMS error among individual models i.e. CNRM-CM5 (76%). We conclude that the models do not perform well regionally and the majority of models exhibit rRMS errors larger than 50% of the respective observed regional means with the exception of the Indian Ocean (ensemble mean rRMS error of 39%) and the South Atlantic Ocean (ensemble mean rRMS error of 34%).

Table 9. Region number, name, and corresponding coordinates to Figure 20–Figure 27.

Region #	Region name	Coordinates
r1	SE Asia	$99.5^oW - 189.5^oW$, $-20.5^oN - 20.5^oS$
r2	Eastern equatorial Pacific Ocean	$200.5^oW - 275.5^oW$, $20.5^oN - 20.5^oS$
r3	Southern Ocean	$0.5^oW - 359.5^oW$, $68.5^oS - 40.5^oS$
r4	North Pacific	$124.5^oW - 199.5^oW$, $19.5^oN - 60.5^oN$
r5	Greenland	$299.5^oW - 359.5^oW$, $50.5^oN - 70.5^oN$
r6	Equatorial Atlantic Ocean	$274.5^oW - 359.5^oW$, $20.5^oN - 49.5^oN$
r7	Indian Ocean	$24.5^oW - 98.5^oW$, $30.5^oN - 30.5^oS$
r8	South Atlantic Ocean	$300.5^oW - 359.5^oW$, $10.5^oN - 35.5^oS$
r9	Global	$0.5^oW - 359.5^oW$, $68.5^oN - 68.5^oS$

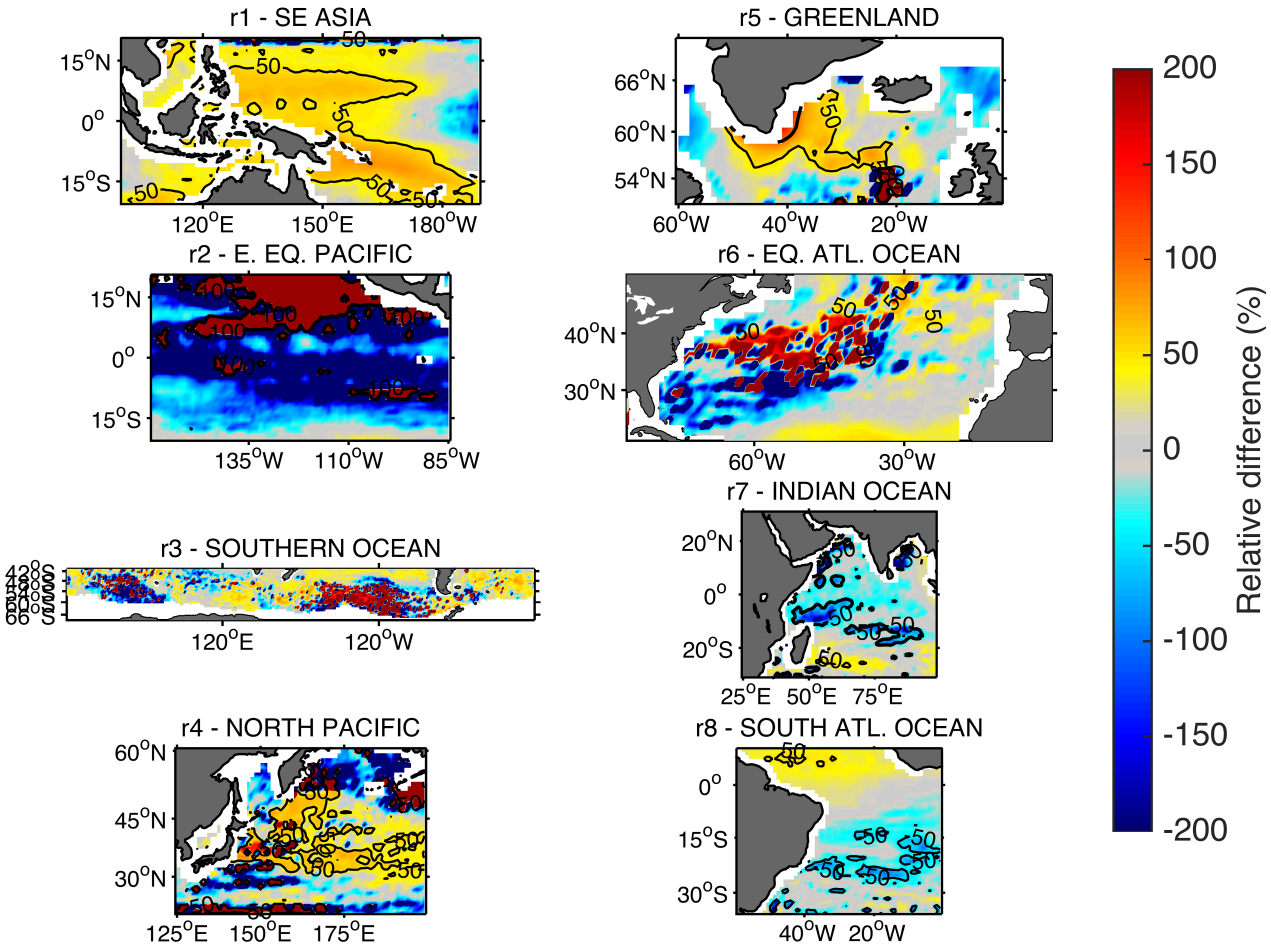

Figure 19. Relative difference (%) based on RSL trend between regional observations and the complete models ensemble mean per region under investigation. Thin black line indicates the 50% contour and thick black line the 100% contour. Missing values in white.

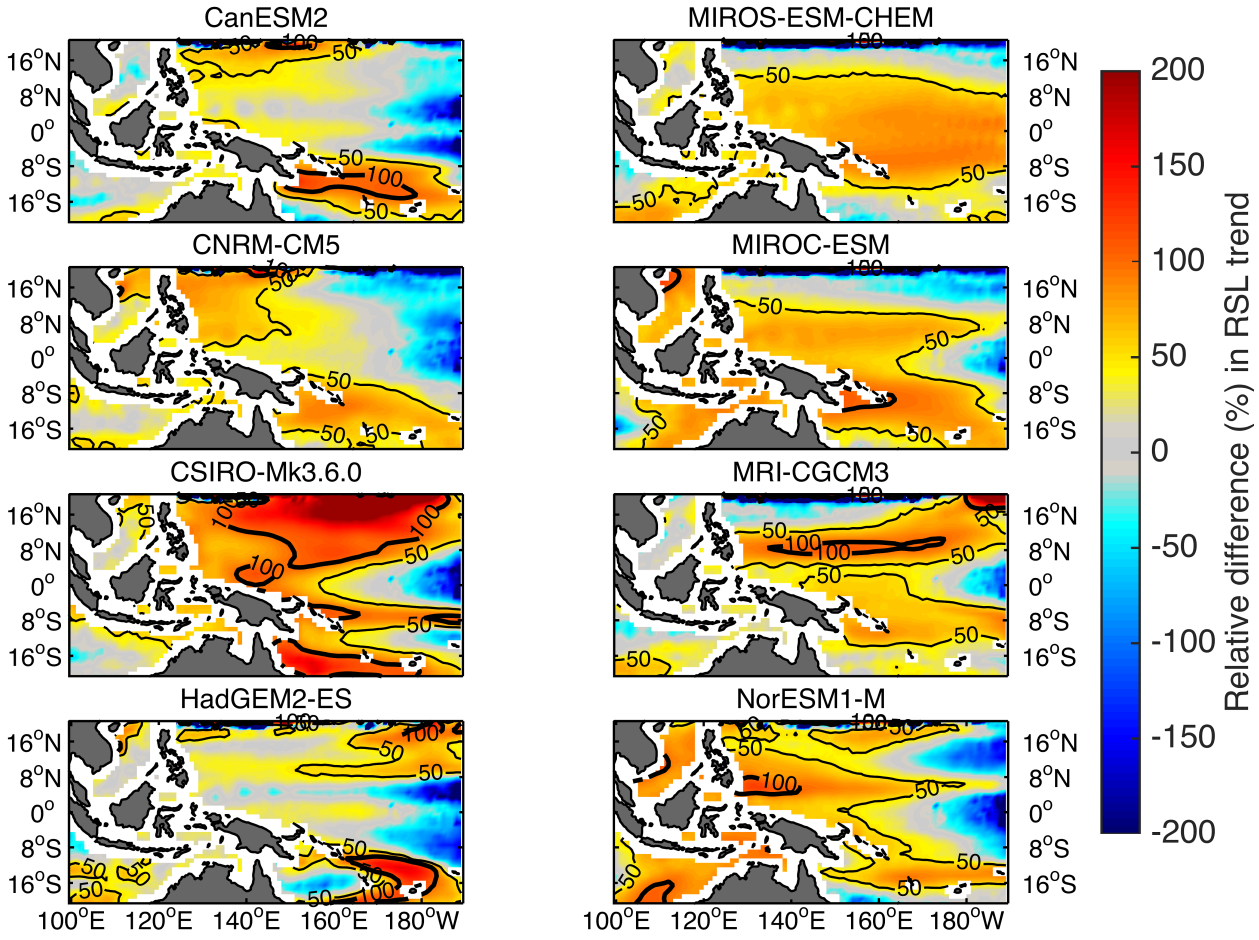

Figure 20. Relative difference (%) based on RSL trend between regional observations and complete models in SE Asia (r1). The 50% and 100% contour are indicated by the thin and thick black lines respectively. Regional observed mean is 5.9 mm/yr. Missing values in white.

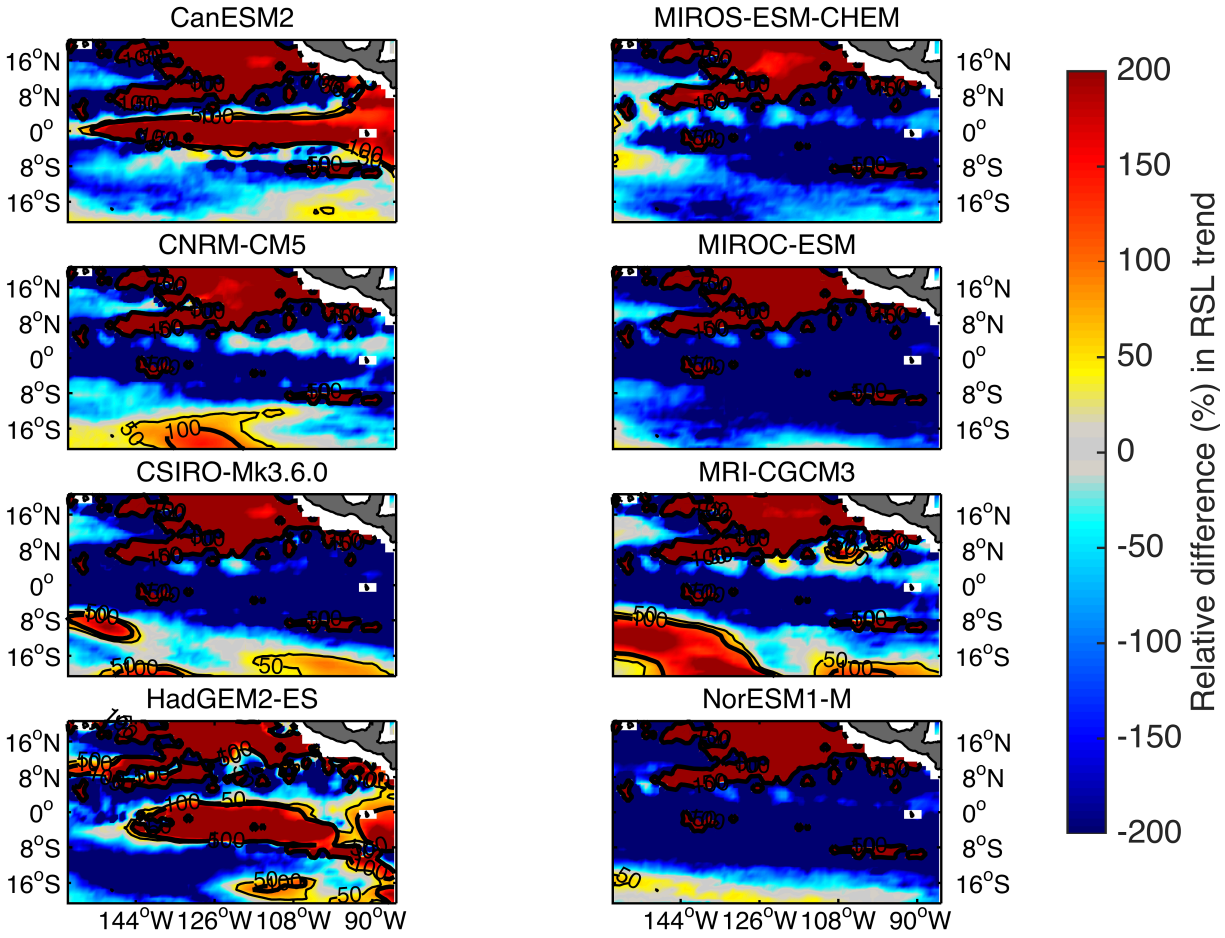

Figure 21. Relative difference (%) based on RSL trend between regional observations and complete models in eastern equatorial Pacific Ocean (r2). The 50% and 100% contour are indicated by the thin and thick black lines respectively. Regional observed mean is 0.8 mm/yr. Missing values in white.

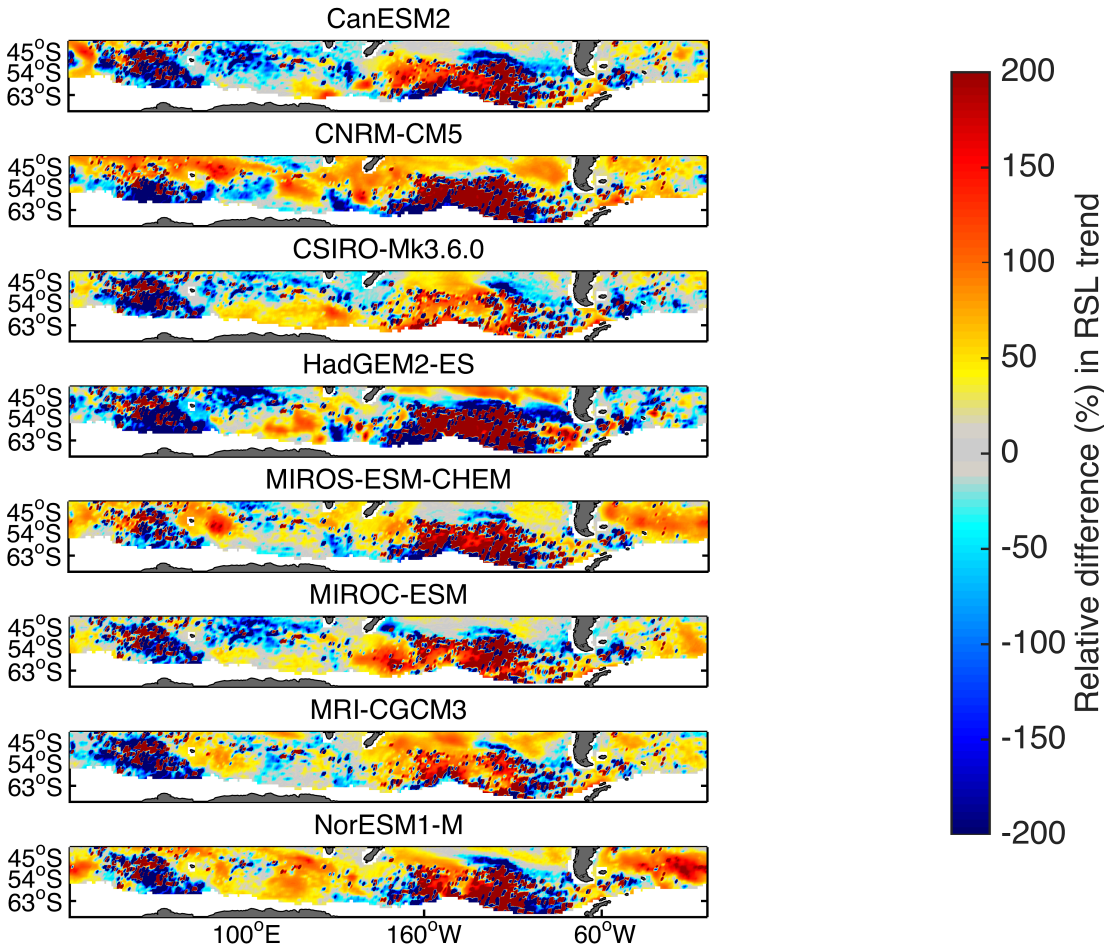

Figure 22. Relative difference (%) based on RSL trend between regional observations and complete models in the Southern Ocean (r3). Regional observed mean is 2.8 mm/yr. Missing values in white.

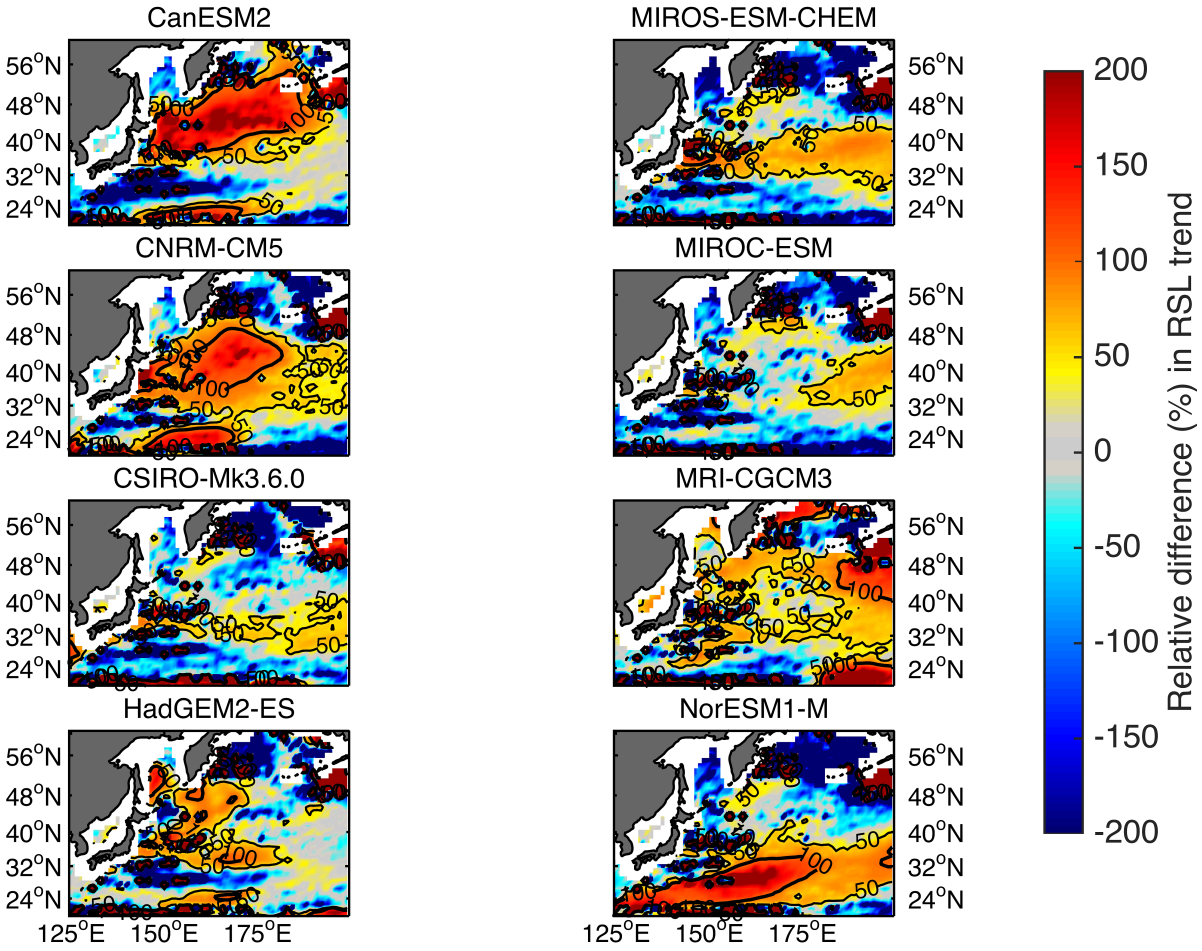

Figure 23. Relative difference (%) based on RSL trend between regional observations and complete models in the North Pacific Ocean (r4). The 50% and 100% contour are indicated by the thin and thick black lines respectively. Regional observed mean is 3.3 mm/yr. Missing values in white.

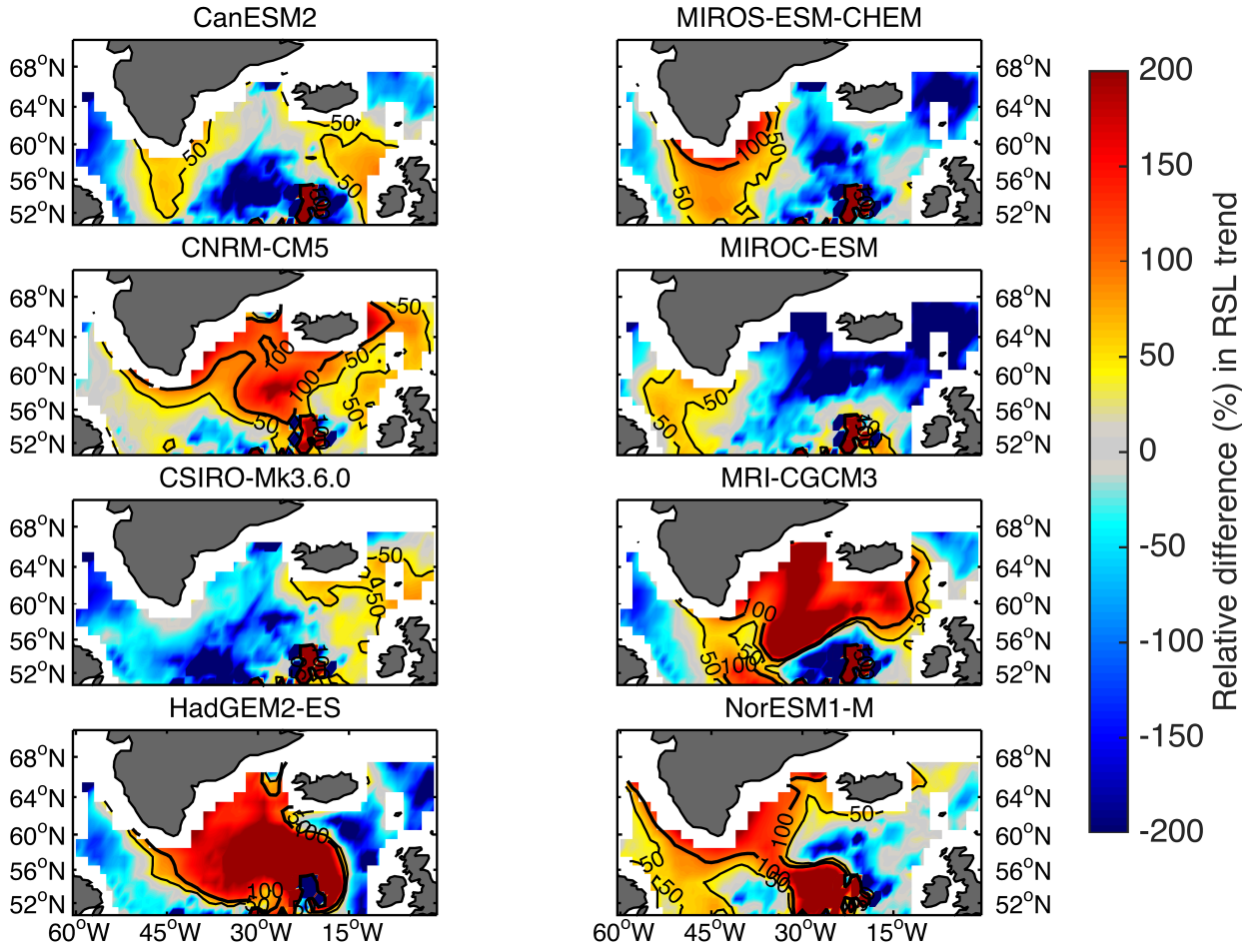

Figure 24. Relative difference (%) based on RSL trend between regional observations and complete models in Greenland (r5). The 50% and 100% contour are indicated by the thin and thick black lines respectively. Regional observed mean is 3.4 mm/yr. Missing values in white.

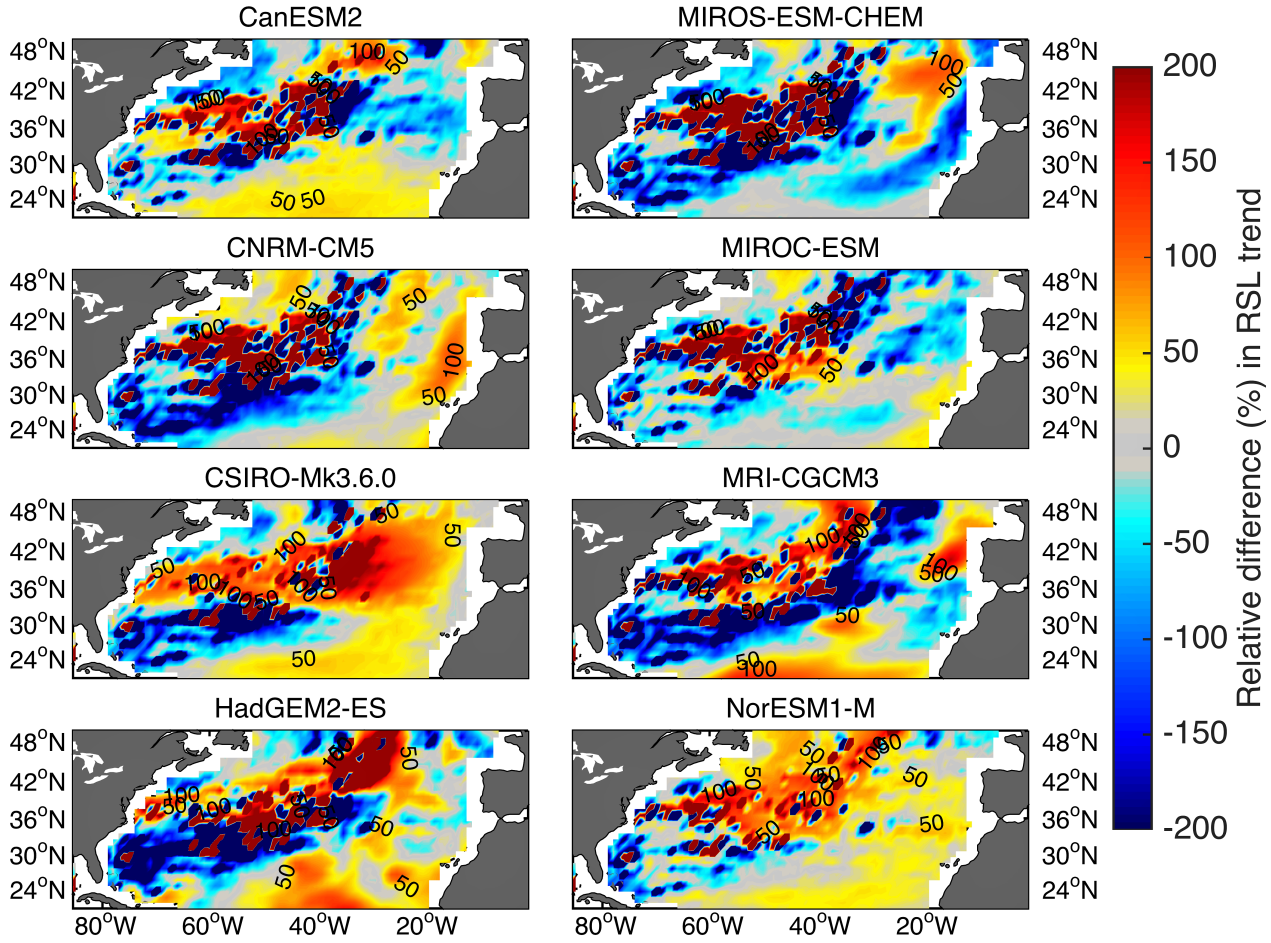

Figure 25. Relative difference (%) based on RSL trend between regional observations and complete models in the equatorial Atlantic Ocean (r6). The 50% and 100% contour are indicated by the thin and thick black lines respectively. Regional observed mean is 2.6 mm/yr. Missing values in white.

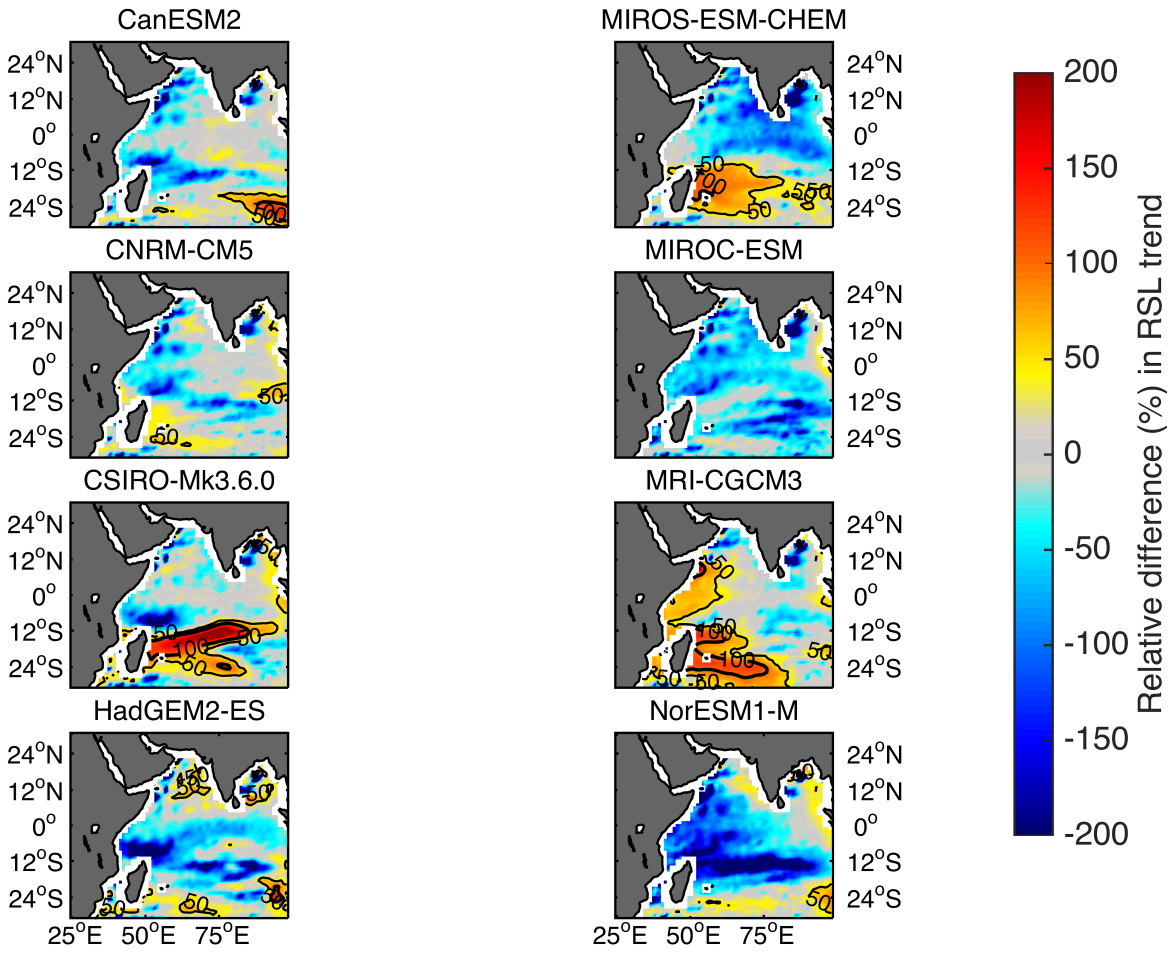

Figure 26. Relative difference (%) based on RSL trend between regional observations and complete models in the Indian Ocean (r7). The 50% and 100% contour are indicated by the thin and thick black lines respectively. Regional observed mean is 3.4 mm/yr. Missing values in white.

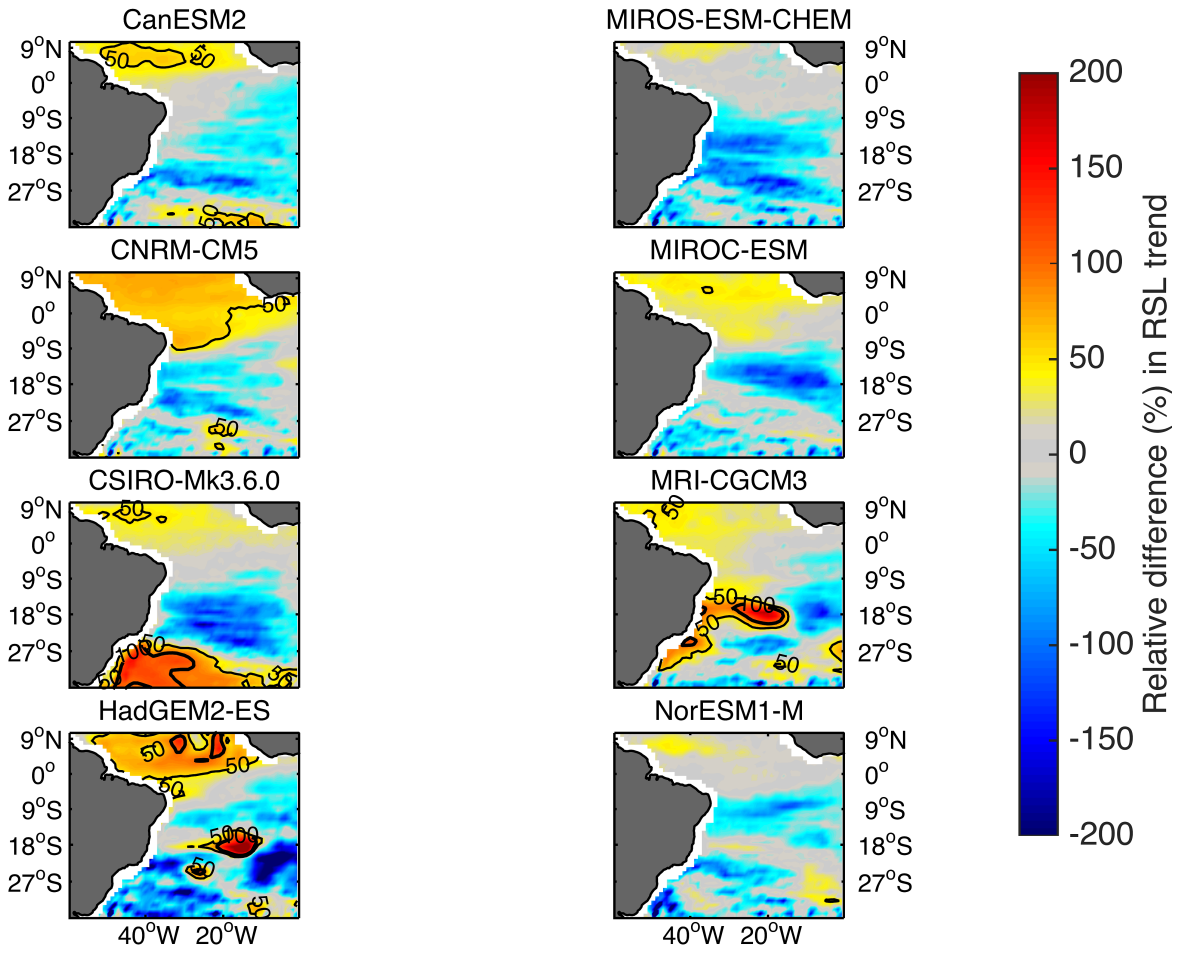

Figure 27. Relative difference (%) based on RSL trend between regional observations and complete models in the South Atlantic Ocean (r8). The 50% and 100% contour are indicated by the thin and thick black lines respectively. Regional observed mean is 3.2 mm/yr. Missing values in white.

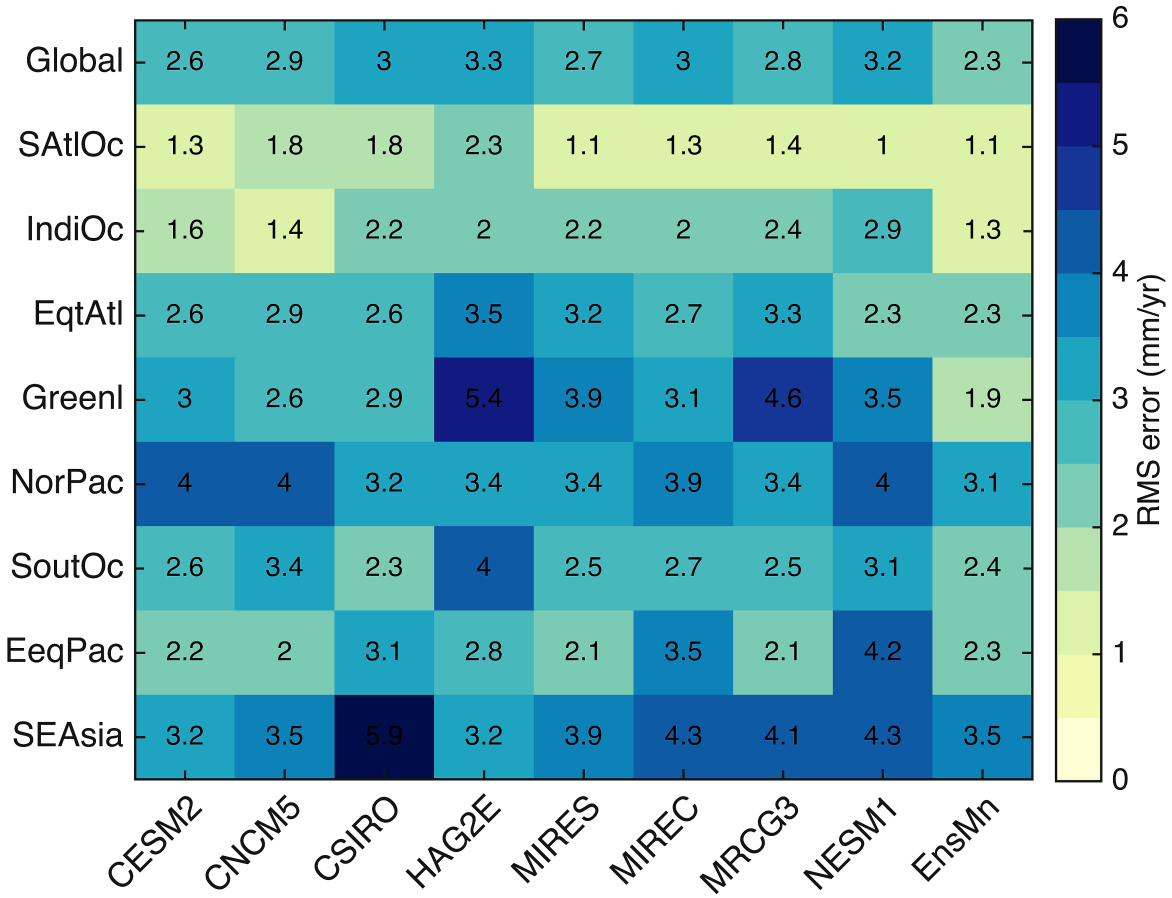

Figure 28. Root-mean-square error heatmap based on RSL trend (mm/yr) of regional observations against complete models per region and globally. Individual models are presented with their 5-character code name as follows: CanESM2 (CESM2), CNRM-CM5 (CNCM5), CSIRO-Mk3.6.0 (CSIRO), HadGEM2-ES (HAG2E), MIROS-ESM-CHEM (MIREC), MIROS-ESM (MIRES), MRI-CGCM3 (MRCG3), and NorESM1-M (NESM1).

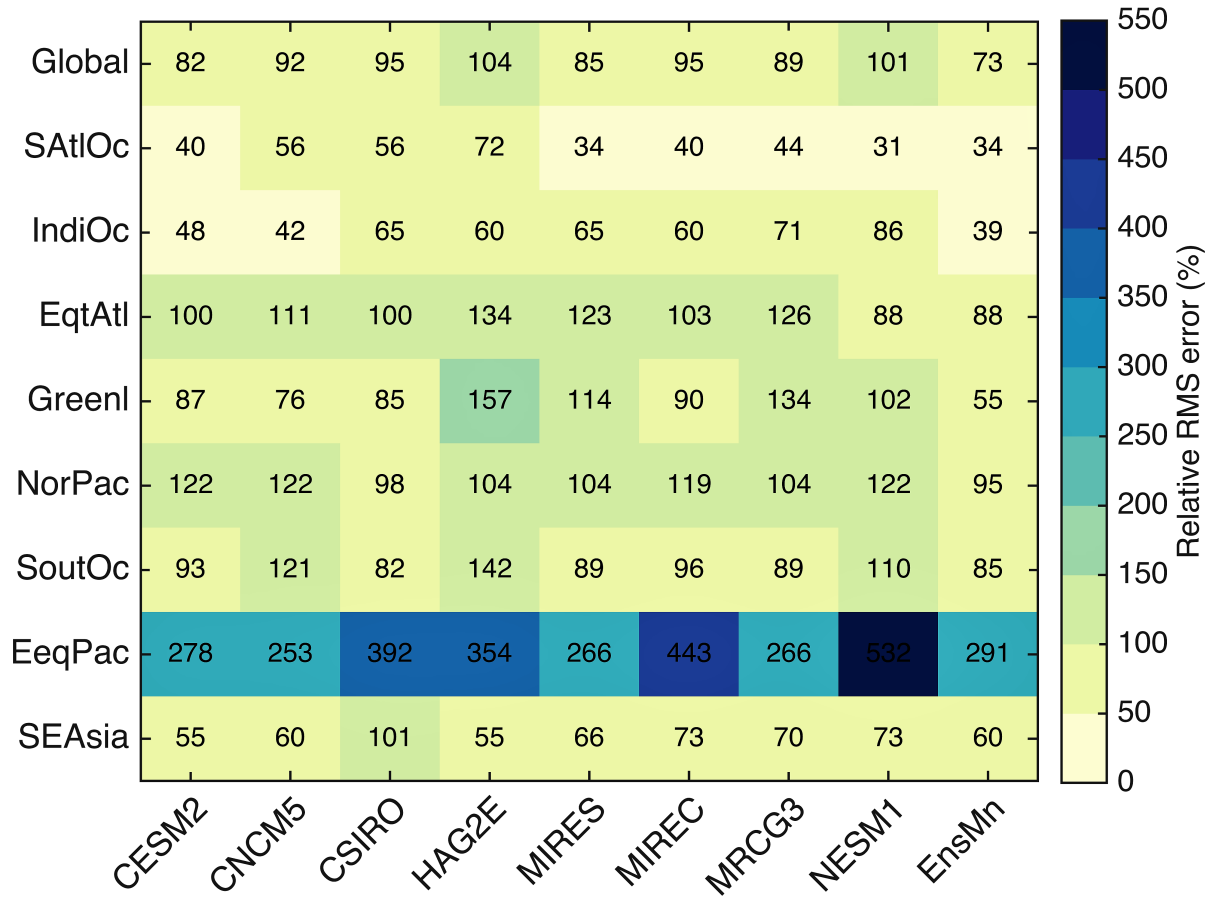

Figure 29. Relative root-mean-square error (%) heatmap based on RSL trend of regional observations against complete models, per region and globally, scaled with the observed regional mean. Short model names sames as in caption of Figure 28.

4 Discussion

In this study, we compared observed RSL changes over the period 1993–2013 from SL_CCI data against modelled RSL changes calculated from the output of 16 CMIP5 models and independent data sets, and we concluded that the modelled RSL rise achieves closure of the RSL budget, within the uncertainty, against the SL_CCI observations. We will now place the results we acquired in a broader context, and draw comparisons against similar studies conducted, such as the paper from Chambers *et al.* (2016) (henceforth C16), where they evaluate the GMSL budget over the period 1993–2014. Similarly to this study, C16 utilised data from SL_CCI over the period 1993–2014. Moreover, our regional study will be compared with other studies conducted, and the role of natural variability versus anthropogenic forcing will also be discussed.

4.1 Global mean sea-level budget comparison

The observed GMSL trend is 3.2±0.5 mm/yr based on SL_CCI data set over the period 1993–2013. This result agrees well with other research groups, which investigated the GMSL trend over the same period with satellite altimetry observations, such as the Colorado University (CU) Sea Level Research Group (3.4±0.4 mm/yr), AVISO (3.4±0.6 mm/yr), CSIRO (3.3±0.4 mm/yr), NASA GSFC (3.4±0.4 mm/yr), and NOAA (3.2±0.4 mm/yr) (available at: http://sealevel.colorado.edu/, accessed October 30th, 2016).

Over the period 1993–2013, the modelled RSL rise trend is 3.1±0.5 mm/yr, of which ~45% can be explained by volume changes, i.e. thermal expansion of the ocean (thermosteric), and the rest ~55% can be explained by mass contribution (land-ice, and groundwater and reservoir storage). This result agrees well with C16 where they conclude that 60% of the increase in RSL rise over the period 1993–2014 is explained by mass contribution, and 40% by thermal expansion of the oceans. Out of this 55% mass contribution, we found that MGIC contributed ~29%, AIS and GrIS contributed 23%, and groundwater and reservoir storage contributed 3%. C16 found that MGIC had the largest effect ~25%, terrestrial water storage—groundwater depletion, water impoundments behind dams, storage loss of endorheic lakes and wetlands, deforestation, and changes in soil moisture, permafrost and snow—had the next (~15%), and finally, Greenland and Antarctica contributed ~12% and ~7% respectively. Our results differ by 14% compared to C16 regarding MGIC contribution, and by 20% regarding the GrIS contribution, while they agree well regarding the AIS contribution. C16 terrestrial water storage contribution is 5-times higher than ours, possibly due to the inclusion of additional processes as mentioned above. This 0.4 mm/yr higher estimate from the terrestrial contribution in C16 budget is compensated in our budget by 0.1 mm/yr higher contribution from GrIS and MGIC, and by a 0.2 mm/yr higher thermosteric contribution. All differences associated with the modelled GMSL between this study and C16 are considered non-significant and overlap with the $\pm 1\sigma$ uncertainty. Overall our results agree well with C16 (Table 10).

Table 10. GMSL budget (mm/yr) over the period 1993–2013 for modelled-based contributions from this study, compared against Chambers *et al.* (2016) results. In this study, terrestrial water storage includes only groundwater depletion and reservoir storage, while in Chambers *et al.* (2016) it also includes storage loss from endorheic lakes and wetlands, deforestation, and changes in soil moisture, permafrost, and snow. Thermosteric contribution accounts for changes from the surface and up to 2000 m depth. GIA is not included as it has zero contribution over the period of study. Uncertainty quoted as $\pm 1\sigma$.

Sources	**1993–2013 (this study)**	**1993–2014 (Chambers et al., 2016)**
Modelled GMSL	mm/yr	
AIS	0.2±0.1	0.2±0.1
GrIS	0.5±0.1	0.4±0.3
MGIC	0.9±0.2	0.8±0.3
Terrestrial	0.1±0.1	0.5±0.2
Thermosteric	1.4±0.4	1.2±0.3
Total	3.1±0.5	3.1±0.6
Observed GMSL	3.2±0.5	3.2±0.7

4.2 Natural variability versus anthropogenic forcing

To what extent does anthropogenic forcing plays a role in the relative sea-level patterns observed? Is it solely anthropogenic forcing that drives these changes or just natural variability associated with ENSO and IPO/DPO events? The answers to these questions have been investigated by several authors and the conclusion is simple. Statitistical techniques have demonstrated that natural variability exclusively cannot explain the observed GMSL trend during the past century and the satellite altimetry era (Becker *et al.*, 2014; Dangendorf *et al.*, 2015; Marcos *et al.*, 2016; Slangen *et al.,* 2016). On the other hand, Slangen *et al.* (2016) demonstrated, while investigating the effect of rising GHGs concentrations to global RSL rise, that GHGs became the dominant contribution to RSL rise after 1970 (69±31%), and reaching 72±39% by the 2000s. In this study, we showed that human activities have a direct impact on RSL changes. We showed that over the period 1993–2013, human extracted groundwater used for agriculture, farming or personal consumption for instance, contributed in total 8.6 mm or 0.4±0.1 mm/yr of RSL change. Moreover, the accelerating construction of reservoirs (dams) stored 6.3 mm or 0.3±0.1 mm/yr of potential RSL change on land. In Figure 12, we saw that the rate of RSL changes slower near regions of groundwater loss—Indian, Arabian Sea, NE China, and California—over the period 1993–2013, mainly of because: a) deflections of the solid Earth and sea surface as a result of mass movement from the continents to the oceans; this spherical harmonc degree 1 movement of water mass represents a change to the vector between Earth's center of mass and figure, which shifts the solid Earth and elevates RSL rise in the Pacific while it leads to RSL fall in southern Asia, and b) as rocks uplift due to elastic expansion when unloaded, the mass loss depresses the geoid locally, causing the sea surface to fall (Veit and Conrad, 2016).

Groundwater depletion and reservoir storage contributed around ~15% of the modelled RSL rise over the satellite era (Chambers *et al.,* 2016). Thermosteric (45%), melting of glaciers (29%), and losses from AIS and GrIS (23%) were far greater contributors. Marcos and Amores (2014) found that 87% of the observed thermosteric RSL trend in the upper 0–700 m since 1970 is induced by human activity, confirmed by Slangen *et al.* (2014a) that also concluded that anthropogenic forcing, caused by increasing GHGs concentrations, had a large impact on full-depth thermosteric RSL rise in the 20th century. Global glacier mass loss has also been with high confidence attributed to anthropogenic forcing between 1991–2010 and the anthropogenic fraction to these losses has increased to 69±24% compared to 25±35% over the period 1851–2010 (Marzeion *et al.*, 2014). On the other hand, the retreat of the West Antarctic ice sheet (WAIS) is

primarily attributed to the retreat of the grounding line in response to the end of the last ice age (Huybrechts *et al.*, 2004), and since ice sheets only respond very slowly to climate changes (decades to thousands of years), past forcing may still be influential in ongoing observed changes (Hegerl *et al.*, 2007). However, Antarctic glaciers like the Pine Island Glacier, has shrinked at an increasing rate, and over the past 40 years it is the largest contributor to sea-level rise in Antarctica (Shepherd *et al.*, 2012; Favier *et al.*, 2014). This fast retreat has been ascribed to increased sub-ice-shelf melting caused by the recent modification of the CDW circulation (Faver *et al.*, 2014).

4.3 Regional patterns

In Figure 6, we saw that the Pacific Ocean has been the region with the largest observed RSL trends over the altimetry era. Marcos *et al.* (2016) identified two noticeable patterns: "a) a V-shaped broad-scale positive trend pattern extending from about 30°–50°N in the central basin to the western equatorial Pacific and then 30°–50°S in the central-eastern basin, and b) a well-pronounced strong dipole-like pattern with positive trends in the western tropical Pacific (with two relative maxima near 10°N and 10°S) and negative trends in the central-eastern tropical Pacific (with relative minima trapped in the equatorial band) limited to about 30°N and 20°S" (Marcos *et al.*, 2016). A number of studies has linked the aforementioned two spatial patterns in the Pacific with climate variability events: a) the V-shaped broad-scale positive pattern has been linked with decadal IPO/DPO climate variability (England *et al.*, 2014; Hamlington *et al.*, 2014; Marcos *et al.*, 2016), while b) the strong dipole-like pattern has been of thermosteric (0–700 m) origin due to surface wind stress-driven vertical thermocline movement, which is related to the ENSO internal climate variability (Merrifield and Maltrud, 2011; Merrifield *et al.*, 2012; McGregor *et al.*, 2012; Becker *et al.*, 2012; Nidheesh *et al.*, 2013). In Figure 7b, we also found that ENSO events leave a trace in the observed RSL rise signal. A comparison by the CU Sea Level Research Group between GMSL change from altimetry observations after the mean, linear trend, and seasonal signal was removed against the Multivariate ENSO Index (MEI) concluded that there exists a strong correlation between the GMSL and MEI, with the GMSL often lagging changes in the MEI (available: http://sealevel.colorado.edu/content/2016rel4-gmsl-and-multivariate-enso-index, accessed October 30th, 2016). Addtionally, Nerem *et al.* (2010) also noted that the detrended GMSL signal is highly correlated with ENSO, with positive/negative RSL anomalies observed during El Niño/La Niña, while Llovel *et al.* (2011) also added that the interannual variability in GMSL variations are inversely correlated with ENSO-driven variations of global land water storage (Meyssignac and Cazenave, 2012); the observed correlation is a result of large scale precipitation changes in the tropics caused by ENSO events, resulting in enhanced rainfall over the oceans and diminished rainfall over land during El Niño events, and vice versa for La Niña (Gu and Adler, 2011).

The regional sea-level change in SE Asia (western tropical Pacific) is the highest observed over the period 1993–2013 (Figure 6). However, the regional patterns observed over this period will recede in the next decades due to decadal and longer timescales fluctuations of trade winds (Becker *et al.*, 2012; Strassburg *et al.*, 2015), as such the patterns we observed are transient. We found that all models investigated agree relatively well with the observed patterns, and reproduce the strong dipole-like pattern in the region, but some models (eg. CSIRO-Mk3.6.0) miscalculate the magnitude of the trends in SE Asia. Strassburg *et al.* (2015) found that after removal of the PDO signal in the region, the rate of sea-level rise greatly reduced, and they projected that in the following decades the region might exhibit trends less than the GMSL trend, while during the period 1993–2013 it experienced trends twice as high the GMSL trend. The densely populated coastal areas of the region renders it vulnerable to future RSL rise and as such it presents great concern as to whether or not the trends observed over the period 1993–2013 will endure in the future as well (Strassburg *et al.*, 2015). Other studies in the western tropical Pacific have shown that sea-level in Freemantle, Australia experiences multi-decadal fluctuations related to Southern Ocean Oscillation (SOI)

and PDO index; this was explained by low-frequency Pacific trade wind fluctuations that force sea-level anomalies that pass through the Indonesian Throughflow region, and along the coastal waveguide of the west coast of Australia (Feng *et al.*, 2004; Merrifield *et al.*, 2012). In this study, we found that CanESM2 and HadGEM2-ES are the two models which capture the RSL patterns the best in this region with rRMS error of only 54%, which is considered relatively good compared to the overall bad performance of the models.

The ensemble mean of the models overestimates the observed sea-level patterns in the eastern equatorial Pacific (Figure 19). Nidheesh *et al.* (2013) found that the region exhibits clear maximum interannual variability, expained by Kelvin wave response to interannual wind anomalies and linked to ENSO, but exhibits little decadal variability. While no significant trend is observed in the region from Figure 6, many models in Figure 16 exhibit trends >4.0 mm/yr (MIROC-ESM, NorESM1-M). This really bad performance of the models in the region is also evident from the really high rRMS errors ranging from 253–532% of the observed regional mean. The large mismatch between CMIP5 models and observations in the region might be attributed to inaccurate representation of wind forcing in CMIP5 models at the 12^{o}N latitude band (Lyu *et al.*, 2016).

RSL patterns in the Southern Ocean are influenced by the Southern Annular Mode (SAM); observations have shown that a poleward intensification of westerly winds since the 1950s, correlate with a positive shift in the SAM (Frankcombe *et al.*, 2013). The SAM causes changes in the patterns and magnitude of wind stress by modifying surface buoynancy fluxes (Sen Gupta and England, 2006), which in their turn modify the strength and position of the ACC (Shakespeare and Hogg, 2012), the intensity of the eddy field (Meredith and Hogg, 2006), and in addition, causes alterations to the meridional overturning circulation (MOC) (Sijp and England, 2009). The observed regional mean over the period 1993–2013 is 2.8 mm/yr in the Southern Ocean. More detailed studies, such as Frankcombe *et al.* (2013), attributed this positive trend over this period mostly to the thermosteric effect and the associated patterns are related to shifts in the wind regime. In this study, the resolution of the observations and models is not good enough to make detailed conclusions on the role of thermosteric sea-level rise in the region, but in Figure 18a and Figure 18e, we see that the land-ice contribution is higher in the area—that we define as the Southern Ocean—but we lack resolution closer to the coast due to the limited satellite coverage, which in turns restricts the range of the land-ocean mask we use to $\pm 68.5^{o}$ in latitude. The Southern Ocean plays a vital role in the redistribution and uptake of heat, and increasing wind stress increases in turn heat uptake, raising GMSL, while a poleward shift of winds decreases heat uptake and lowers GMSL as Frankcombe *et al.* (2013) concluded.

The observed regional mean in North Pacific (3.3 mm/yr) follows the GMSL trend (3.2 ± 0.5 mm/yr) which agree with Moon and Lee (2016) study of the East Japan Sea (EJS). The sea-level variability in EJS has also been linked to PDO, with higher sea-level occuring during the negative phase of the PDO, and vice-versa (Gordon and Giulivi, 2004). Though EJS is not well resolved in our models, it is used here as an indicator of the trends in the region, though not a very sound comparison overall. Most models (Figure 16) fail to capture the large-amplitude meandering nature of mesoscale eddies observed in Figure 6 west of Japan, and this is where most of the relative differences are also located (Figure 23). CSIRO-Mk3.6.0 is the model with the lowest rRMS error, 98%, and the ensemble mean exhibits the second lowest with 93%. Both rRMS errors are as high as the observed regional sea-level change, and thus not in good agreement with the observations.

The observed regional patterns in North Atlantic (Figure 6), characterized by increased sea-level around Greenland and decreased sea-level along the course of the Gulf-Stream, are a result of the North Atlantic dipole (Bilbao *et al.*, 2015). These patterns are the result of changes in heat flux and the AMOC, due to changes in surface buoyancy fluxes from freshwater input and heat (Yin, 2012). Agreement between individual complete models regarding this regional pattern seems to deviate considerably (Figure 16).

CSIRO-Mk3.6.0 is the only model that captures this pattern, while other models (eg. CanESM2, MIROC-ESM) simulate only an increase in sea-level around Greenland but also exhibit an increase along the Gulf-Stream. On the other hand, HadGEM2-ES, MRI-CGCM3, and NorESM1-M simulate a decrease in sea-level during the same period around Greenland. This bad performance of the models in Greenland and Equatorial Atlantic (based on the definitions we give for each region in Table 9) is also seen in Figure 29 with rRMS errors ranging from 76–157% of the observed regional mean in Greenland, and errors ranging from 100–134% for equatorial Atlantic. Suprisingly enough the ensemble mean in Greenland has an rRMS error of 55%, and 88% in equatorial Atlantic, performing relatively "better" than any individual model.

In the Indian Ocean, models reproduce well the observed RSL patterns with ensemble mean rRMS error of 38%. Over the satellite era, the Indian Ocean has experienced RSL rise twice as fast as the global average especially in the northern Indian Ocean since 2003 (Thompson *et al.*, 2016), while during the 1990s the region did not experience such sharp changes. These changes are related to reversal in basin-scale, upper ocean temperature trends. Thompson *et al.* (2016) identified two main mechanism causing this decadal variability: a) the Cross-Equatorial Cell (CEC) forced by zonal wind-stress curl (WSC) at the equator, and b) deep (700 m) upwelling related to zonal wind stress at the equator that causes deep, cross-equatorial overturning. Overall, the wind regimes in the region are mainly responsible for redistribution of heat, and amplification of RSL rise by increasing the amount of ocean heat in the region. The Indian Ocean is particularly vulnerable to RSL changes due to the highly and densely populated coastal region especially in Bangladesh, India, and Jakarta. Assuming that anthropogenic forcing will continue to dominate natural variability in the Indo-Pacific region, the Mascarenhas arhipelago islands, the coast of Indonesia, Sumatra, and the north Indian Ocean might experience even higher RSL rise than the global mean (Han *et al.*, 2010). Rising sea-surface temperatures and ocean acidification will also impact atoll-inhabiting Pacific island nations, as increased ocean temperatures accelerate coral bleaching and reduce the rate of land regeneration (mostly made out of *motu* i.e. crashed corals) resulting in sinking of these islands (Brown *et al.*, 2000).

Overall, the regional performance of individual CMIP5 models against observations is not great but improved relative to CMIP3, possibly due to improved physics and model resolution (Taylor *et al.*, 2012), still they tend to underestimate the altimeter-observed magnitudes of sea-level change over the period 1993–2013. Furthermore, CMIP5 model simulations of sea-level patterns—for instance, in the western tropical Pacific—are usually weaker and occasionally of the wrong sign compared to observations (CSIRO-Mk3.6.0 in Figure 16); it has been suggested that these biases are associated with inaccurate representation of wind forcing patterns at the corresponding latitude band i.e. 12^{o}N (Lyu *et al.*, 2016). The observed sea-level patterns in the tropical Pacific during the short altimeter period are mainly governed by interdecadal climate variability (eg. IPO/DPO) (Meyssignac *et al.*, 2012; Palamisany *et al.*, 2015). Slangen *et al.* (2016) showed that elevated GHGs concentrations of anthropogenic origin play a paramount role on global sea-level rise, however as a result of the low signal-to-noise ratio found in local and regional sea-level variations, the anthropogenic fingerprint cannot always be detected at these smaller spatial scales (Palamisany *et al.*, 2015); thus, it remains uncertain and open for debate whether or not the elevated observed sea-level trends in the western tropical Pacific over the satellite period are of anthropogenic origin (Hamlington *et al.*, 2014; Lyu *et al.*, 2016).

4.4 Improvements for future work

This study is by no means exhaustive regarding the potential analysis one can conduct to verify to even greater extent the main research questions tackled here. A number of improvements can be implemented to the data sets as well as to their analysis. Starting of by extending the local dynamic topography fields to even more CMIP5 AOCGMs. As it was shown above only the 8 complete models used had a local dynamic topography field up to the required date. The rest of the models only reached till 2005. As such one can

extend these model's local dynamic topography field with, for instance, RCP4.5 scenario projections and add them to the rest of models used here, instead of taking the mean local dynamic topography field from the complete models as it was done in this study.

The SL_CCI data set has proven to be quite reliable and accurate. The purpose of this study was to test how model results perform against this new data set. However, in future studies it is advised to also use other satellite altimetry data sets (eg. AVISO, NOAA, NASA) to test how well SL_CCI perform against them. An important aspect of this comparison can be the regional performance of each of these observations, i.e. how well do regional changes of RSL change can be compared among an array of different observational data sets, especially since different groups apply different corrections to them.

Similar to Church and White (2011), a future study can include the computation of Empirical Orthogonal Functions (EOF) of the SL_CCI data set over the period 1993–present. The computation of EOFs will help to distinguish the large-scale interannual variability of the signal, particularly the signal associated with the ENSO phenomenon, and if the seasonal signal is not removed from the signal, one will also be able to distinguish the seasonal north/south oscilation of RSL change (Church and White, 2011). In addition, EOFs can be used to relate spatial patterns between the individual CMIP5 models and the observations.

5 Conclusions

We hereby conclude this study with a summary of our main findings:

- The observed GMSL rise trend over the period 1993–2013 with use of SL_CCI data is 3.2±0.5 mm/yr, and it agrees well with other satellite observational products.
- The multi-model (16 CMIP5 AOGCM) ensemble mean GMSL change (using independent data sets for groundwater, reservoir storage, and GIA) is 3.1±0.5 mm/yr over the period 1993–2013.
- The modelled mass (land-ice and terrestrial water storage) and volume (steric) contributions are 55% and 45% respectively.
- We are confident (within $\pm 1\sigma$ uncertainty) that we can model the sources that contributed 3.2±0.5 mm/yr of observed RSL change over the period 1993–2013 by summation of MGIC, AIS, GrIS, groundwater depletion, reservoir storage, and thermosteric contributions.
- Differences among individual models and between observations and models are larger on regional scale (in some locations >200%), particularly in the eastern equatorial Pacific.
- In places like the Indian and South Atlantic Ocean, the agreement between models and observations is better (ranging within ±50%).
- The global RMS error of the ensemble of 8 CMIP5 models which contain all necessary field to calculate RSL is 2.3 mm/yr, which is 73% of the observed global mean.
- We conclude that while models perform well on a global scale against observations, they do not perform as well on a regional scale over the period 1993–2013.

6 References

6.1 Peer-reviewed literature

Abdalati, W. (2006), 'Recent changes in high-latitude glaciers, ice caps, and ice sheets', *Weather*, **61**(4), 95–101.

Ablain, M., Cazenave, A., Valladeau, G., and Guinehut, S. (2009), 'A new assessment of the error budget of global mean RSL rate estimated by satellite altimetry over 1993-2008', *Ocean Science*, **5**, 193–201.

Ablain, M. and Zawadzki, L. (2014), ESA RSL CCI Error Characterization Report : Altimetry Measurement Errors at Climate Scales.

Ablain, M., Cazenave, A., Larnicol, G., Balmaseda, M., Cipollini, P., Faugère, Y., Fernandes, M. J., Henry, O., Johannessen, J. A., Knudsen, P., Andersen, O., Legeais, J., Meyssignac, B., Picot, N., Roca, M., Rudenko, S., Scharffenberg, M. G., Stammer, D., Timms, G., and Benveniste, J. (2015), 'Improved RSL record over the satellite altimetry era (1993–2010) from the Climate Change Initiative project', *Ocean Science*, **11**, 67-82.

Anthoff, D., Nicholls, R.J., Tol, R.S.J., and Vafeidis, A.T. (2006), 'Global and regional exposure to large rises in RSL: a sensitivity analysis', *Tyndall Centre for climate change Research Working paper 96*.

Bahr, D.B., Meier, M.F., and Peckham, S.D. (1997), 'The physical basis of glacier volume-area scaling', *Journal of Geophysical Research*, **102**, 20355–20362.

Bartolino, J. R., and Cunningham, W.L. (2003), 'Groundwater depletion across the Nation', *U.S. Geological Survey Fact Sheet*, **103**, 4 pp.

Becker, M., Meyssignac, B., Letetrel, C., Llovel, W., Cazenave, A., and Delcroix, T. (2012), 'Sea level variations at tropical Pacific islands since 1950', *Global Planetary Change*, **80**, 85–98.

Becker, M., Karpytchev, M., and Lennartz-Sassinek, S. (2014), 'Long-term sea level trends: natural or anthropogenic?', *Geophysical Research Letters*, **41**, 5571–5580.

Beckley, B., Zelensky, N., Holmes, S., Lemoine, F., Ray, R., Mitchum, G., Desai, S. and Brown., S. (2010), 'Assessment of the Jason-2 extension to the TOPEX/Poseidon, Jason-1 sea-surface height time series for global mean RSL monitoring', *Marine Geodesy*, **33**(1), 447–471.

Bentley, C. R. and Wahr, J. M. (1998), 'Satellite gravity and the mass balance of the Antarctic ice sheet', *Journal of Glaciology*, **44**, 207–213.

Bilbao, R.A.F., Gregory, J.M., and Bouttes, N. (2015), 'Assessment of the regional pattern of sea-level change due to ocean dynamics and density change from 1993–2099 in obserations and CMIP5 AOGCMs', *Climate Dynamics*, **45**, 2647–2666.

Bindoff N., Willebrand J., Artale V., Cazenave A., Gregory J.M., Gulev S. et al. (2007), 'Observations: Ocean Climate Change and RSL'. In: *Climate Change 2007: The Physical Science Basis. Contribution of Working Group 1 to the Fourth Assessment Report of the Intergovernmental Panel on Climate Change* (Solomon S., Qin D., Manning M., Marquis M., Averyt K., Tignor M.M.B. et al., eds), Cambridge University Press: Cambridge, pp. 385–432.

Brown, B., Dunne, R., Goodson, M. and Douglas, A. (2000), 'Bleaching patterns in coral reefs', *Nature*, **404**, 142-143.

Cazenave, A. and Llovel, W. (2010), 'Contemporary RSL rise', *Annual Review of Marine Science,* **2**(1), 145–173.

Chambers, D.P., Cazenave, A., Champollion, N., Dieng, H., Llovel, W., Forsberg, R., Von Schuckmann, K., and Wada, Y. (2016), 'Evaluation of the Global Mean RSL budget between 1993 and 2014', *Survey in Geophysics*, 1–19.

Chao, B.F., Wu, Y.H. and Li, Y.S. (2008), 'Impact of Artificial Reservoir Water impoundment on Global RSL', *Science*, **320**, 212–214.

Church, J.A. and White, N.J. (2006), 'A 20th century acceleration in global RSL rise', *Geophysical Research Letters,* **33**, L01602.

Church, J.A., Roemmich, D., Domingues, C.M., Willis, J.K., White, N.J., Gilson, J.E., Stammer, D., Kohl, A., Chambers, D.P., Landerer, F.W., Marotzke, J., Gregory, J.M., Suzuki, T., Cazenave, A., and Le Traon, P.Y. (2010), 'Ocean Temperature and Salinity Contributions to Global and Regional Sea Level Change', In: *Understanding RSL Rise and Variability*[Church, J.A., Woodworth, P.L., Aarup, T., Wilson, W.S. (eds)], Blackwell Publishing Ltd, 1st ed.

Church, J.A., Aarup, T., Woodworth, P.L., Wilson, W.S., Nicholls, R.J., Rayner, R., Lambeck, K., Mitchum, G.T., Steffen, K., Cazenave, A., Blewitt, G., Mitrovica, J.X., and Lowe, J.A. (2010a), 'RSL rise and Variability: synthesis and outlook for the future', In: *Understanding RSL Rise and Variability* [Church, J.A., Woodworth, P.L., Aarup, T., Wilson, W.S. (eds)], Blackwell Publishing Ltd, 1st ed.

Church, J.A. and White, N.J. (2011), 'RSL Rise from the Late 19th to the early 21st century', *Survey Geophysics*, **32,** 585–602.

Church, J.A., Clark, P.U., Cazenave, A., Gregory, J.M., Jevrejeva, S., Levermann, A., Merrifield, M.A., Milne, G.A., Nerem, R.S., Nunn, P.D., Payne, A.J, Pfeffer, W.T., Stammer, D. and Unnikrishnan, A.S. (2013), 'RSL change', In: *Climate Change 2013, The Physical Science Basis. Contribution of Working Group I to the Fifth Assessment Report of the Intergovernmental Panel on Climate Change* [Stocker, T.F., D. Qin, G.-K. Plattner, M. Tignor, S.K. Allen, J. Boschung, A. Nauels, Y. Xia, V. Bex and P.M. Midgley (eds.)]. Cambridge University Press, Cambridge, United Kingdom and New York, NY, USA.

Clark, J.A., Farrell, W.E. and Peltier, W.R. (1978), 'Global Changes in Postglacial RSL: A numerical calculation', *Quartenary Research*, **9**, 265–287.

Davis R., Sherman J.T. and Dufour J. (2001), 'Profiling ALACEs and other advances in autonomous subsurface floats', *Journal of Atmospheric and ocean Technology*, **18**, 982–93.

Domingues, C.M., Church, J.A., White, N.J., Gleckler, P.J., Wijffels, S.E., Barker, P.M., and Dunn, ,J.R. (2008), 'Improved estimates of upper-ocean warming and multi-decadal RSL rise', *Nature*, **453**, 1090–1093.

Dupont, T.K. and Alley, R.B. (2005), 'Assessment of the importance of ice-shelf buttressing to ice-sheet flow', *Geophysical Research Letters*, ***32***(4), L04503.

Dyurgerov, M.B. and Meier, M.F. (2005), 'Arctic ice caps and glaciers', In: Bamber, J. L. and Payne, A. J. (Eds.) *Mass Balance of the Cryosphere*, Cambridge University Press.

Dziewonski, A.M. and Anderson, D.L. (1981), 'Preliminary reference Earth model', *Physics of the Earth and Planetary Interiors*, **25**, 297–356.

England, M.H., McGregor, S., Spence, P., Meehl, G.A., Timmermann, A., Cai, W., Gupta, A.S., McPhaden, M.J., Purich, A., Santoso, A. (2014), 'Recent intensification of wind-driven circulation in the Pacific and the ongoing warming hiatus', *Nature Climate Change*, **4**(3), 222–227.

Farrell, W.R. and Clark, J.A. (1976), 'On Postglacial RSL', *Geophysical Journal of the Royal Astronomical Society*, **46**, 647–667.

Favier, L., Durand, G., Cornford, S.L., Gudmundsson, G.H., Gagliardini, O., Gillet-Chaulet, F., Zwinger, T., Payne, A.J., and Le Brocq, A.M. (2014), 'Retreat of Pine Island Glacier controlled by marine ice-sheet instability', *Nature Climate Change*, **4**, 117–121.

Feng, M., Li, Y., and Meyers, G. (2004), 'Multidecadal variations of Freemantle sea level: Footprint of climate variability in the tropical Pacific ', *Geophysical Research Letters*, **31**, L13602.

Frankcombe, L.M., Spence, P., Hogg, A.M., England, M.H., and Griffies, S.M. (2013), 'Sea level changes forced by Southern Ocean winds', *Geophysical Research Letters*, **40**, 5710–5715.

Frankcombe, L.M., McGregor, S., and England, M.H. (2015), 'Robustness of the modes of Indo-Pacific sea-level variability', *Climate Dynamics*, **45**, 1281–1298.

Gehrels, R. and Long, A. (2008), 'RSL is not level: the case for a new approach to predicting UK RSL rise', *Geography*, **93**, 11–16.

Gordon, A.L and Giulivi, C.F. (2004), 'Pacific decadal oscillation and sea level in the Japan/East sea', *Deep-Sea Research Part I*, **51**, 653–663.

Gould J. and the Argo Science Team (2004), 'Argo profiling floats bring new era of in situ ocean observations', *EOS Transactions of the American Geophysical Union,* **85.**

Gregory, J.M. and Huybrechts, P. (2006), 'Ice-sheet contributions to future RSL change', *Philosophical Transactions of the Royal Society A*, **364**(1844), 1709–1731.

Gregory, J.M. (2010), 'Long-term effect of volcanic forcing on ocean heat content', *Geophysical Research Letters*, **37**, L22701.

Gregory, J.M., et al. (2013), 'Climate models without pre-industrial volcanic forcing underestimate historical ocean thermal expansion', *Geophysical Research Letters*, **40**, 1–5.

Grinsted, A. (2013), 'An estimate of global glacier volume', *The Cryosphere*, **7**, 141–151.

Gu, G., and Adler, R.F. (2011), 'Precipitation and temperature variations on the interannual time scale: assessing the impact of ENSO and volcanic eruptions', *Journal of Climate*, **24**, 2258–2270.

Hamlington, B.D., Strassburg, M.W., Leben, R.R., Han, W., Nerem, R.S., Kim, K.-Y. (2014), 'Uncovering an anthropogenic RSL rise signal in the Pacific Ocean', *Nature Climate Change*, **4**(9), 782–785.

Han, W., Meehl, G.A., Rajagopalan, B., Fasullo, J.T., Hu, A., Lin, J., Large, W.G., Wang, J., Quan, X.W., Trenary, L.L., Wallcraft, A., Shinoda, T., and Yeager, S. (2010), 'Patterns of Indian Ocean sea-level change in a warming climate', *Nature Geosciences*, **3**, 546–550.

Hegerl, G.C., Zwiers, F. W., Braconnot, P., Gillett, N.P., Luo, Y., Marengo Orsini, J.A., Nicholls, N., Penner, J.E., and Stott, P.A. (2007), 'Understanding and Attributing Climate Change', In: *Climate Change 2007: The Physical Science Basis*, Contribution of Working Group I to the Fourth Assessment Report of the Intergovernmental Panel on Climate Change [Solomon, S., D. Qin, M. Manning, Z. Chen, M. Marquis, K.B. Averyt, M. Tignor and H.L. Miller (eds.)]. Cambridge University Press, Cambridge, United Kingdom and New York, NY, USA.

Huss, M. and Farinotti, D. (2012), 'Distributed ice thickness and volume of all glaciers around the globe', *Journal of Geophysical Research*, **117**, F04010.

Huybrechts, P., Gregory, J., Janssens, I., and Wild, M. (2004), 'Modelling Antarctic and Greenland volume changes during the 20th and 21st centuries forced by GCM time slice integrations', *Global and Planetary Change*, **42**, 83–105.

Ishii, M. and Kimoto, M. (2009), 'Reevaluation of historical ocean heat content variations with time-varying XBT and MBT depth bias corrections', *Journal of Oceanography*, **65**(3), 287–299.

Konikow, L.F. (2011), 'Contribution of groundwater depletion since 1900 to RSL rise', *Geophysical Research Letters*, **38**, 5pp.

Lenaerts, J.T.M., van den Broeke, M.R., van de Berg, W.J., van Meijgaard, E. and Kuipers Munneke, P. (2012), 'A new, high resolution surface mass balance map of Antarctica (1979-2010) based on regional climate modelling', *Geophysics Research Letters*, **39**(L04501).

Leuliette, E.W., and Scharroo, R. (2010), 'Integrating Jason-2 into a Multiple-Altimeter Climate Data Record', *Marine Geodesy*,**33**(1), 504–517.

Leuliette, E.W. and Willis, J.K. (2011), 'Balancing the RSL budget', *Oceanography*, **24**(2), 122–129.

Levitus, S., Antonov, J.L., Boyer, T.P., Locarnini, R.A., Garcia, H.E., and Mishonov, A.V. (2009), 'Global Ocean heat content 1955–2008 in light of recently revealed instrumentation', *Geophysical Research Letters*, **36**, L07608, doi:10.1029/2008GL037155.

Levitus S., Antonov, J.I., Boyer, T.P., Baranova, O.K., Garcia, H.E., Locarnini, R.A., Mishonov, A.V., Reagan, J.R., Seidov, D., Yarosh, E.S., and Zweng, M.M. (2012), 'World ocean heat content and thermosteric RSL change (0–2000 m), 1955–2010', *Geophysical Research Letters*, **39**: L10603.

Liu, Y., Moore, J.C., Cheng, X., Gladstone, R.M., Bassis, J.N., Liu, H., Wen, J., and Hui, F. (2015), 'Ocean-driven thinning enhances iceberg calving and retreat of Antarctic ice shelves', *Proceedings of the National Academy of Science*, **112**(11), 3263–3268.

Llovel, W., Becker, M., Cazenave, A., Jevrejeva, S., Alkama, R., Decharme, B., Douville, H., Ablain, M., and Beckley, B. (2011), 'Terrestrial waters and sea level variations on interannual time scale', *Global Planetary Change*, **75**, 76–82.

Lyu, K., Zhang, X., Church, J.A., and Hu, J. (2016), 'Evaluation of the interdecadal variability of sea surface temperature and sea-level in the Pacific in CMIP3 and CMIP5 models', *International Journal of Climatology*, **36**, 3723–3740.

Marcos, M. and Amores, A. (2014), 'Quantifying anthropogenic and natural contributions to thermosteric RSL', *Geophysical Research Letters*, **41**, 2502–2507.

Marcos, M., Marzeion, B., Dangendorf, S., Slangen, A.B.A., Palanisamy, H., and Fenoglio-Marc, L. (2016), 'Internal variability versus anthropogenic forcing on RSL and its components', *Survey in Geophysics*, **37**, 1–20.

Marzeion, B., Graham Cogley, J., Richter, K., and Parkes, D. (2014), 'Attribution of global glacier mass loss to anthropogenic and natural causes', *Science*, **345**(6199), 919–921.

McGregor, S., Gupta, A.S., and England, M.H. (2012), 'Constraining wind stress products with sea surface height observations and implications for Pacific Ocean sea level trend attribution', *Journal of Climate*, **25**(23), 8164–8176.

Meehl, G.A., Washington, W.M., Collins, W.D., Arblaster, J.M., Hu, A., Buja, L.E., Strand, W.G., and Teng, H. (2005), 'How much more global warming and sea-level rise', *Science*, **307**(5716), 1769–1772.

Meehl, G. A., Stocker, T.F., Collins, W.D., Friedlingstein, P., Gaye, A.T., Gregory, J.M., Kitoh, A., Knutti, R., Murphy, J.M., Noda, A., Raper, S.C.B., Watterson, I.G., Weaver, A.J. and Zhao, Z.-C. (2007), 'Global Climate Projections', In: *Climate Change 2007: The Physical Science Basis. Contribution of Working Group I to the Fourth Assessment Report of the Intergovernmental Panel on Climate Change* [Solomon, S., D. Qin, M. Manning, Z. Chen, M. Marquis, K.B. Averyt, M. Tignor and H.L. Miller (eds.)], Cambridge University Press, Cambridge, U. K. and New York, NY. USA.

Meehl, G.A., Hu, A.,Tebaldi, C., Arblaster, J.M., Washington, W.M., Teng, H., Sanderson, B.M., Ault, T., Strand, W.G., and White, J.B. (2012), 'Relative outcomes of climate change mitigation related to global temperatures versus sea-level rise', *Nature Climate Change*, doi: 10.1038/nclimate1529.

Meier, M.F. (1984), 'Contribution of small glaciers to RSL', *Science*, **226**, 1418–1421.

Meredith, M. P., and Hogg, A.M. (2006), 'Circumpolar response of Southern Ocean eddy activity to a change in the Southern Annular Mode', *Geophysical Research Letters*, **33**, L16608.

Merrifield, M.A. and Maltrud, M.E. (2011), 'Regional sea-level trends due to a Pacific trade wind intensification', *Geophysical Research Letters,* **38**, L21605.

Merrifield, M.A., Thompson, P.R., and Lander, M. (2012), 'Multidecadal sea level anomalies and trends in the western tropical Pacific', *Geophysical Research Letters*, **39**(13), L13602.

Meyssignac, B. and Cazenave, A. (2012), 'Sea level: A review of present-day and recent-past changes and variability', *Journal of Geodynamics*, **58**, 96–109.

Milly, P.C.D., Cazenave, A., Famiglietti, J.S., Gornitz, V., Laval, K., Lettenmaier, D.P., Sahagian, D.L., Wahr, J.M. and Wilson, C.R. (2010), 'Terrestrial Water-Storage Contributions to RSL Rise and Variability', In: Understanding RSL Rise and Variability[Church, J.A., Woodworth, P.L., Aarup, T., Wilson, W.S. (eds)], Blackwell Publishing Ltd, 1st ed.

Mitrovica, J.X. and Peltier, W.R. (1991), 'On postglacial geoid subsidence over the equatorial oceans', *Journal of Geophysical Research*, **96**, 20,053–20,071.

Mitrovica, J.X., Tamisiea, M.E., Davis, J.L., and Milne, G.A. (2001), 'Recent mass balance of polar ice sheets inferred from patterns of global sea-level change', *Nature*, **409**, 1026–1029.

Moon, J.H. and Lee, J. (2016), 'Shifts in multi-decadal sea level trends in the East/Japan Sea over the past 60 years', *Ocean Science Journal*, **51**(1), 87–96.

Nerem, R.S., Chambers, D.P., Choe, C., Mitchum, G.T. (2010), 'Estimating mean sea level change from the TOPEX and Jason altimeter missions', *Marine Geodesy*, **33**(1), 435–446.

Nicholls, R.J. and Cazenave, A. (2010), 'RSL Rise and its Impact on Coastal Zones', *Science*, **328**, 1517–1520.

Nidheesh, A.G., Lengaigne, M., Vialard, J., Unnikrishnan, A.S., Dayan, H. (2013), 'Decadal and long-term sea level variability in the tropical Indo-Pacific Ocean', *Climate Dynamics*, **41**(2), 381–402.

Palamisany, H., Meyssignac, B., Cazenave, A., and Delcroix, T. (2015), 'Is anthropogenic RSL fingerprint already detecable in the Pacific Ocean?', *Environmental Research Letters*, **10**, doi: 10.1088/1748-9326/10/8/084024.

Palamisany, H., Cazenave, A., Delcroix, T., and Meyssignac, B. (2015b), 'Spatial trend patterns in the Pacific Ocean sea level during the altimetry era: the contribution of thermocline depth change and internal climate variability', *Ocean Dynamics*, **65**, 341–356.

Peltier, W.R. (1974), 'The impact response of a Maxwell Earth', *Review of Geophysical and Space Physics*, **12**, 649–705.

Peltier, W.R. (1999), 'Global RSL rise and glacial isostatic adjustment', *Global and Planetary Change*, **20**, 93–123.

Peltier, W.R. (2004), 'Global Glacial Isostasy and the Surface of the Ice-Age Earth: The ICE-5G (VM2) Model and GRACE', *Annual Review of Earth and Planetary Science*, **32**, 111–149.

Peltier, W.R. (2009), 'Closure of the budget of global RSL rise over the GRACE era: The importance and magnitudes of the required corrections for global glacial isostatic adjustment', *Quaternary Science Reviews*, **28**, 1658–1674.

Pokhrel, Y.N., Hanasaki, N., Yeh, P.J.F., Yamada, T.J., Kanae, S., and Oki, T. (2012), 'Model estimates of RSL change due to anthropogenic impacts on terrestrial water storage', *Nature Geoscience*, **5**, doi: 10.1038/NGEO1476.

Pfeffer, W.T., Harper, J.T. and O'Neel, S. (2008), 'Kinematics constraints on glacier contributions to 21st century RSL rise', *Science*, **321**(5894), 1340–1343.

Radic´, V., Hock, R., and Oerlemans, J. (2007), 'Volume-area scaling vs flowline modelling in glacier volume projections', *Annals of Glaciology*, **46**, 234–240.

Radic´, V. and Hock, R. (2010), 'Regional and global volumes of glaciers derived from statistical upscaling of glacier inventory data', *Journal of Geophysical Research*, **115**(F01010).

Reager, J.T., Gardner, A.S., Famiglietti, J.S., Wiese, D.N., Eicker, A., and Lo, M-. H. (2016), 'A decade of RSL rise slowed by climate-driven hydrology', *Science*, 699–702.

Rhein, M., Rintoul, S.R., Aoki, S., Campos, E., Chambers, D., Feely, R.A., Gulev, S., Johnson, G.C., Josey, S.A., Kostianoy, A., Mauritzen, C., Roemmich, D., Talley, L.D., and Wang, F. (2013), 'Observations: Ocean', In: *Climate Change 2013: The Physical Science Basis. Contribution of Working Group I to the Fifth Assessment Report of the Intergovernmental Panel on Climate Change* [Stocker, T.F., D. Qin, G.-K. Plattner, M. Tignor, S.K. Allen, J. Boschung, A. Nauels, Y. Xia, V. Bex and P.M. Midgley (eds.)]. Cambridge University Press, Cambridge, United Kingdom and New York, NY, USA.

Rignot, E. and Thomas, R. H. (2002), 'Mass balance of polar ice sheets', *Science*, **297**, 1502–1506.

Schotman, H.H.A. (2008), 'Shallow-earth rheology from Glacial Isostasy and satellite gravimetry', PhD Thesis, TU Delft.

Sen Gupta, A., and England, M.H. (2006), 'Coupled ocean–atmosphere–ice response to variations in the southern annular mode', *Journal of Climate*, **19**(18), 4457–4486.

Shakespeare, C. J., and Hogg, A.M. (2012), 'An analytical model of the response of the meridional overturning circulation to changes in wind and buoyancy forcing', *Journal of Physical Oceanography*, **42**(8), 1270–1287.

Shepherd, A., Ivins, E.R., Geruo, A., Barletta, V.R., Bentley, M.J., Bettadpur, S., Briggs, K.H., Bromwich, D.H., Forsberg, R., Galin, N., Horwarth, M., Jacobs, S., Joughin, I., King, M.A., Lenaerts, J.T.M., Li, J., Ligtenberg, S.R.M., Luckman, A., Luthcke, S.B., McMillan, M., Meister, R., Milne, G., Mouginot, J., Muir, A., Nicolas, J.P., Paden, J., van de Berg, W.J., van de Broeke, M.R., Vaughan, D.G., Velicogna, I., Wahr, J., Whitehouse, P.L., Wingham, D.J., Yi, D., Young, D., and Zwally, H.J. (2012), 'A Reconciled Estimate of Ice-Sheet Mass Balance', *Nature*, **338**, 1183–1189.

Siedler G., Church J., and Gould J. (eds) (2001), *Ocean Circulation and Climate: Observing and Modelling the Global Ocean*, Academic Press, London.

Sijp, W. P., and England, M.H. (2009), 'Southern Hemisphere westerly wind control over the ocean's thermohaline circulation', *Journal of Climate*, **22**, 1277–1286.

Slangen, A.B.A. and Van de Wal, R.S.W. (2011), 'An assessment of uncertainties in using volume-area modelling for computing the twenty-first century glacier contribution to RSL change', *The Cryosphere*, **5**, 673–686.

Slangen, A.B.A., Katsman, C.A., Van de Wal, R.S.W., Vermeersen, L.L.A., and Riva, L.E.M. (2012), 'Towards regional projections of twenty-first century RSL change based on IPCC SRES scenarios', *Climate Dynamics*, **38**, 1191–1209.

Slangen, A.B.A. (2012), 'Modelling regional sea-level changes in recent past and future', PhD Thesis, Utrecht University, 138 pp. Available: http://dspace.library.uu.nl/handle/1874/257394

Slangen, A.B.A., Van de Wal, R.S.W., Wada, Y., and Vermeersen, L.L.A. (2014), 'Comparing tide-gauge observations to regional patters of RSL change (1961-2003)', *Earth System Dynamics*, **5**, 243–255.

Slangen, A.B.A., Church, J.A., Zhang, X., and Monselesan, D. (2014a), 'Detection and attribution of global mean thermosteric RSL change', *Geophysical Research Letters*, **41**, 5951–5959.

Slangen, A.B.A., Church, J.A., Agosta, C., Fettweis, X., Marzeion, B., and Richter, K. (2016), 'Anthropogenic forcing dominates global mean RSL rise since 1970', *Nature Climate Change*, doi: 10.1038/NCLIMATE2991.

Strassburg, M.W., Hamlington, B.D., Leben, R.R., Manurung, P., Lumban Gaol, J., Nababan, B., Vignudelli, S., and Kim, K.-Y. (2015), 'Sea level trends in Southeast Asian seas', *Climate of the Past*, **11**, 743–750.

Taylor, K.E., Stouffer, R.J., and Meehl, G.A. (2012), 'An overview of CMIP5 and the experiment design', *Bullet of American Meteorological Society*, **93**, 485–498.

Van de Wal, R.S.W and Wild, M. (2001), 'Modelling the response of glaciers to climate change by applying volume-area scaling in combination with a high-resolution GCM', *Climate Dynamics*, **18**, 359–366.

Vaughan, D.G., Comiso, J.C., Allison, I., Carrasco, J., Kaser, G., Kwok, R., Mote, P., Murray, T., Paul, F., Ren, J.,Rignot, E., Solomina, O. Steffen, K. and Zhang, T. (2013), 'Observations: Cryosphere', *In: Climate Change 2013: The Physical Science Basis. Contribution of Working Group I to the Fifth Assessment Report of the Intergovernmental Panel on Climate Change* [Stocker, T.F., D. Qin, G.-K. Plattner, M. Tignor, S.K. Allen, J. Boschung, A. Nauels, Y. Xia, V. Bex and P.M. Midgley (eds.)]. Cambridge University Press, Cambridge, United Kingdom and New York, NY, USA.

Veit, E. and Conrad, C.P. (2016), 'The impact of groundwater depletion on spatial variations in RSL change during the past century', *Geophysical Research Letters*, **43**, 3351–3359.

Velicogna, I., Sutterley, T.C., and Van de Broeke, M.R. (2014), 'Regional acceleration in ice mass loss from Greenland and Antarctica using GRACE time-variable gravity data', *Geophysical Research Letters Space Physics*, **41**, 8130–8137.

Vermeersen, L.L.A. and Sabadini, R. (1999), 'Polar wander, RSL variations and ice age cycles', *Survey Geophysics*, **20**, 415–440.

Vermeersen, L.L.A and Schotman, H.H.A. (2009), 'Constraints on Glacial Isostatic Adjustment from GOCE and Sea Level Data', *Pure and Applied Geophysics*, 166, 1261–1281.

Wada, Y., Van Beek, L.P.H., Sperna Weiland, F.C., Chao, B.F., Wu, Y.H. and Bierkens, M.F.P. (2012), 'Past and future contribution of global groundwater depletion to RSL rise', *Geophysical Research Letters*, **39**(L09402).

Wada, Y., Lo, M.H., Yeh, P.J.F., Reager, J.T., Famiglietti, J.S., Wu, R.J., and Tseng, Y-H. (2016), 'Fate of water pumped from underground and contributions to RSL rise', *Nature Climate Change*, **6**.

Walcott, R.I. (1972), 'Past RSLs, eustasy and deformation of the Earth', *Quartenary Research*, **2**, 1–14.

Wingham, D. J., Ridout, A., Scharroo, R., Arthern, R. and Shum, C. K. (1998), 'Antarctic elevation change from 1992 to 1996', *Science*, **282**, 456–458.

Yi, S., Sun, W., Heki, K., and Qian, A. (2015), 'An increase in the rate of global mean sea-level rise since 2010', *Geophysical Research Letters,* **42***,* 3998–4006.

Yin, J. (2012), 'Century to multi-century sea-level rise projections from CMIP5 models', *Geophysical Research Letters*, **39**:17.

Zuo, Z. and Oerlemans, J. (1997), 'Contribution of glacier melt to RSL rise since 1865AD: a regionally differentiated calculation', *Climate Dynamics*, **13**, 835–845.

6.2 Online sources

Antarcticglaciers.org: Explaining the science of Antarctic glaciology (2016), available: http://www.antarcticglaciers.org/glaciers-and-climate/estimating-glacier-contribution-to-sea-level-rise/ [accessed 25th September 2016].

CMIP5 (2016), available: http://cmip-pcmdi.llnl.gov/cmip5/index.html?submenuheader=0 [accessed 28th September 2016].

ESA CCI "Sea Level" ECV products (2016), available: http://www.esa-sealevel-cci.org/products [accessed 28th November 2016].

GMSL & Multivariate ENSO Index (2016), available: http://sealevel.colorado.edu/content/2016rel4-gmsl-and-multivariate-enso-index [accessed 30th October 2016].

GMSL Rates (2016), available: http://sealevel.colorado.edu/ [accessed 30th October 2016].

IMBIE 2012 (2016), available from: http://imbie.org/data-downloads/ [accessed 29th April 2016].

A Sea-level Equivalent (SLE) calculation

In order to calculate how much global sea-level would rise if all the ice melted (sea-level equivalent, SLE), we must first know the total ocean surface; the value we use is $3.62 \times 10^8\, km^2$. For a 1 mm increase in sea-level, $10^{-3}\, m^3$ or $10^{-12}\, km^3$ of water per m^2 of ocean surface are required (or 10^{-12} Gt). The volume of water required to raise global sea-level by 1 mm is given by:

$$V\ \left(km^3\right) = \left(3.62 \times 10^8\, km^2\right) \times \left(10^{-6}\, km\right) = 3.62 \times 10^2\, km^3 = 362.0\, km^3$$

Converting km^3 of water to Gt, we get that 1 km^3 water is equal to 1 Gt water. Similarly, 1 Gt of ice is equal to 1 km^3 of water. Hence, 362.0 Gt of ice will raise global sea-level by 1 mm. So the SLE is given by the following equation:

$$SLE\ (mm) = M_I\,(Gt) \times \left(1/362.0\, km^3\right)$$

where M_I is the mass of ice. The above derivation is taken from http://www.antarcticglaciers.org/glaciers-and-climate/estimating-glacier-contribution-to-sea-level-rise/ (accessed 25th September 2016).

B List of CMIP5 model names and associated institutions

In the following Appendix, a table of the CMIP5 model names and their associated institutions that provided that model output is given. Available at: http://cmip-pcmdi.llnl.gov/cmip5/index.html?submenuheader=0

Table 11. CMIP5 modelling center (or group), institution ID, and model name used in this study.

Modelling Center (or group)	Institute ID	Model Name
Commonwealth Scientific and Industrial Research Organization (CSIRO) and Bureau of Meteorology (BOM), Australia	CSIRO-BOM	ACCESS1.0
Canadian Centre for Climate Modelling and Analysis	CCCMA	CanESM2
Centre National de Recherches Météorologiques / Centre Européen de Recherche et Formation Avancée en Calcul Scientifique	CNRM-CERFACS	CNRM-CM5
NOAA Geophysical Fluid Dynamics Laboratory	NOAA GFDL	GFDL-ESM2G GFDL-ESM2M
Met Office Hadley Centre (additional HadGEM2-ES realizations contributed by Instituto Nacional de Pesquisas Espaciais)	MOHC (additional realizations by INPE)	HadGEM2-ES
Institute for Numerical Mathematics	INM	INM-CM4
Institut Pierre-Simon Laplace	IPSL	IPSL-CM5A-MR
Japan Agency for Marine-Earth Science and Technology, Atmosphere and Ocean Research Institute (The University of Tokyo), and National Institute for Environmental Studies	MIROC	MIROC-ESM MIROC-ESM-CHEM
Atmosphere and Ocean Research Institute (The University of Tokyo), National Institute for Environmental Studies, and Japan Agency for Marine-Earth Science and Technology	MIROC	MIROC5
Max-Planck-Institut für Meteorologie (Max Planck Institute for Meteorology)	MPI-M	MPI-ESM-LR
Meteorological Research Institute	MRI	MRI-CGCM3
Norwegian Climate Centre	NCC	NorESM1-M NorESM1-ME

C List of acronyms

Table 12. List of acronyms used throughout this study

Acronym	Full name
AIS	Antarctic Ice Sheet
AOGCM	Atmosphere-Ocean General Circulation Model
CMIP5	Coupled Model Intercomparison Project 5
DJF	December-January-February
ESA CCI	European Space Agency Climate Change Initiative
FIS	Fennoscandian Ice Sheet
GHGs	Greenhouse gases
GFO	Geosat Follow-on
GIA	Glacial Isostatic Adjustment
GrIS	Greenland Ice Sheet
GMSL	Global Mean RSL
GPS	Global Position System
GW	Groundwater
ICOLD	International Commision of Large Dams
IPCC	Intergovermental Panel for Climate Change
ITRF	International Terrestrial Reference Frame
JJA	June-July-August
kBP	Thousands years before present
LGM	Last Glacial Maximum
LIS	Laurentide Ice Sheet
MGIC	Mountain Glaciers and Ice Caps
MSLA	Monthly Sea Level Anomaly
NADW	North Atlantic Deep Water
RACMO2	Regional Climate Model 2
RS	Reservoir Storage
RSL	Relative Sea Level
SLE	Sea Level Equivalent
SRES	Special Report on Emissions Scenarios
SSH	Sea Surface Height
SST	Sea Surface Temperature
WOCE	World Ocean Circulation Experiment
XBT	Expendable Bathythermographs

D Acknowledgements

I acknowledge the World Climate Research Programme's Working Group on Coupled Modelling, which is responsible for CMIP, and I thank the climate modeling groups (listed in Table 11 Appendix B) for producing and making available their model output. For CMIP the U.S. Department of Energy's Program for Climate Model Diagnosis and Intercomparison provides coordinating support and led development of software infrastructure in partnership with the Global Organization for Earth System Science Portals. In addition, I would like to thank the SL_CCI project for making available the satellite altimeter products, and their administration team for providing me access to the data, and their fast response in answering my questions.

On a personal level, I would first like to thank my supervisor R.S.W. van de Wal for giving me the opportunity to undertake this project and for his support, guidance, feedback, and professional advice throughout the duration of this project. Secondly, I would like to thank my second supervisor A. Slangen for her help with the glacier and sea-level model, providing me with data sets for the individual contributions of the modelled RSL rise, and for her expertise regarding the processing/treatement of these data sets, as well as additional programming advice and feedback on the first drafts. Furthermore, I would like to thank my girlfriend, Julia, for her immense love, support, and tolerance through this difficult task. Last but definitely not least, a big thank you goes to my parents and sister, Spiros, Sylvia, and Margarita, for their unconditional love, and economic and mental support throughout the years of my studies, and for believing in me.